Dissertation zur Erlangung des Doktorgrades
der Fakultät für Chemie und Pharmazie
der Ludwig-Maximilians-Universität München

TRANSLATIONAL, ORIENTATIONAL AND SPECTRAL DYNAMICS OF INDIVIDUAL MOLECULES IN NANO-STRUCTURED MATERIALS STUDIED WITH SINGLE-MOLECULE-SPECTROSCOPY

Christian Hellriegel

aus

São Paulo, Brasilien

2005

Erklärung

Diese Dissertation wurde im Sinne von §13 Abs. 3 bzw. 4 der Promotionsordung vom 29. Januar 1998 von Prof. Dr. Christoph Bräuchle betreut

Ehrenwörtliche Versicherung

Diese Dissertation wurde selbstständig, ohne unerlaubte Hilfe erarbeitet.

München, den 30.Juni 2005

(Unterschrift)

Dissertation eingereicht am: 1.7.2005
1. Gutachter: Prof. Dr. Christoph Bräuchle
2. Gutachter:Prof. Dr. Thomas Bein
Mündliche Prüfung am:25.7.2005

Index

1. Introduction **10**

2. Theoretical Background **14**

2.1. Host-Guest Materials **15**

2.2. Fluorescence and SMS **28**

2.2.1 Fluorescence **28**

2.2.2. Single-Moelcule Spectroscopy **31**

2.3. Diffusion **35**

2.3.1 Macroscopic **35**

2.3.2 Microscopic **37**

3. Experimental Section **50**

3.1. Microscopy Techniques **51**

3.1.1 Confocal Microscopy **53**

3.1.2 Widefield Imaging Microscopy **62**

3.2. Analysis Programs **66**

3.2.1. Evaluation of Diffusion **66**

3.2.2. Evaluation of Single Molecule Spectra **79**

3.2.3. Evaluation of Orientation Measurements **81**

3.2.4. Photostability of Fluorescent Dye Molecules **84**

4. Results and Discussion **90**

4.1. Characterization of Host-Guest Materials (ensemble) **91**

4.2. Photostability of New Dyes for SMS **103**

4.3. Orientational Distribution of Oxazine Dyes in $AlPO_4$-5 **109**

4.4. Translational Diffusion of TDI in MCM41S Monoliths **114**

4.5. Translational Diffusion of 9A1 in Sol-Gel Glass **117**

4.6. Translational Diffusion of TDI Molecules in SBA-15 Films **130**

4.7. Spectral Behavior of TDI in PMMA **137**

4.8. Covalently bound Cy5 in MCM-41 **148**

5. Summary **158**

6. Bibliographical Information **163**

7. Appendix **172**

1. Introduction

The importance of materials in technology, science and everyday life is self-evident. Among promising materials for emerging applications (think of smart materials, medical diagnostics, nanoelectronic devices etc.) are the so-called host-guest materials, where a molecular species is incorporated as a guest into a solid host. Interesting hosts for the incorporation of guests (biomolecules, indicators, catalysts, fluorescent dyes, etc.) are, for example, inorganic micro- and mesoporous materials, which can be thought of as a well-defined system of nanometer-sized pores.[Davis02], [Wark03]

If such host-guest materials can be seen as a nanometer-sized system of pores in which the individual guest molecules may move, turn or perform a specific task, then it is of fundamental importance to observe and to understand the behavior of guest molecules in such a system.

The characterization of the behavior of fluorescent dye molecules in porous materials is the central topic of this thesis. The topic is addressed using single-molecule-spectroscopy (SMS) and microscopy techniques. It will be shown that SMS methods allow for a very thorough characterization of the behavior of dye molecules in the studied samples.

Since the first observations of individual molecules via fluorescence [Moerner89], [Orrit90], the SMS technique has developped to become a mature and established technique that can be used at room-temperature to investigate complex systems, like polymers, crystals, liquid solutions and biological samples [Basché96], [Nie97], [Xie98], [Tamarat00], [Rigler01]. Two recent reviews [Moerner02], [Kulzer04] cover the most recent developments in SMS. Apart from addressing interesting questions in material science [Gruber97], [Kulzer97], [Deschenes01], [Weston01], [Schuster02], it is clear that SMS can also be used as a powerful technique to answer biophysical questions [Rigler90], [Kinosita98], [Weiss99], [Kitamura99], [Seisenberger01].

The first direct observation of the dynamics of individual fluorescent molecules in nanostructured porous materials were published in 2002 [Seebacher02] and were part of my diploma thesis. In the subsequent time, it was possible to expand the used SMS setup, to improve the data acquisition and evaluation so that presently it is not only possible to *detect* individual molecules in a nanostructured material but also to characterize their dynamical behavior at an unprecedented level of detail.

This thesis is subdivided into three main chapters (i.e. chapters 2, 3 and 4) followed by the summary, the bibliographical information and the appendix.

Chapter 2 covers the theoretical background and is subdivided into three sections. The first section describes the host structures, that is the inorganic porous materials used. The second section introduces fluorescence, as the measured quantity of the guest molecules, and describes the advantages of the SMS approach. The third section covers the topic of diffusion which is the main dynamical phenomenon observed.

Chapter 3 describes the experimental setup (confocal and widefield microscopes) and the evaluation programs used to analyze the data. The necessary theoretical background for the techniques is included in this chapter, in the respective section. The emphasis of this chapter lies in the evaluation programs which were conceived and written in order to process the extensive amount of data produced by the microscopes. These programs are essential for the evaluation of data. Comparable or even suitable programs are not commercially available.

Chapter 4 describes the results and is subdivided into 8 sections. It addresses the experiments and results going from the straightforward ensemble measurements to the more elaborate SMS experiments. The emphasis lies in sections 4, 5, and 6 which present studies on the translational diffusion of individual moelcules in diverse nano-structured mesoporous materials. Spectral and orientational dynamics are described in sections 7 and 8.

2. Theoretical Background

As outlined in the introduction, the main subject of the scientific investigations presented in this thesis is the dynamical behaviour of individual molecules incorporated as guests in a porous host material.

This chapter is subdivided in three sections. The host materials, and in particular the relevant host materials are introduced in the first section. The guests, fluorescent dye molecules are visualized individually via their fluorescence, the second section in this chapter describes fluorescence and the basic principle of single-molecule spectroscopy. This section illustrates in particular why SMS is a superior technique in comparison to ensemble methods. The last section in this chapter describes diffusion in detail as it is the most important dynamical behaviour studied.

2.1. Host-Guest Materials

A host-guest material is any binary compound in which a molecular species, the guest, is incorporated into a solid matrix, the host. In a narrower definition a host-guest material also displays properties not present for the individual components and that result from the interplay between host and guest.[Langley99].

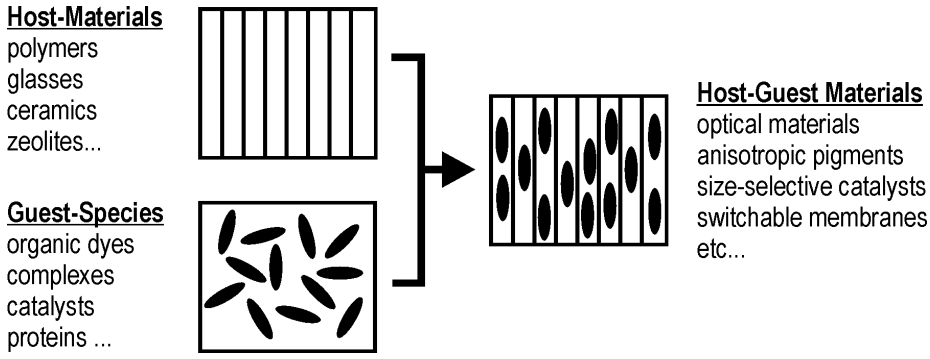

Figure 1: Schematical diagram illustrating the idea behind a host-guest material.

The broad variety of interplay possibilities between host and guest can be explored to generate interesting materials[Wark03], such as: novel pigments, phosphors, nonlinear optical materials[Caro94], micrometer-sized lasers[Schüth95], waveguides[Yang00], switchable membranes for size selective separation[Weh02], materials with controllable pore openings [Ban04], energy transfer materials[Gfeller98], sensors[Meinershagen99] and many more. There are numerous ways to combine host materials (polymers, glasses, porous materials, etc.) with guest species (dye molecules, catalytic complexes, biologically active molecules, etc.) to produce host-guest systems. Among these methods are those that use the spatial arrangement of inorganic porous materials or molecular sieves, such as zeolites and templated mesoporous silicas as a host structure for the well-defined incorporation of a molecular guest species. [Megelski01], [Schulz02].

Inorganic porous materials have particularly appealing properties for the use as host materials: (a) The materials are mechanically, chemically and thermally stable. (b) Their structure allows an ordered incorporation of guests molecules creating well-defined spatial arrangements in the resulting host-guest material. (c) From the synthetic point of view the structure of the pores can be varied in size, interconnectivity and polarity. (d) Some of these materials can be thought of as a well-defined grid, or a system of pipes, for the ordered incorporation of functional guest molecules.

Despite the numerous applications and successful synthesis procedures leading to host-guest materials, there are many important open questions in the characterization of these materials. For example: (a) How do the guest molecules behave in the confined environment? (b) What properties of the host and guest have an influence on this behaviour? (c) Can the behavior be influenced by external factors (e.g. light irradiation, addition of solvents)? (d) Over which range are the materials homogenous in their properties? (e) How easily can molecules become incorporated into the materials? (f) Are the pores accessible to molecules coming from the outside? (g) Does the material degrade in any way? Etc.

Recently, the techniques of fluorescence microscopy and single molecule spectroscopy (SMS) have been successfully employed in the characterization of host-guest materials. These methods address such questions and provide new and detailed insight to the guest behaviour inside the host materials. Results of such investigations are presented in the 'results and discussion' section of this thesis.

2.1.1. Inorganic molecular sieves

'Molecular sieve' is the designation for any porous material capable of separating molecules due to the interplay between the pore-size and the molecular size, just like a sieve.[Szostak89] In this picture, the pore sizes of molecular sieves are comparable to the size of a molecule, i.e. between 0.1 and 10 nm. Inorganic porous materials such as sol-gel glasses, M41S-type materials and zeolites are typical molecular sieves. The materials investigated in this thesis are described in more detail below.

Sol-Gel-Glasses

The materials with the least ordered structure used in the presented studies are sol-gel-glasses (also called 'xerogels'). These amorphous, micro- and mesoporous silicas are widely used as hosts in technical applications because they are cheap and easy to prepare via a sol-gel synthesis [Brinker85] in a variety of physical forms, including powders, cast monoliths and spin-coated thin films. Sol-gel-glasses can be synthesized with a wide range of mean pore-diameters, from 0.5 nm to 200 nm and a wide range of specific surfaces from 100 to 1000 m^2/g. The pores are interconnected, open to the exterior and can easily be loaded with gases, liquids or solids dispersed in a liquid.

The pore size of a sol-gel-glass is not uniform and is broadly distributed around a mean value (around ± 100% [Thommes02]) . The pore interconnectivity is random. The average porosity can be influenced by varying synthesis parameters. It has been shown that the physico-chemical structure of a sol-gel-glass is a result of a complex sequence of gelation, aging and drying conditions employed during processing. This is illustrated schematically in figure 2. Note, for example, that base-catalysed gels have a higher degree of branching of the polymers in the gel whereas their acid-catalysed counterparts are more linear.

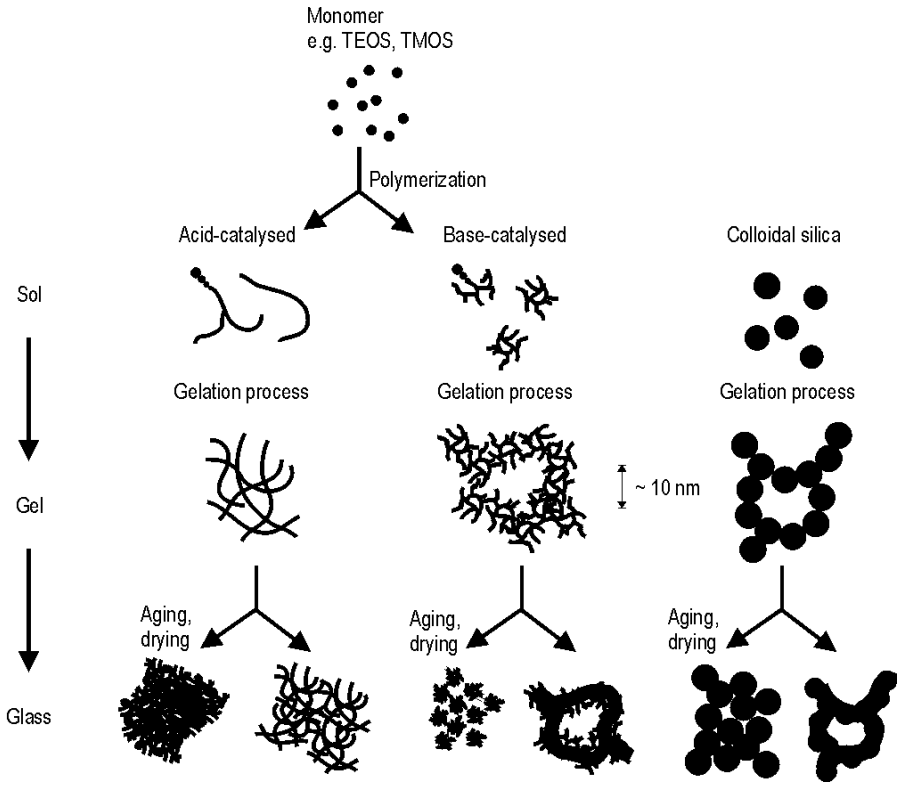

Figure 2: Formation mechanisms of a sol-gel-glass. Sol-gel-glasses are formed from precursor particles or monomers, the sol, that condenses to form a gel. Further condensation, aging and drying of the gel leads to the porous siliceous material, the sol-gel-glass. The gelation, aging and drying conditions affect the structure of the resulting porous material. Adapted from [Brinker85].

The advantages of using sol-gel-glasses to build host-guest materials are related to the simple synthesis procedure of the host material and the easy loading of the material with guest species. The high specific surface area, porosity and accessibility to molecules from the exterior of the solid body makes them, for example, ideal support materials for catalysts.[Schwarz95] Furthermore, sol-gel-glasses are often used as model materials to study confinement effects, for example on solvation-dynamics [Baumann01], [Baumann03] or on diffusion [Wirth03], [Hellriegel04]. Sol-gel-glasses have also found use in molecular recognition systems [Jimenez02] and have been used to stabilize reactive species [Cauzzi99].

The limitations of sol-gel-glasses in their use as host-matrices are directly related to their unspecific structure: The highly heterogenous pore architecture and the broad distribution of pore sizes makes sol-gel-glasses less suitable for materials that have to exhibit very specific effects related with the size and architecture of the pores, which for example are required in regioselective catalysis or molecular sieving with high size-specificity. In the same sense it is not possible to use these materials for the ordered incorporation of guests, as required e.g. in non-linear optical applications. The properties of the guests in such a disordered material will show a strong distribution or pronounced heterogeneities reflecting the various types, orientations and sizes of pores in which the guests may be incorporated. For example, processes and applications based on diffusion, like the suggested use of sol-gel glasses as a matrix for chromatography [McCalley05] or electrophoresis [Palmer02], are expected to show a pronounced heterogeneity.

Templated Mesoporous Materials

Templated mesoporous materials, like the group of M41S materials, represent the next level of structural organization of a molecular sieve. These amorphous porous silicas are synthesized via condensation, aging and drying of a gel formed by silica precursors (such as TEOS or TMOS) in the presence of a supramolecular structure-directing agent (SDA). [Kresge92], [Ying98] This supramolecular species, for example a surfactant forming a micellar liquid crystal, serves as a template around which the silica condenses forming the solid matrix.

The exact formation mechanism (see fig.3) of the material has not yet been elucidated in detail. There is evidence for a direct templating mechanism (fig. 3a), in which the supramolecular template structure is formed before the condensation of the solid matrix. This seems to be the case when using neutrally charged molecules (like octaethylen-monododecylether) as a structure directing agent. On the other hand there is also strong

evidence (*in situ* X-Ray diffractometry) indicating that the condensation of the solid matrix occurrs in a cooperative or concerted mechanism (fig. 3b). This seems to be the case in the synthesis using charged molecules as structure directing agent, and via evaporation induced self-assembly (EISA). [Grosso04], [Zhang02]

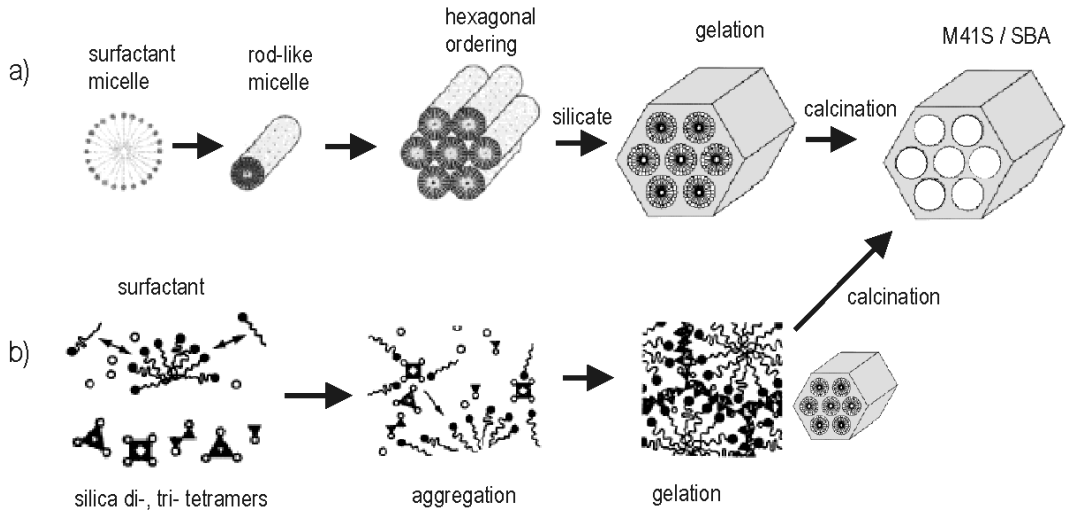

Figure 3: Suggested formation mechanism of templated mesoporous materials. a) Direct templating mechanism: The supramolecular structure (e.g. a micellar liquid crystalline phase) forms before condensation of the silica. b) Concerted or cooperative mechanism: The structure is formed as the silica condenses. Adapted from [Ying98]

The resulting materials show a high ordering of the pores with narrowly distributed pore-diameters (around ± 1% [Thommes02]) as a consequence of the presence of the template structure during the formation of the matrix. Evidently, large template molecules, like amphiphilic block co-polymers, form pores with a large diameter (up to 20 nm), whereas smaller species, for example ionic surfactants like CTAB, form small pores (down to 2 nm). The formation mechanism of the amorphous SiO_2 pore walls themselves is similar the sol-gel-process discussed in the preceding sub-section. The SiO_2 walls have a typical thickness between 1 and 2 nm (3-6 SiO_2 units)[Kruk00], and may in turn be microporous (pore diameter < 1 nm) depending on the synthesis conditions.[Ravikovitch01]

The resulting pore topology formed by the supramolecular arrangement of the template may vary from micellar arrays to layered structures, as illustrated for M41S type materials in figure 4.

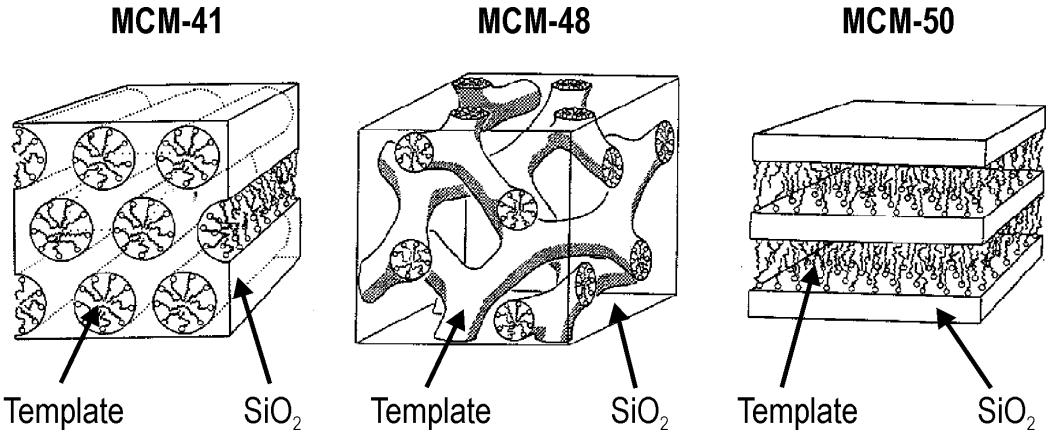

Figure 4: Different channel structures of M41S-Materials. The channel topology is a consequence of the organization of the supramolecular template formed in the synthesis. Shown here are three examples (from left to right): The pore architecture of MCM-41 results from a hexagonal array of micelles, the architecture of MCM-48 is based on a three-dimensial cubic arrangement of micelles and in MCM-50 the structure is formed on the basis of a layered structure of the template.

The supramolecular arrangement of the template, in turn, depends primarily on the synthesis conditions (concentration of template, temperature, air humidity, aging time). This dependence can be illustrated in the form of a phase diagram, as obtained, for example, for spin coated MCM-type films using cetyltrimethylammonium bromide (CTAB) as a structure directing template (see fig. 5a). [Besson03]

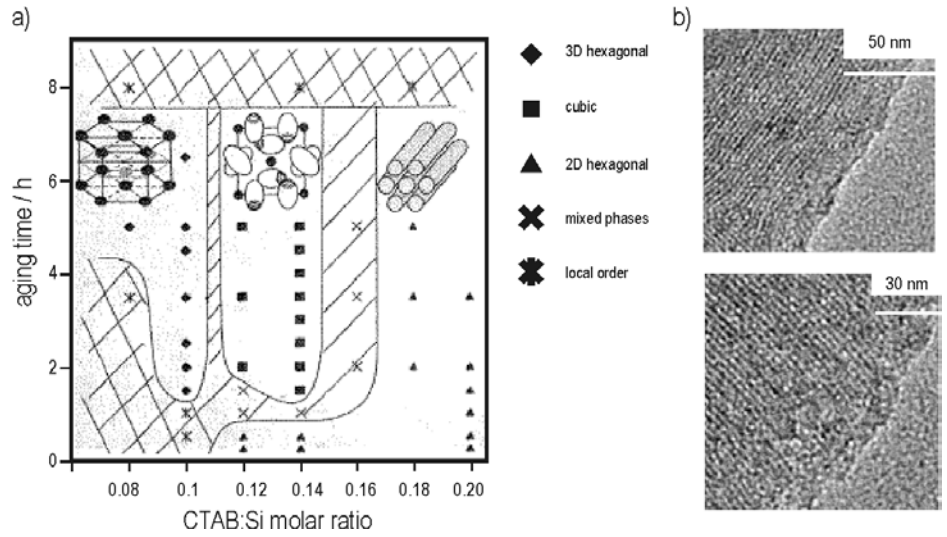

Figure 5: The formation of different structures depends on synthesis conditions. a) Phase diagram (aging time versus surfactant concentration) of CTAB Templated spin-coated films. Adapted from [Besson03] b) TEM images of spin-coated MCM-41 (CTAB template), corresponding to the 2D hexagonal phase in the phase diagram. The views in the micrographs are parallel to the substrate surface. Images from [Petkov04].

The short-range order of the pores - on the100 nm scale - can be characterized using X-ray diffraction techniques and transmission electron microscopy, TEM (e.g. fig. 5b). TEM images show that the pores, organized in hexagonal bundles, do not necessarily extend linearly over the entire body of the material. Instead, it is a common finding that the pores are arranged domains of a few 100 nm in size forming fingerprint motifs. The long-range order of the pores (in the order of a few µm) and the interconnectivity of the domains is presently not sufficiently well characterized.

Currently, some of the main challenges in the synthesis of these materials are: (a) To achieve an internal functionalization of the material, for example via covalent binding of dyes, catalysts and functional molecules, like cis-trans isomerizable molecules or biological receptors to the inner pore surface. (b) To form materials with long range order of the pores (on the µm-scale), with (c) a specific orientation relative to the substrate surface. And also (d) to form large, defect-free monolithic bodies or membranes.

Zeolites, porosils and zeotype-structures

Crystalline porous solids like zeolites, porosils and zeotype-structures show the highest level of structural organization of a molecular sieve. A zeolite is commonly defined via its chemical structure, which consists of tetrahedral SiO_4^{4-} and AlO_4^{5-} subunits connected in a regular way. In a zeolite, the periodical arrangement of the chemical subunits forms crystallographically well-defined cages and pores, which are accessible to molecules from the exterior of the material. A porosil is similar to a zeolite in the sense that its structure can be derived from a zeolite structure, but it is composed exclusively of SiO_2 units (e.g. Silicalite-1, SSZ-24, etc.). A zeotype-material is similar to a zeolite in the same sense, but is composed of different chemical subunits (e.g. $AlPO_4$-5, CrAPO-5, etc.).

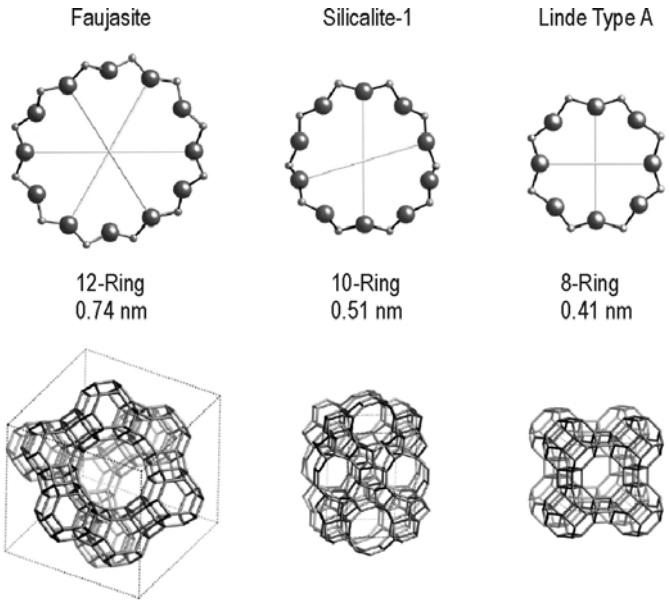

Figure 6: Typical examples for zeolite structures. From [ZeoliteAtlas05]

The structural arrangement of the aforementioned tetrahedral subunits results in typical types of pore openings, which can be classified according to the number of oxygen atoms present in the underlying ring structure, namely 12, 10 and 8 oxygen atoms. The characteristic diameters of these openings are respectively 0.7, 0.5 and 0.3 nm (see figure 6). The arrangement and the interconnectivity of these structures can lead to different types of pore architecture along one, two or three cartesian axes, and may also lead to the

formation of the so-called supercages, which are nearly spherical voids with diameters in the nm-range, a well-known example for a zeolite with 1.3 nm supercages is faujasite (see fig. 6).

Zeolites are obtained in the laboratory by crystallisation of gels containing Al and Si sources in aqueous medium at temperatures in the range of 100-190 °C and autogenous pressure for several days or weeks. Besides Si and Al sources the reaction mixture can be prepared using other metal sources, and often also quaternary ammonium ions which direct the crystallisation to a specific crystal structure.[Corma04]

Zeolites are widely used as catalysts in technical applications, e.g. in catalytic cracking and Friedel-Crafts alkylation. Besides catalysis their well-defined structures can further be explored to generate host-guest materials with highly specific properties (sensors, solid lasers, etc.). The range of guest molecules that can be incorporated into a zeolite is, however, limited due to material's pore diameters. In a zeolite the pore diameter (or supercage opening) rarely exceeds 0.8 nm, making impossible the incorporation of more complex molecules, such as organic dye molecules which are often larger than 1 nm. It is possible, however, to form large molecular species in a zeolite supercage via a so-called ship-in-the-bottle synthesis[Domenech05],[Ricci04] or to encapsulate large molecules during synthesis [Ganschow01] - note that the encapsulation of large foreign species is likely to affect the structure of the material or to induce defects at the incorporation site.

Some of the current challenges in zeolite synthesis and characterization are: (a) the synthesis of large crystals in optical quality (i.e. µm-sized and defect free) and with large pore openings, that may accomodate more sizeable molecules. (b) The production of films in which the individual zeolite crystals are arranged in a specific order with respect to a substrate. (c) the synthesis of functional host-guest materials via a ship-in-a-bottle synthesis, in which the desired guest species is, for example, synthesized in a zeolite supercage and cannot escape the material. (d) The characterization of processes taking place in these materials, like diffusion, energy transfer, spectral or orientational dynamics.

Two important materials of this class, that have been studied in this thesis, are the zeotype $AlPO_4$-5 (AFI) and the porosil Silicalite-1 (MFI).

$AlPO_4$-5 (AFI): AFI is a zeotype material. Its structure (figure 7) is characterized by the arrangement of AlO_4^{4-} and PO_4^{3-} tetrahedra that form hexagonally arranged unidimensional channels of 0.73 nm in diameter (considering van-der-Waals radii). AFI can be synthesized in the form of large (µm to mm-sized) crystalline hexagonal prisms or rods. The large pore diameter, the unidimensional arrangement of the pores and the possibility to synthesize large crystalline bodies makes AFI an interesting host material for the ordered incorporation of organic dye molecules.

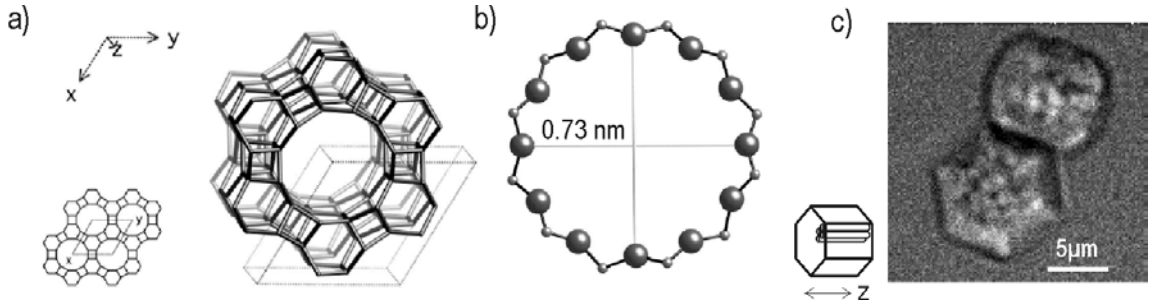

Figure 7: Structure of $AlPO_4$-5 a) 3D-Structure b) 12-Ring dimensions. [ZeoliteAtlas05] and c) Transmission micrograph showing the typical habitus of the studied AFI crystals.

AFI is conventionally synthesized in a hydrothermal process using equimolar quantities of Al_2O_3, P_2O_5 and tripropylamine (Pr_3N) in aqueous solution (35 fold excess of water) at 160°C under autogenous pressure for 6 - 24h and pH between 2 and 4. The synthesis time is reduced drasitically to less than 45 minutes using microwave assisted synthesis (a typical synthesis batch $Al_2O_3/P_2O_5/Pr_3N/H_2O$ is 1/1/2/150). The microwave assisted synthesis also has the advantage that the synthesis batch reaches the necessary high temperature quickly (within 1 min), allowing the syntheis of pure $AlPO_4$-5 phases, slower heating, as in the conventional hydrothermal synthesis, often leads to the formation of different $AlPO_4$ phases (such as $AlPO_4$-8) that are intergrown with $AlPO_4$-5 in the product particles.[Ganschow01]

Silicalite-1: The porosil Silicalite-1 (MFI) can be synthesized in the form of µm-sized crystalline bodies with a well defined (usually coffin-shaped) morphology. MFI is an attractive material for technical applications because of the possibility to synthesise oriented films of MFI on various substrates [Xomeritakis99] (a defect free MFI film would, for example, act as a permselective membrane).

Its structure (figure 8) is characterized by the arrangement of two systems of pores of ca. 0.55 nm in diameter (considering van der Waals radii): (a) straight pores along [010] and (b) sinusoidal pores perpendicular to [010] interconnecting the pores (cf. figure 8a).

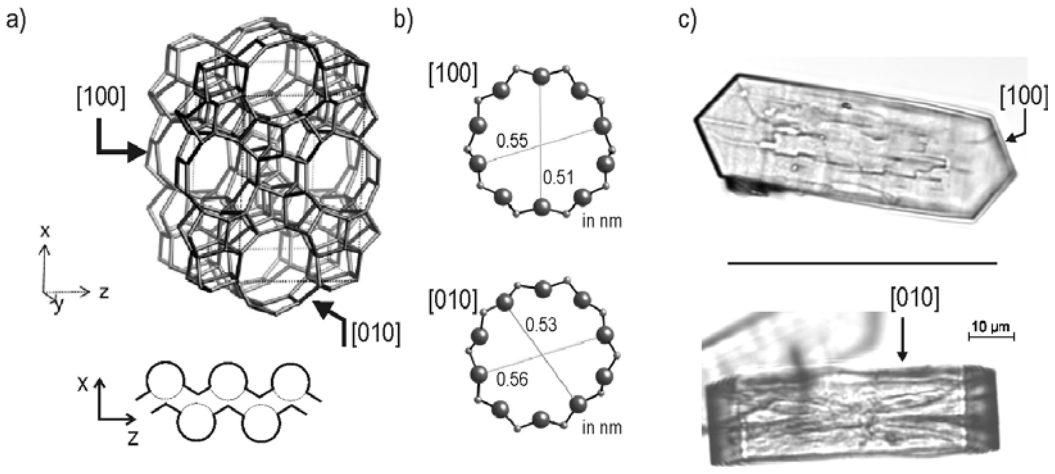

Figure 8: Structure of MFI. a) 3D-Structure of MFI b) 10-Ring dimensions c) Transmission micrographs of MFI crystals showing its typical habitus. [Hellriegel03]

There are numerous synthesis procedures to form MFI. Typically, it is synthesized from a silica source (e.g. Cab-o-sil M5) in aqueous solution, in the presence of tetrapropyl-ammonium bromide, HF and NH_4F in an autoclave (170°C, 14d) [Guth86]. The typical crystalline bodies formed are not single crystals and exhibit comparatively large defect structures that extend to the inner volume of the particles. [Seebacher01],[Bonilla01].

Summary: The most important properties of the host materials just discussed, with relevance for the studies presented in this thesis are resumed in the follwing table. The last column indicates in what study the host material has been used.

host-material	pore-sizes (nm)	advantages	limitations	studied host-guest materials
sol-gel-glass	0.3-200	synthesis is easy, simple and cheap	a) heterogenous structure b) distribution of pore sizes is very broad.	diffusion of VG5(dye) in sol-gel-glasses of different porosity
templated materials (M41S / SBA)	2-20	narrow distribution of pore-sizes, and well-defined architecture.	a) synthesis difficulties b) long range (0.1-10 μm) order of pores not well-defined	a) diffusion of TDI(dye) in SBA-15 and MCM-41. b) Effect of different solvents on Cy5(dye) covalently bound to the pores of MCM-41
zeolites and zeotype-structures	0.3-0.8	crystalline bodies	a) small pores, b) synthesis of big defect-free crystals difficult	a) detection of defect structures on MFI coats. b) energy transfer between different dyes in AFI c) orientational distributions of oxazine dyes in AFI

2.2. Fluorescence and Single-Molecule-Spectroscopy (SMS)

2.2.1 Fluorescence

Fluorescence can be described semi-classically by the interaction of light with a quantum mechanical system (cf. physical chemistry textbooks like [Moore76] or [Levine83]). In a simplified schematical energy diagram for organic fluorescent dye molecules, the fluorescence occurrs as follows:

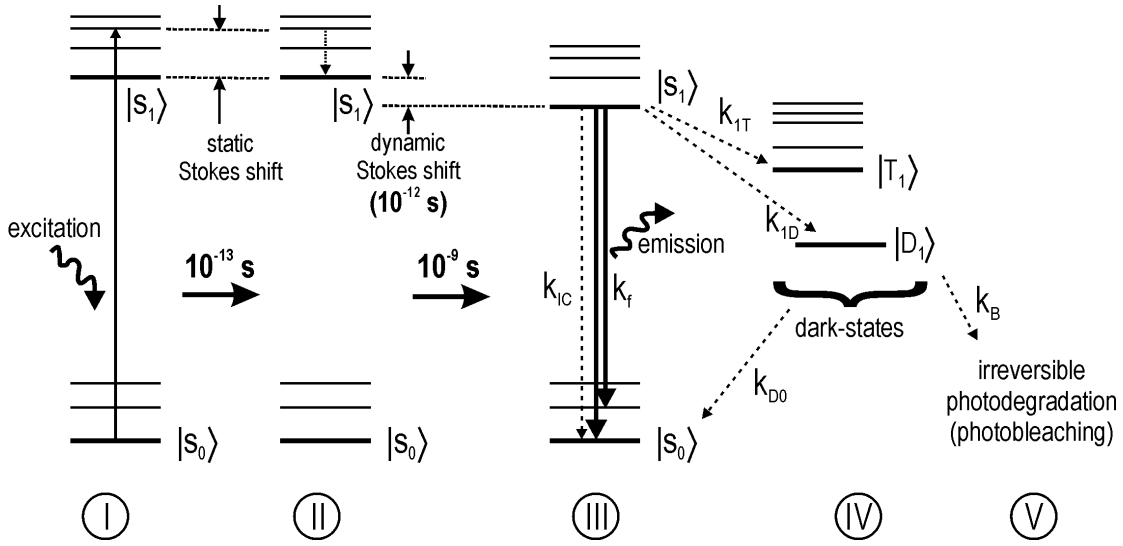

Figure 9: Schematical energy diagram illustrating the basic principles involved in fluorescence (dashed lines represent radiationless relaxation pathways).

Dynamics of Fluorescence: At room temperature a dye molecule rests in the lowest electronic state, the singlet S_0. An incoming photon (with suitable energy and polarization) excites the molecule to the next-highest electronic state, the singlet state S_1. (I in fig.9) The absorbtion according to the Franck-Condon principle leads the molecule to a higher vibrational state in S_1, from where it relaxes within 10^{-13} to 10^{-12} seconds to the vibrational ground state in S_1 (II). The next relaxation step, from S_1 to S_0 can occur in different ways. The most probable relaxation step leads the molecule directly to S_0 typically within the next few 10^{-9} seconds under emmission of a photon. The photons emitted in this step make up the fluorescence light (III). These photons are red-shifted in comparison to the photons used for the excitation because of the static (I→II) and

dynamic (on the 10^{-12} s time-scale) Stokes shifts. Less probable steps from S_1 are (a) the radiationless relaxation via internal conversion (IC), and (b) radiationless relaxations via dark-states, such as the triplet T_1. From the dark-states the molecule may relax back to S_0 from where a new excitation-relaxation cycle can begin again (IV→I). In the schematical diagram above, the transition probabilities to the involved states are expressed as transition rates k. The ratio between the fluorescent rate k_f and the sum of all relaxation rates, the fluorescence quantum yield ϕ_f, gives the probability that the relaxation from S_1 will occur under emission of a photon:

$$\phi_f = k_f / k_{TOT} \qquad (1)$$

With $k_{TOT} = (k_f + k_{IC} + k_{1T} + k_{1D} + k_{1D'}...)$ increasing with additional radiationless relaxation mechanisms. Clearly, a good fluorescent dye molecule has a quantum yield near 1, and few interfering dark-states, or radiationless relaxation channels.

The best-understood and characterized dark-state is the triplet state T_1.[McGlynn69] which can also be studied for specific fluorescent dye molecules [Kulzer99], [Fleury00], in these molecules the low triplet-rates k_{1T} (between 10^{-4} and 10^{-5} s^{-1}) do not effectively compete with the main relaxation channel of fluorescence. The typical life-time of the triplet in such molecules is in the order of a few µs. Some recent works covering the identification and the characterization of fluorescence dynamics involving other dark states are [Zondervan03], [Verberk02], [Renge02], [Zehetmayer02] and [Jung01b].

The End of Fluorescence / Photobleaching: In an idealized system the absorption-emission cycle would go on indeterminately. In real systems the molecule may undergo an irreversible reaction from one of the excited states (S_1, T_1, D, etc.) to form a non-fluorescing species. This last step in the duty-life of a fluorescent molecule is called 'photobleaching' (V in fig.9). The photobleaching mechanisms can be very complex, and few are presently understood in detail: The suggested mechanisms vary from reaction via the triplet state, or via other dark states (S_2, T_2, D', D'', etc.), from transient radical-formation to reactions with the surrounding medium (cf. also section 3.2.4.).

Fluorescence Spectra: The relative positions of the states in the energy diagram above, result in the respective absorbtion and emission spectra. The typical room-temperature absorption and fluorescence spectrum of an organic dye molecule (TDI) is shown in fig.10 and consists of broadened emission bands resulting from the main (00) transition and transitions to vibronic states in S_0 that may appear well or less well resolved depending on the molecule in question.

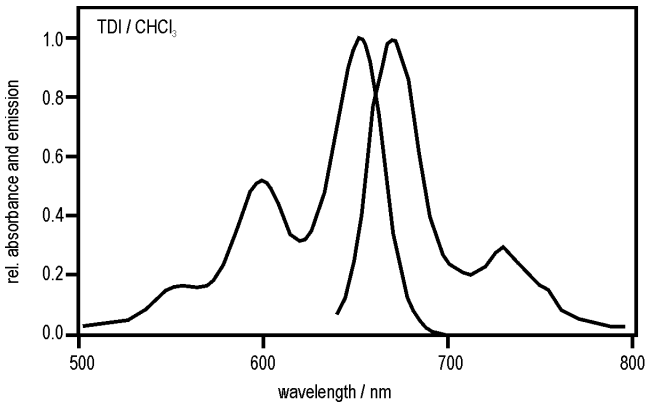

Figure 10: Typical absorption and emission spectrum of an organic fluorescent dye molecule (TDI in $CHCl_3$; normalized spectra, excitation at 633 nm).

In an idealized system the absorption and emission lines should be as narrow as a few ten MHz, limited only by the uncertainty principle. However, in real systems and at room temperature the emission bands are broadened to some THz because of: (a) the *homogenous broadening* in which the underlying quantum mechanical systems are coupled to inumerable fluctuating energy levels in the molecule's immediate surroundings (e.g. solvent molecules, thermal fluctuations in a solid matrix) and (b) the *ensemble averaging effect*, in which the slightly different, stastistically distributed fluorescence spectra of many individual molecules add up to form the ensemble spectrum. The *ensemble averaging* is suppressed on going to higher dilutions of dye molecules, so that their fluorescence can be detected individually At room temperature the single molecule spectrum is still broadened (to some THz) due to the *homogenous broadening* and resembles the ensemble spectrum. The *homogenous broadening* is the most significant contribution to the spectral broadening and can be eliminated on going to cryogenic temperatures (< 4 K).

2.2.2 Single-Moelcule Spectroscopy (SMS)

The essential task in single molecule spectroscopy (SMS) is to separate any signal, (e.g. fluorescence) from an individual molecule from the remaining signals of the sample (background light, fluorescence from other molecules, etc.). In principle tunneling microscopy (STM) [Binnig82],[Hofer03], force microscopy (AFM) [Binnig86], [Giessibl03], and electron microscopy (SEM, TEM) [Fultz01], which can record images of a surface with a spatial resolution on the atomic scale, can also be counted to the SMS methods. More frequently, however, SMS is associated with optical emmission spectroscopy and microscopy of individual fluorescing molecules (or particles such as nano-crystals), which can also be situated in the volume of a transparent sample. A number of reviews on SMS has been published in recent years. [Nie97], [Tamarat00], [Moerner02], [Barkai04], [Kulzer04]. The technique has gained considerable attention since the first experiments more than a decade ago; developping to become a mature technique employed in fields as diverse as biology [Rigler90], [Kinosita98], [Weiss99], [Kitamura99], [Seisenberger01] and material science [Gruber97], [Kulzer97], [Deschenes01], [Weston01], [Schuster02]. SMS studies provide details that cannot be accessed by the conventional ensemble methods. The most important aspects of SMS, and these advantages, will be described in the following.

There are basically three strategies that can be followed in typical SMS measurements to isolate the emmission of individual molecules: (a) The *spectral selection* of fluorescence, which is typically carried out at liquid-helium temperatures, because the emission spectrum of the molecules at that temperature becomes extremely narrow (~10 MHz) (cf. previous section). (b) The *spatial selection* of fluorophores via dilution, which is typical for room-temperature experiments. In high dilutions ($< 10^{-9}$ M) the individual molecules are spatially separated by a few hundred nanometers and can be examined with sensitive fluorescence microscopy techniques. (c) The *temporal selection* of fluorophores in a detection volume (e.g. as the fluorophores diffuse into and out of a defined detection volume), and the subsequent analysis of the temporal fluctuations, as in fluorescence correlation spectroscopy (FCS).

SMS resolves distributions: An SMS method has the capability of resolving individual properties of the investigated molecules, and thus has access to the distribution function of a studied property. This stands in contrast to conventional ensemble spectroscopy methods, in which properties are measured for an ensemble of molecules, and are perceived as a sum or an average from all contributions of all individual molecules.

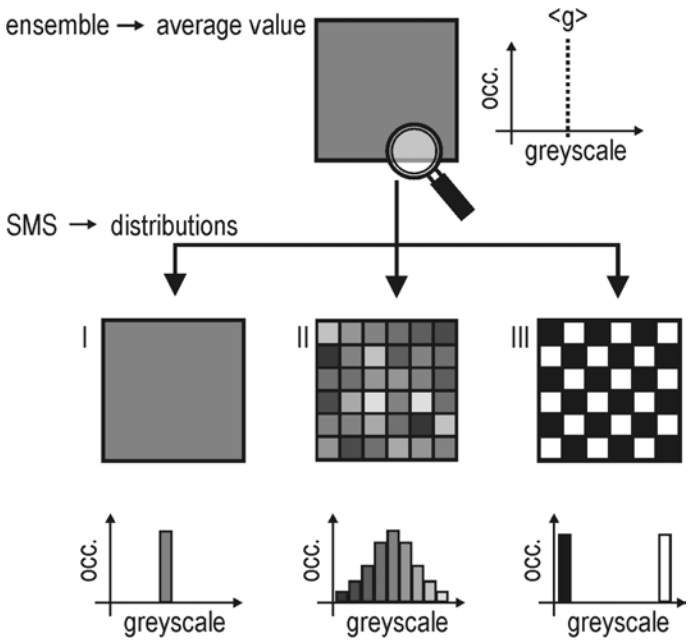

Figure 11: Ensemble measurements give an average value for a measured property (here the greyscale value). SMS resolves the distribution of the values around the mean value. Note in case III that the mean value obtained in the ensemble measurement has no physical meaning.

This advantage of SMS is illustrated schematically in figure 11, using greyscale values as an examplary property. In the ensemble measurement the average value (e.g. 50% grey) is readily obtained. By analysing the individual components that make up the ensemble it is possible to obtain the distribution of the studied property around a mean value. Note that it is possible to conceive cases in which the mean value of a studied property does not correspond to any real existing value in the sample (for example case III in figure 11).

SMS resolves dynamics: In the same sense, the study of dynamics (e.g. diffusion) is more detailed in SMS. In an ensemble measurement it is only possible to study dynamics by synchronizing the individual components. While it is possible to detect pronounced heterogeneities using ensemble methods, it is not possible to assign the individual components to specific sub-populations, and to study systems in dynamic equilibrium.

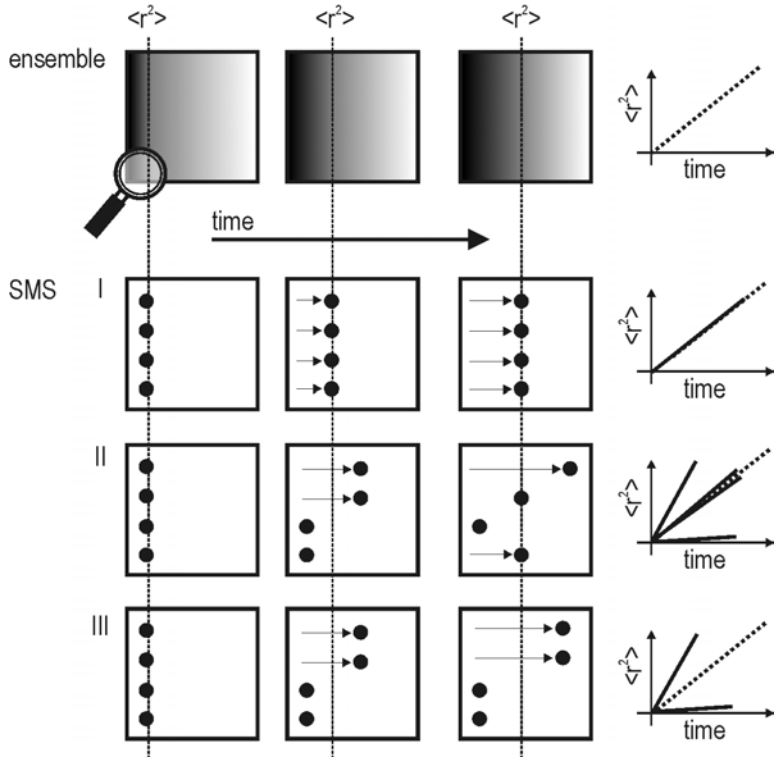

Figure 12: Ensemble measurements fail to detect sub-populations in a dynamic measurement (here, diffusion). The direct observation of individual molecules resolves sub-populations. Note in case III that the mean value obtained in the ensemble measurement has no physical meaning.

The advantage of the SMS approach is illustrated in figure 12 using diffusion as an example. The diffusion of an ensemble of individual components is characterized by the spatial and temporal evolution of the concentration (indicated by a grey-scale gradient in fig.12). By analysing the individual diffusing components that make up the ensemble it is possible to resolve the distribution of the diffusional behaviours. Note that it is possible to identify different sub-populations of molecules with different diffusivities in cases II and III, and furthermore to observe interconversion between mobile and immobile sub-

populations in case II. This kind of data is not available from ensemble measurements and allows for a thorough interpretation of the involved dynamics. It is possible to determine, for example, if the retardation of a particle during diffusion is caused by a specific mechanism (e.g. entering and escaping a bottle-neck trap). Furthermore it is possible to infer whether the effect is the same for all molecules or if two populations with differing diffusivities are separated but coexisting in the same sample.

SMS Summary: The SMS technique brings a series of advantages in the characterization of a sample because it detects the properties (e.g. fluorescence intensity, position, fluorescence spectrum, polarization) of individual molecules and thus (a) resolves the distribution function of the studied property. This stands in contrast to an average value that can be obtained from a conventional measurement on an ensemble of molecules. (b) Using SMS it is possible to characterize dynamics in a high level of detail. (c) SMS also allows to observe and to characterize rare or extreme phenomena (on the flanks of a distribution curve) that would otherwise remain undetected in an ensemble measurement.

While SMS is usually associated with the detection and spectroscopy of individual fluorescent dye molecules, it can, in a wider sense be used to denote the observation of any individual emitter. Examples for such emitters are: carbon nanotubes [Lefebvre04], nanoparticles, fluorescent proteins, DNA-complexes, dendrimers [Cotlet04], emitting polymers [Müller04], defect centres in crystals [Gaebel04] and quantum dots. Some of these sytems, most notably the quantum dots and semiconductor nanoparticles can be considered to be superior chromophores in comparison to conventional organic dye molecules (typically 100 times more photostable and 20 times brighter). Their use, for example, in biological systems or as probes in molecular sieves is limited, however, because of their size (typically 15 nm and above) and chemical behaviour (e.g. toxicity). Individual emitters are widely used as minimally perturbing tracers, as e.g. used in the tracking of viruses in living cells [Seisenberger01] or motor proteins [Peterman04]. Single molecules are also very interesting light sources for the generation of 'individual photons' or 'photons on demand' [Kiraz05], [Moerner04] - which are important concepts in the field of quantum optics and quantum cryptography.

2.3. Diffusion

Diffusion is a fundamental phenomenon taking place on fields as diverse as biology, astronomy and communication sciences. In a very raw definition, diffusion can be seen as the dynamic spreading of any physical property, such as the amount of particles, heat, or information. In the following considerations, diffusion will be restricted to the transport of matter, and more specifically, to the diffusion of molecules, which is of obvious importance for applications based on porous materials: The working mechanisms and the performance of ion exchangers, catalysts, adsorbers and molecular sieves depend on the diffusion properties of the involved molecular species. Before turning to experimental considerations on how to observe and characterize diffusion, a compact introduction to the theoretical background of diffusion is given.

2.3.1. Macrsocopic Treatment of Diffsuion

Diffusion describes the movement of matter, or molecules in space and in time. It is possible to address the involved questions from a macroscopic (ensemble) and from a microscopic (particulate) perspective. In the macroscopic approach the amount of particles per volume is described by a concentration. Diffusion is then associated to the change of concentration with time and space. The theory of macroscopic diffusion is described by the Fickian equations (e.g. [Moore76]):

$$J_{x,t} = -D\left(\frac{\partial C(x,t)}{\partial x}\right) \quad \text{and} \quad \frac{\partial C(x,t)}{\partial t} = D\left(\frac{\partial^2 C(x,t)}{\partial x^2}\right) \tag{2,3}$$

In words, the flux $J_{x,t}$ of particles (along a spatial axis x and at a time t) is proportional to the spatial gradient of concentration, and the change of concentration with time is proportional to the change in the slope of the gradient. The consequence is that the flux has a maximum at the place with the highest difference in concentration, and that the concentration does not change with time at the place with the highest flux. The power of

this approach lies in the fact that it allows to predict the distribution of concentrations at any given time, just by knowing the initial concentrations and boundary conditions that define the diffusing system. Two relevant problems and the solutions for the differential equations (2,3) are given in the following (adapted from [Carlslaw59]):

a) Diffusion into a gaussian shaped, depleted region with a characteristic radius r and from a limited reservoir - e.g. dye diffusion into a photobleached spot, $I(r,t) \sim C(r,t)$:

$$C(r,t) = \frac{c_0}{\sqrt{(4\pi Dt)^3}} \exp\left(\frac{-r^2}{4Dt}\right) \qquad (4)$$

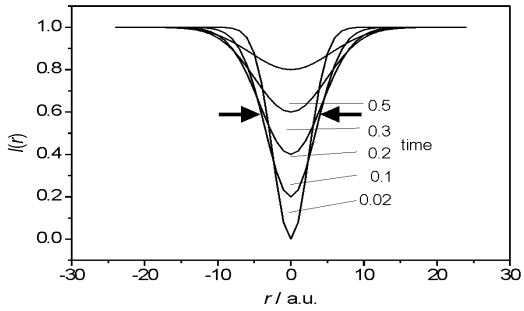

b) Diffusion perpendicular to a plane source (along x) from an unlimited reservoir - e.g. dye uptake by a straight crystal boundary from solution, with $I(x,t) \sim C(x,t)$:

$$C(x,t) = 1 - c_0 \,\mathrm{erfc}\left(\frac{x}{\sqrt{4Dt}}\right) \qquad (5)$$

Note: $\mathrm{erfc}(x) = \int_0^x \exp\left(\frac{-z^2}{w^2}\right) dz$

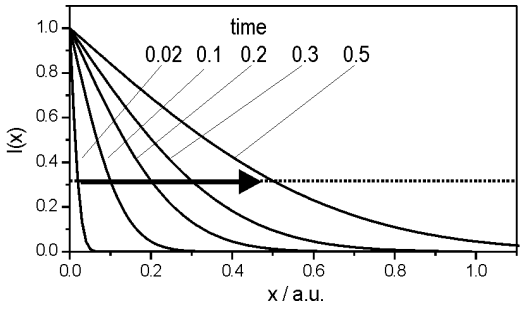

The central quantity in these equations is the diffusion coefficient D, which in the macroscopic picture can be interpreted as an amount of particles or molecules diffusing perpendicularly through a unit area in a specific interval of time. Experimentally, D is obtained by measuring the spatial distribution of a concentration (e.g. of fluorescent dye molecules) and evaluating its temporal evolution.

2.3.2. Microscopic Treatment of Diffusion

The macroscopic method, described above, has limitations. It is not sensitive towards different sub-populations or, more generally, to distributions of diffusional behaviours and depends strongly on the assumption of diffusion models. The experimentally observed behaviour is often difficult to characterize properly using the idealized ensemble models. Furthermore, the macroscopic approach using the Fickian diffusion equations will not work in the study of systems under equilibrium. In such systems the concentration gradient and consequently the net flux are zero, despite the fact that the molecules are actually diffusing (see fig.13).

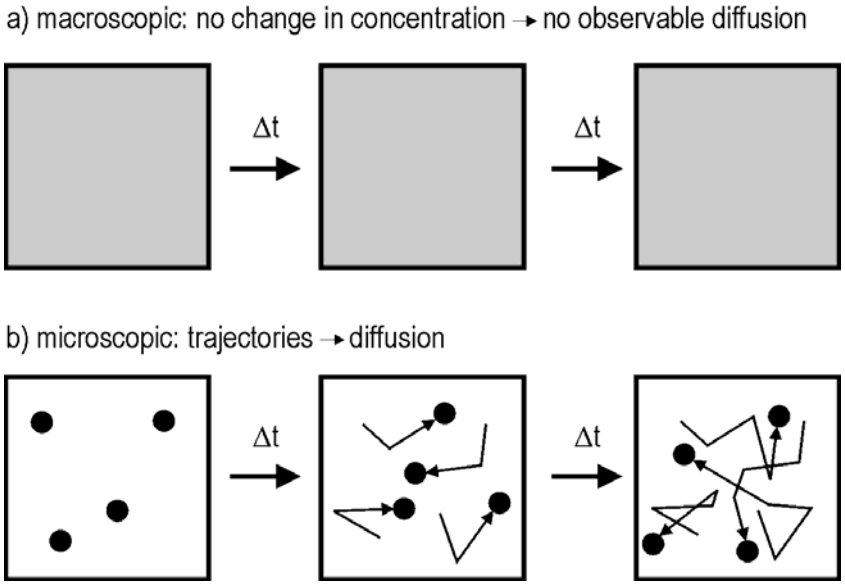

Figure 13: Comparison between macroscopic and microscopic observation of diffusion in equilibrium - e.g. particles in a liquid solution. a) In the macroscopic approach it is not possible to determine a change in the concentration. b) In the microscopic approach the trajectories of the diffusing particles are resolved and can be used to characterize diffusion.

In the microscopic approach, the characterization of diffusion is based on the observation of the movement of an individual diffusing particle (e.g. a fluorescent molecule). This method has a series of advantages over the macroscopic approach: (a) It is independent from any initial conditions (i.e. concentration gradients or other boundary conditions). The investigated system can thus be in equilibrium (see fig.13). (b) The evaluation based on the individual particle that makes up the ensemble contains information on the distribution of diffusivities, which may vary spatially, or from particle to particle - the 'ensemble averaging' effect is supressed. Sub-populations and, in general, the distributions of diffusional behaviours are resolved. (c) It is possible to resolve mechanistic details, or events such as adsorption / desorption, that take place during diffusion (transient traps).

The characterization of diffusion based on the observation of individual trajectories of a diffusing particle has to account for the statistical nature of diffusion.[Chandrasekhar43] This has two implications: First, a large number of individual trajectories has to be evaluated to allow for a proper description of the diffusional behaviour - this is particularly important for the characterization of sub-populations and/or distributions of diffusional behaviours. Second, the physical interpretation of the diffusion process may become more complex, because the observation of individual trajectories reveal spatial and temporal heterogeneities not described by the simpler models of diffusion. While the measurements of individual trajectories is more difficult to accomplish experimentally, and while the analysis is more complex, the information gained from the analysis of individual trajectories adds a significant amount of quality to the obtained data.

In the next sub-sections a few diffusion models, and the evaluation of diffusion based on the parameters obtained by analysis of the trajectories, are presented with increasing complexity.

Random walk: The isotropic random walk is the simplest mode of motion for a diffusing particle. A central result of the microscopic treatment of diffusion is that in a random walk, the mean square displacement of a diffusing particle, $\langle r^2(t)\rangle$, follows a linear dependence with time:

$$\langle r^2(t)\rangle = 4\,Dt. \qquad (6)$$

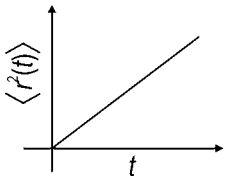

Equation 6, the Einstein equation for a two-dimensional random walk, is the central equation in most diffusion studies.[Einstein05], [Einstein06] It can be shown that the diffusion coefficient D corresponds exactly to the macroscopic diffusion coefficient.[Chadrasekhar43], [Berg93] In the microscopic model, the diffusion coefficient D describes the area that the particle explores per unit of time during its random walk.

Starting from a trajectory sampled in time intervals δt it is easy to calculate the mean square displacement $\langle r^2(t)\rangle$ for every time lag $t = n\delta t$ (n is the number of sample periods between two positions in the trajectory). In a random walk, every position of the trajectory serves as a starting point for the analysis. With n steps in the trajectory the number of individual steps leading to a mean square displacement at a time lag t=1δt is n, the number of steps leading to a mean square displacement (MSD) at a time lag 2δt is n-1, for a time lag 3δt it is n-2 and so on. As a consequence the statistical error for the mean square displacement increases with observation time, as less steps are used to calculate the mean value. The diffusion coefficient D is obtained in a straightforward way via a linear regression for $\langle r^2(t)\rangle$ versus time lag (see fig.14).

Deviations from a Random Walk: The individual mean square displacements do not necessarily follow a linear dependence with the observation time, as shown above for the random walk diffusion. In real systems, the diffusion of an individual particle is often influenced by local anisotropies, such as obstacles, adsorption sites, regions with increased viscosity or regions with a uniform flow. These influences are visualised as

deviations from the linear behaviour in a $\langle r^2(t)\rangle$ versus time plot. [Berg93], [Qian91], [Schmidt96], [Saxton97] and [Schütz97]. For some specific cases, it is possible to derive analytically a mathematical formula that describes the time dependence of the MSD. A small collection of such diffusion equations is given below (adapted from [Saxton97]):

$$\left\langle r^2(t)\right\rangle = 2nDt \qquad \text{random walk in } n\text{-dimensions} \qquad (7)$$

$$\left\langle r^2(t)\right\rangle = 4Dt^{\alpha} \qquad \text{anomalous 2D-diffusion} \qquad (8)$$

$$\left\langle r^2(t)\right\rangle = 4Dt + (Vt)^2 \qquad \text{2D-diffusion with flow} \qquad (9)$$

$$\left\langle r^2(t)\right\rangle \cong \left\langle r_C^2\right\rangle \left[1 - A_1 \exp\left(\frac{-4A_2}{\left\langle r_C^2\right\rangle} Dt\right)\right] \qquad \text{confined motion} \qquad (10)$$

In these equations the mean-square displacements as a function of time, $\langle r^2(t)\rangle$, relate to a diffusion coefficient D. Equations 16-19 are plotted as $\langle r^2(t)\rangle$ versus time in figure 14:

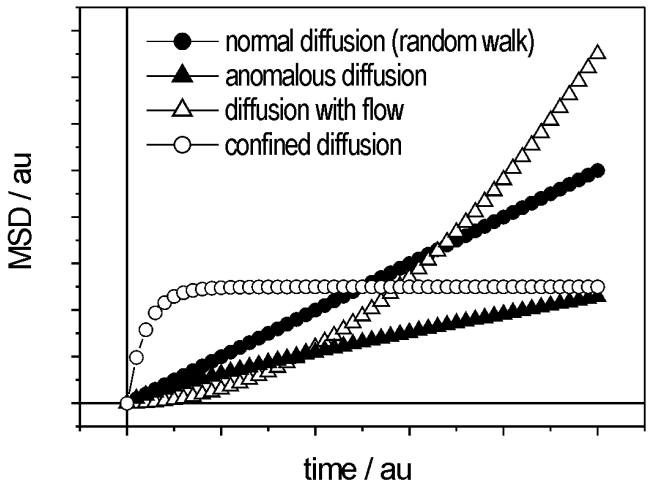

Figure 14: Different types of diffusion lead to different time-dependencies of the MSD. The four depicted curves relate to equations 7-10.

Normal diffusion (eq. 7) gives a linear curve through the origin. In the case of anomalous diffusion (eq.8), in which the exponent α is a number between 0 and 1, the curve has a decreasing slope. In the case of diffusion with drift (eq. 9) a (constant) drift velocity (V)

leads to a quadratic increase of $\langle r^2(t) \rangle$ with time. In the last case (eq. 10) a molecule diffuses within a confined region. It can be shown that the value of the asymptote $\langle r_C^2 \rangle$ corresponds to the effective area of the confinement. The other parameters in equation 10 (A_i) relate to the confinement geometry, and are not easily obtained analytically. A reliable value for the diffusion coefficient D can only be determined if these parameters are known.

Influence of pores on diffusion: The influence of pores, or generally of geometrical constraints on the diffusional behaviour can be complex: (a) The diffusivity is in general reduced due to the presence of barriers, and it also depends on their geometrical shape and arrangement, for example, if the pores are straight, curved, interconnected or if they form bottleneck traps. (b) Particles interact with the walls of the pores, and may for example be subject to absorption/desorption kinetics.

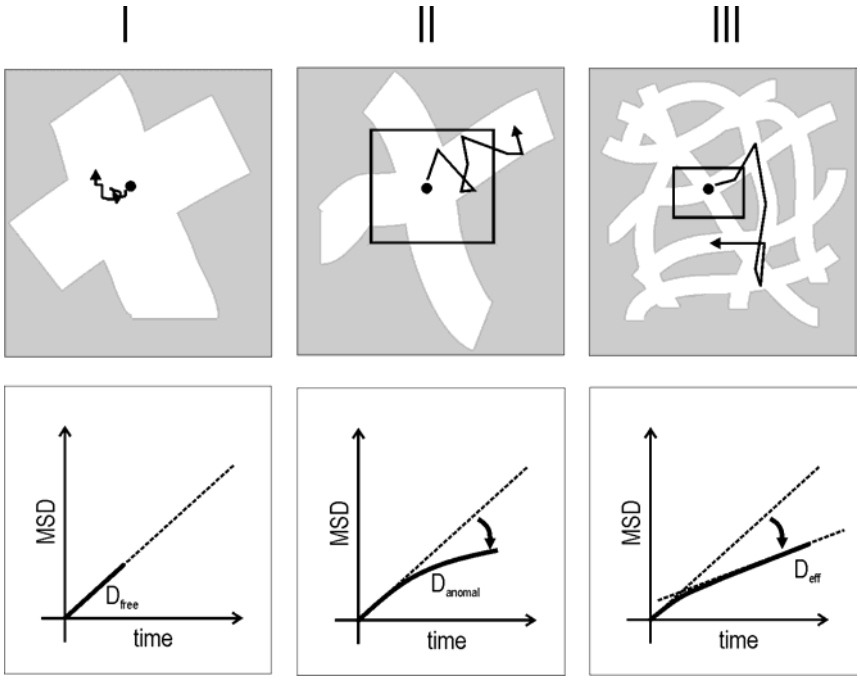

Figure 15: Reduction of the diffusivity due to pores on different time scales.

Taken together, these influences of the geometrical constraints affect diffusion on several time scales. If the temporal or spatial scale of the influences is large in comparison to the

trajectory or to the temporal and spatial resolution of the experimental apparatus, the diffusion will be perceived as unaffected by the geometrical constraint (case I in figure 15). If the temporal or spatial scale of the effects is comparable to the trajectory size the diffusivity becomes anomalous (case II in fig. 15). If the interactions take place on a very short time-scale, and if the molecules are otherwise free to diffuse in interconnected pores, the effects average out to give a normal diffusivity with a reduced *effective* diffusion coefficient, D_{eff} (case III in fig.15). The the ratio between the effective (case III) and the free (case I) diffusion coefficients ($D_{\text{free}} : D_{\text{eff}}$) can be expressed by a factor R, which comprises the influences of the geometry (e.g. the tortuosity) and interconnectivity of the pores (e.g. a 'labyrinth factor') for long observation times. The influence of the geometrical constraints can, however, be more complex, for example if the pores are so narrow that the molecules cannot pass each other (resulting in single-file diffusion). The effects of the geometrical constraints are difficult to predict analytically, and are usually compared with simulations.[Saxton97], [Regier05]

Distinguishing sub-populations: In the cases described so far the overall behaviour of one molecule or a group of molecules was assumed to be normally distributed. In a random walk, for example, the mean value for the individual mean squared displacements $\langle r^2(t)\rangle$ corresponds to the most frequently found, or most probable value. The picture changes significantly if different sub-populations of diffusing molecules are present, or if one molecule changes its diffusional behaviour during its trajectory (e.g. by becomming trapped and released). In this case a more appropriate analysis of the diffusion is based on a population analysis, as explained in the following.

The individual mean square displacements $\langle r^2(t)\rangle$ for every time lag $t = n\delta t$ (defined as above) can be obtained by analysing the distribution $p(u,t)$ of squared displacements (where r^2 is substituted by u) for the relevant time lag:

$$p(u,t) = \frac{1}{\left\langle r^2(t)\right\rangle}\exp\left(\frac{-u}{\left\langle r^2(t)\right\rangle}\right) \qquad (11)$$

$p(u,t)$ is often given in the form of a histogram (figure 16a).

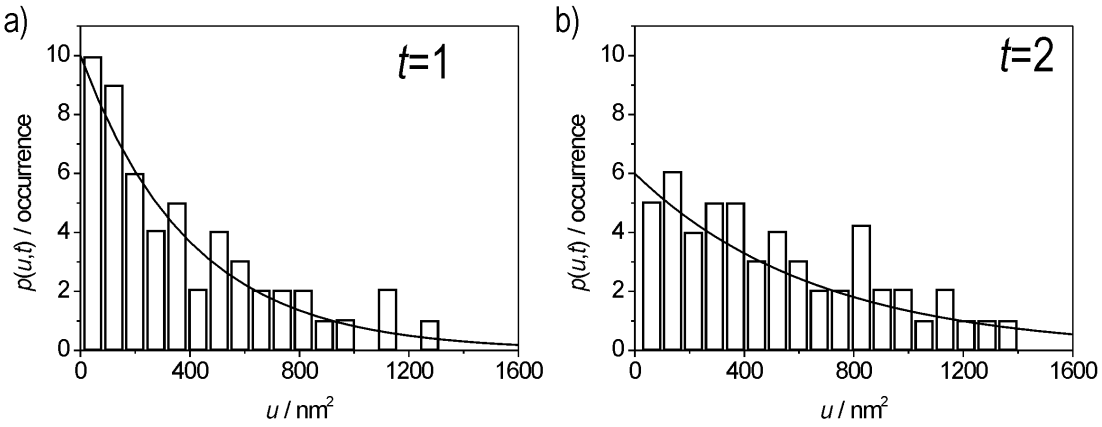

Figure 16: Conventional analysis of squared step distributions via histogrammes. a) An exemplary historgram (54 steps) showing the binned data and a fit according to eq. 11 for t=1 and b) histogram and fit for t=2 (53 steps).

A more elegant way to analyse diffusion, that avoids the necessity of artificially binning the data to obtain histograms is based on a statistical population analysis. The cumulative probability $P(U,t)$, or the probability to find a squared step between 0 and U, is given by the integral betweeen 0 and U over $p(u,t)$. The complementary function, $C(U,t)$gives the probability to find a squared step larger than U (see figure17a).

$$P(U,t) = \int_0^U p(u,t)\,\mathrm{d}u = 1 - \exp\left(\frac{-U}{\left\langle r_i^2(t)\right\rangle}\right) \qquad (12)$$

The complementary function (i.e. the probability to find a particle between 0 and infinity)

$$C(U,t) = 1 - P(U,t) \qquad (13)$$

is an exponential decay with decay constant $\langle r^2(t)\rangle$ (adapted from [Schmidt96]; see figure 17b).

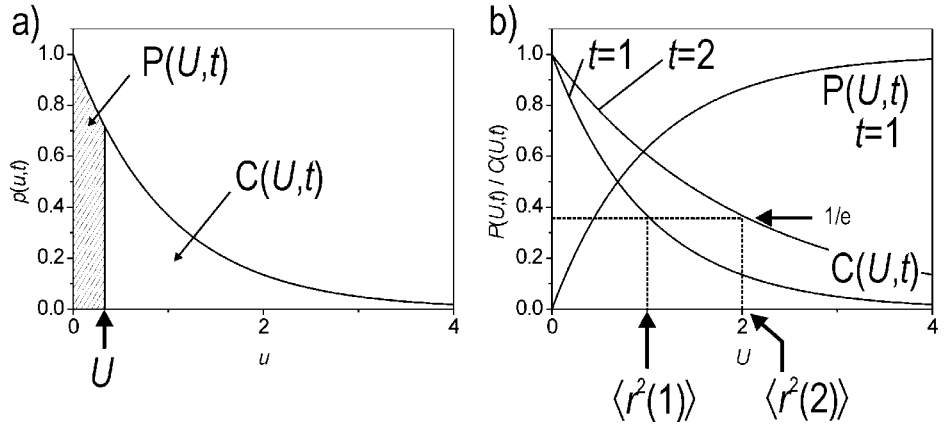

Figure 17: Population analysis. a) Starting from the histogram it is possible to compute the cumulative probability $P(U,t)$ and the complementary function $C(U,t)$. b) $P(U,t)$ and $C(U,t)$ are plotted versus U. $C(U,t)$ is plotted for two times t=1 and t=2.

$C(U,t)$ is obtained from the experimental values of the individual squared displacements U, by sorting the values (longest squared step first) and assigning each a rank relative to the total number of steps j/N (N is the total number of steps).

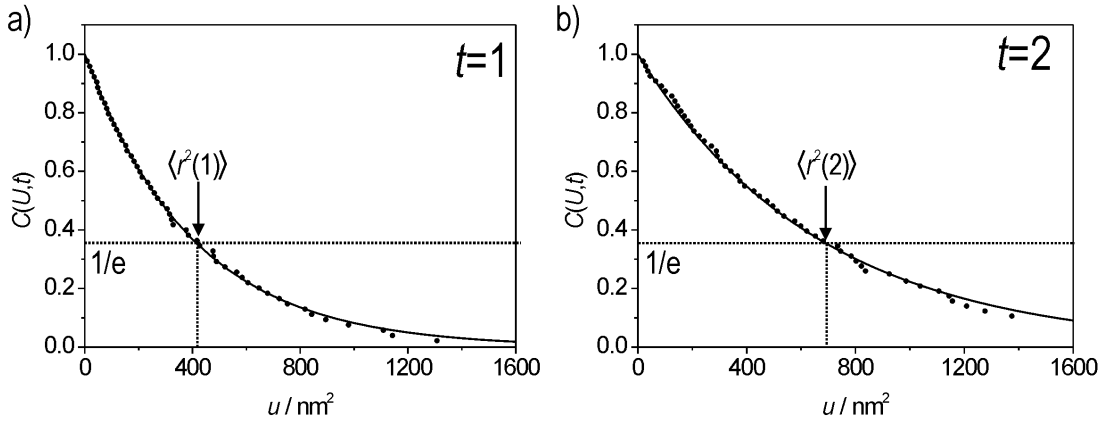

Figure 18: Ranked data corresponding to $C(U,t)$. The graphs in a) and b) were generated using the same set of data from figure 16; note that the graph appears significantly smoother because the data was not binned.

The relative rank j/N of a specific squared displacement U gives the percentage of how many molecules have a smaller rank, or have a larger squared displacement - between U and infinity. This corresponds directly to $C(U,t)$. This is shown in figure 18 for the same data set used to generate the histograms in figure 16. Note that the curve is visibly smoother, because it is not binned.

If a number (m) of sub-populations with different diffusion behavior are present, equation 11 becomes the sum of the individual distributions:

$$p(u,t) = \sum_{i=1}^{m} A_i \frac{1}{\left\langle r_i^2(t) \right\rangle} \exp\left(\frac{-u}{\left\langle r_i^2(t) \right\rangle} \right) \qquad (14)$$

with relative amplitudes A_i (and the sum over all A_i being unity) The cumulative probability is thus:

$$P(U,t) = \int_0^U p(u,t)\, \mathrm{d}u = 1 - \sum_{i=1}^{m} A_i \exp\left(\frac{-U}{\left\langle r_i^2(t) \right\rangle} \right) \qquad (15)$$

The complementary function $C(U,t)$ (i.e. equation 13), is for m sub-populations a sum of exponential decays with decay constants $\langle r_1^2(t) \rangle$, $\langle r_2^2(t) \rangle$, ... $\langle r_m^2(t) \rangle$. The ranked data can then directly be fitted to a mono- bi-, tri- (and so on) exponential decay, which gives the respective decay constants for the m populations $\langle r_1^2(t) \rangle$, $\langle r_2^2(t) \rangle$, ... $\langle r_m^2(t) \rangle$.

The mean squared displacements obtained in this way can be evaluated against the time-lag t. For example, if different sub-populations are undergoing normal isotropic diffusion, with different diffusion coefficients, the respective diffusion coefficients D_i are obtained via linear regression through the respective $\langle r_i^2(t) \rangle$ versus t plots using equation 6.

The same type of analysis can be used to characterize the distributions of step sizes for m different sub-populations (again, with the sum of the relative amplitudes A_i being unity). The normalized distribution function of step lengths is:

$$q(r,t) = \sum_{i=1}^{m} A_i \frac{2r}{\left\langle r_i^2(t) \right\rangle} \exp(-r^2/\langle r_i^2\ (t)\rangle). \qquad (16)$$

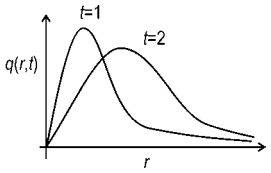

The cumulative probability, or the probability to find a step with a length between 0 and R) distribution is thus

$$P(R,t) = \int_0^R q(r,t)\, \mathrm{d}r = 1 - \sum_{i=1}^{m} A_i \exp\left(\frac{-R^2}{\left\langle r_i^2(t) \right\rangle} \right). \qquad (17)$$

The complementary function (the probability to find a setp larger than R)

$$C(R,t) = 1 - P(R,t) \qquad (18)$$

in the case of m sub-populations is a sum of m Gaussians centered at origin, with characteristic widths $\langle r_1^2(t)\rangle$, $\langle r_2^2(t)\rangle$, ... $\langle r_m^2(t)\rangle$. Again, the relative ranks of the experimentally obtained step lengths correspond directly to $C(R,t)$.

Using the described population analysis to determine the mean value (or mean values), has a series of advantages over other types of analysis that are based on making arbitrary cuts in the trajectory (for example around an area of reduced mobility that may appear to be particularly well-pronounced) or setting arbitrary binning and treshold values in the analysis of histograms. Firstly, there is no necessity to introduce these artificial parameters. Secondly, this approach is sensitive towards the presence of sub-populations that may not be well-pronounced or otherwise visibly obvious from the data. If a sub-population exists with statistical significance it is readily detected by this approach.

2.3.3. Methods in Comparison: The Measurement of Diffusion

A broad variety of methods can be used to study diffusion in porous materials. A brief overview and comparison is given in this section to put the experimentally obtained characterizations (via single molecule tracking) into a broader context.

Conventional, macroscopic approach: Methods based on the macroscopic approach evaluate the change of concentration in space with time $c(x,t)$ using solutions to the Fickian equations (eqs 2,3). $c(x,t)$ is monitored directly, for example via fluorescence (e.g. fluorescence recovery after photobleaching, FRAP, where the diffusion of a fluorescent dye into a photobleached area is observed), IR or NMR signals, as the concentration is directly proportional to the signal intensity. The major advantage of this approach lies in its simplicity and in the fact that it is not restricted to any particular type of molecule (e.g. fluorescent dyes). Limitations of this approach are: (a) The diffusion process has to be synchronized in some way for it to become observable. (b) The gained data does not contain the information availiable from the trajectories of the individual diffusing particles and depends on a series of assumptions.[Saxton97]

SMS / microscopic approach: The most straightforward method for the observation of diffusion is based on the direct observation of the individual diffusing particle (e.g. a fluorescent molecule). Diffusion parameters, such as the diffusion coefficient, the distribution of step sizes and angles between steps are obtained directly from the trajectory of the diffusing particle as described in the previous sub-sections. The major advantage of this method is that it allows to characterize diffusion in a very thorough way, because it does not discard the information contained in the individual trajectories for the analysis. It is possible to resolve different types of diffusional sub-populations and to visualize structural features in the trajectory directly (e.g. the appearance of fast or slow steps, or the presence of diffusional traps). This method is limited by the experimental equipment used. SMS measurements are typically limited to diffusional processes in which the observed diffusing particle is present in very low concentrations

(typically 10^{-9} or 10^{-10} M), and to slow diffusional processes (typically, with diffusion coefficients below 10^{-7} cm^2s^{-1}).

Another more indirect SMS method is based on the statistical analysis of the amount of particles, or molecules, diffusing in and out of a well-defined volume. This method is called fluorescence correlation spectroscopy (FCS). This approach determines the typical time a molecule stays in a given volume (eg. a confocal detection ellipsoid) by analysis of the autocorrelation function of intensity $g^{(2)}(\tau) = \langle I(t)I(t+\tau)\rangle\langle I(t)\rangle^{-2}$. Typical concentrations of particles, or molecules for diffusion measurements are in the order of 10^{-8} M. The major advantage of this method is that it is capable of resolving very fast dynamic phenomena (diffusion, rotation, triplet blinking) taking place on a time scale of 0.1 μs. Very slow or rare processes however are not sensed by this method. Another limitation of this method is that the autocorrelation function has to be matched to a hypothetical expression derived from a model of the diffusion process in order to obtain a parameter like the diffusion coefficient. Also, the spatial information contained in the individual trajectories is discarded by this technique.

Other methods: Among other methods that can be used to analyse diffusion are: Pulsed-field-gradient NMR, or PFG-NMR [Kukla96], quasi-elastic neutron scattering, or QENS [Benes01]. The strength of these methods lies in the possibility to probe the diffusional behaviour of any diffusing species, like water, methane and xenon, and are not restricted to the comparatively large fluorescent dye molecules.

In PFG-NMR, the individial spins of the nuclei in a molecule are subjected to a pulsed magnetic field gradient (FG) between the pulses of a spin-echo experiment. (The pulse sequnce using NMR notation is: π/2-FG-π-FG- echo). The effect of the field gradient is that the molecules will have different Larmor frequencies depending on where they are situaded spatially in the field gradient. After the refocussing pulse (π) the same gradient is applied so that all spins refocus and deliver a full spin-echo signal. If the molecules diffuse the second gradient will fail to refocus all the spins, causing the spin-echo signal to become attenuated. The amount of attenuation thus relates to diffusion. PFG-NMR is

'limited' to molecules with NMR-active nuclei and to a high concentrations of diffusing particles. The rule of thumb for ^{1}H-PFG-NMR, for example is 1 proton per nm^3. [Kärger, personal communication]. As an ensemble method PFG-NMR also fails to determine whether one molecule shows a heterogenous behaviour, or if a heterogeneity is caused by separate sub-populations of molecules coexisting in the same sample.

QENS probes the energy spectrum of neutrons which collide with the atoms of a diffusing species in a sample. If the collision is completely elastic, the energy of the scattered neutron will remain unaffected by the collision, unless the particle with which it collides is also moving due to translation, rotation or vibration (hence the term 'quasi'-elastic). These three movement components can be treated independently, since they occur on different time-scales.[Benes01] In the case of neutron collisions with diffusing molecules, additional components get added to and subtracted from the neutron's energy, causing the energy spectrum to broaden. The amount of broadening can be related to translational diffusion.[Benes01] The big disadvantage of QENS is that it is experimentally very eleaborate (i.e. it requires a source of monochromatic neutrons), and that the final results are heavily dependent on the assumption of models.

Method	Conc. [M]	D [cm^2s^{-1}]	Limited by:	e.g. Ref.
PFG NMR	$> 10^{-12}$	$< 10^{-4}$	Concentration	[Kukla96]
QENS	$> 10^{-12}$	$< 10^{-4}$	Concentration	[Benes01]
FRAP	$> 10^{-13}$	$< 10^{-4}$	Concentration	[Saxton97]
SMS-FCS	10^{-13} - 10^{-20}	10^{-8} - 10^{-4}	Bleaching	[Eggeling98]
SMS-SPT	10^{-14} - 10^{-20}	10^{-14}-10^{-8}	Frame Rate	[Schmidt97]

The table above resumes the most important specifications for the described techniques. The concentration of diffusing particels is the limiting factor for all ensemble measurements. The limiting factor for FCS is the photobleaching rate: Very slowly diffusing molecules would photobleach before they leave the irradiation area, leading to an artificially high diffusion coefficient. In SPT the limit is given by the speed with which an apparatus can record a sequence of images.

3. Experimental Setup and Background

The materials presented in the preceding chapter, the host-guest materials consisting of an organic dye molecule incorporated into the channels and voids of a molecular sieve are examined using fluorescence microscopy and SMS. In this chapter the experimental techniques used to acquire and to evaluate the data are discussed.

This chapter is subdivided into two sections: The first describes the used optical microscopy equipment, the confocal and widefield imaging setups, starting with the basic theoretical background of these microscopy techniques. The emphasis of this chapter lies on the second section, which deals with the automated analysis of data. Different sets of programs were conceived and written in order to (a) obtain the relevant information from the extensive amount of raw-data produced by the experimental equipment (for example, to obtain trajectories of many individual diffusing patterns from large sequences of microscopy images) and (b) to evaluate the gained information (for example to analyse the obtained trajectories in order to characterize the diffusional behaviour).

3.1. Microscopy Techniques

Spatial Resolution in Microscopy: The idea behind microscopy is to obtain information from small regions in space. The central question for any type of microscopy is thus, how small such a region can be: The smaller the region, the better the spatial resolution becomes. In optical microscopy, it can be shown that the spatial resolution is limited. The schematic illustration in figure 19 shows the necessary definitions and parameters that will be used in the following discussion.

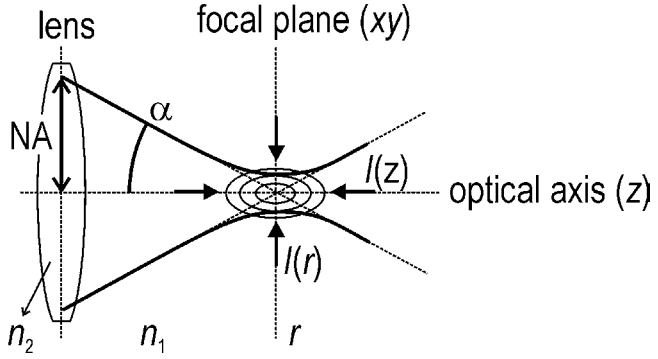

Figure 19: Schematical picture illustrating the basic parameters and definitions used in the calculation of the spatial resolution of a microscopy apparatus.

A lens can neither focus light onto a point in space nor can it collect all the light coming from a point source in the focus. This is so, because it has a finite size and ultimately because of the existence of an angle of total reflection (α). This limited, effective size of a lens is characterized by a collection or focusation cone, described by the numerical aperture (*NA*) of the objective lens (see fig.19). The *NA* is defined as

$$NA = n_1 \cdot \sin \alpha, \qquad (19)$$

where n_1 is the refractive index of a the medium between the lens and the object. The angle of total internal reflection is defined as $\alpha = \arcsin(n_1/n_2)$, with n_2 being the refractive index of the lens and $n_2 > n_1$.

The main consequence of this limited size of the focusation cone is that the image of an object, projected onto the focal plane, will not contain the entire phase information needed to reconstruct the exact image of the object by interference. This loss of (phase-) information is finally what causes images to appear less sharp (see fig.20).

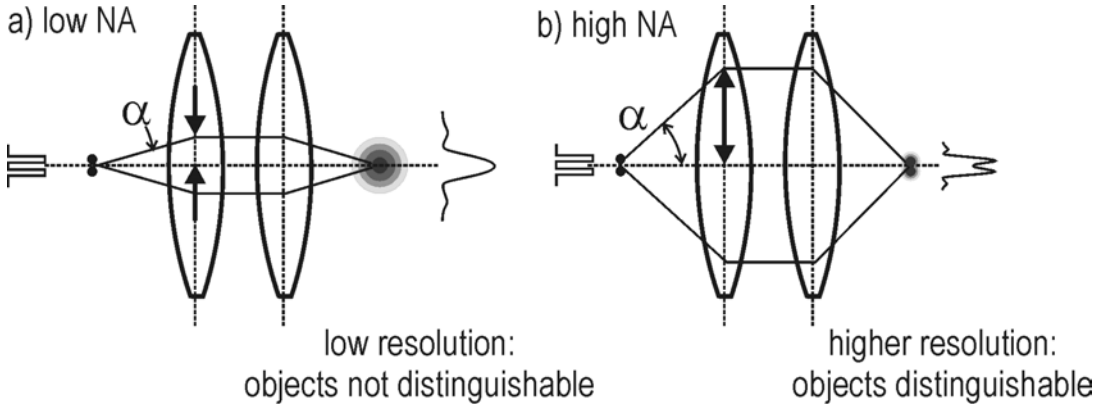

Figure 20: Influence of the nummerical apperture (*NA*) on the sharpness of an image. a) A lens with low *NA* produces blurred images. b) A lens with a higher *NA* collects a larger cone of light rays from the object (i.e. obtaining more phase infomation) and produces sharper images.

In effect a point-like object will appear as a diffraction pattern with a finite width. The intensity map of this pattern and its characteristic size can be used to characterize the resolution. This intensity map can be calulated for an idealized point-source for the different types of microscopy in dependence of the wavelength of the light in question (λ), of the *NA* and of the illumination and detection geometries. The resulting distribution function, $I_{PSF}(x,y,z)$ is called the point-spread function (PSF) of the optical apparatus. The PSF results from the convolution of the illumination and detection probabilities in space, $I_{ill}(x,y,z)$ and $I_{det}(x,y,z)$.

$$I_{PSF}(x,y,z) = I_{ill}(x,y,z) \cdot I_{det}(x,y,z) \qquad (20)$$

Because of the cylindrical symmetry of most microscopy arrangements $I(x,y,z)$ can commonly be noted as $I(r,z)$, where r is in an arbitrary direction parallel to the focal-plane of the microscope, and z is the optical axis.

The illumination and detection probabilities vary for different types of microscopy, resulting in different PSFs and in a series of advantages and limitations for the respective type of microscopy. The PSFs will be described in more detail below for the two different fluorescence microscopy techniques used in this work: confocal microscopy and widefield imaging microscopy. Other types of optical microscopy are covered for example in [Stelzer94], [Jung01] and [Seebacher02d]. Recent developments in fluorescence microscopy (e.g. using stimulated emission depletion) are covered in [Hell03] or [Hell04]; total internal reflection microscopy is covered in [Funatsu95] and [Ambrose99]; near field scanning optical microscopy is covered in [Hecht00] and [Dereux00].

3.1.1. Confocal Microscope

The basic idea behind confocal microscopy lies in the spatial superposition of the illumination and detection foci. As a consequence the illumination and the detection probabilities are nearly identical $I_{ill}(r,z) = I_{det}(r,z)$. Thus the intensity distribution of the PSF becomes:

$$I_{PSF}(r,z) = I_{ill}(r,z)^2 \qquad (21)$$

$I_{ill}(r,z)^2$ can be calculated. The exact result [Richards59], [Webb96], [Hell93] is difficult to handle mathematically. For most purposes, however, $I_{ill}(r,z)$ can conveniently be separated into a lateral $I_{ill}(r)$ and axial component $I_{ill}(z)$ and both components approximated by simple Gaussians (in figure 21 this is shown for the lateral component):

$$I_{ill}(r)^2 = I_0 \exp(-r^2/2w_r^2) \qquad (22) \quad \text{and} \quad I_{ill}(z)^2 = I_0 \exp(-z^2/2w_z^2) \qquad (23)$$

In equations 22 and 23 the widths w depends on the used wavelength λ, on the NA and on the refractive index n_1. They are empirically found to be $w_r = 0.15 \cdot \lambda \cdot NA^{-1}$ for the lateral component and $w_z = 0.54 \cdot n\lambda \cdot NA^{-2}$ for the axial component. The full-width at half-maximum, $FWHM$, of these distribution functions are often used to characterize the resolution limit, or the minimal distance between two point-like objects, so that they still can be distinguished. The lateral $FWHM_{lat}$ and axial $FWHM_{ax}$ are:

$$FWHM_{lat} \approx 0.36\ \lambda \cdot NA^{-1} \qquad \text{and} \qquad FWHM_{ax} \approx 1.27\ n\lambda \cdot NA^{-2} \qquad (24, 25)$$

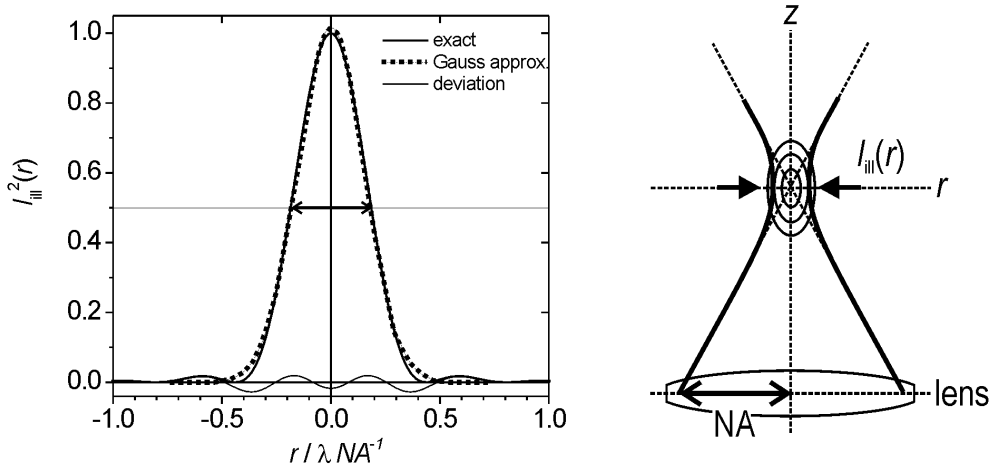

Figure 21: The exact intensity distribution function for the confocal PSF can be approximated by a Gaussian. The FWHM can be used to characterize the resolution limit.

Experimentally, the focussed illumination is achieved by illuminating the specimen through the microscope objective with laser. The focussed detection is achieved by placing a spatial filter, a pinhole, in the detection pathway (as schematically illustrated in figure 22a). Note that strictly the factors 0.36 and 1.27 in equations 23 and 24 will also depend on the size of the pinhole pupil in detection. The given factors were obtained for the ideal case in which the pinhole corresponds exactly to the size of the focus.

The real, or effective resolution obtained with an experimental apparatus is usually worse than that obtained from the idealised equations. There are various reasons for this

discrepancy: (a) The pinhole is usually larger than the ideal size, (b) the optical elements (mirrors, lenses, etc.) are not perfect, (c) The refractive index between the object and the objective lens is typically inhomogenous. (d) The illumination beam is not perfectly collimated and not strictly monochromatic, and so is (e) the detection beam.

The ideal resolution volume element can be described by an ellipsoid with the diameters corresponding to the FWHMs given in equations 23 and 24. In figure 22b the size of the ellipsoid is depicted using λ=633 nm, NA=1.3 and n_1=1.51 (immersion oil). The effective resolution ellipsoid (for the same conditions) is depicted in fig 22c. It was obtained experimentally, by acquiring a three-dimensional fluorescence pattern of a point-like emitter, for example an individual molecule - as it is considerably smaller than the wavelength in question.

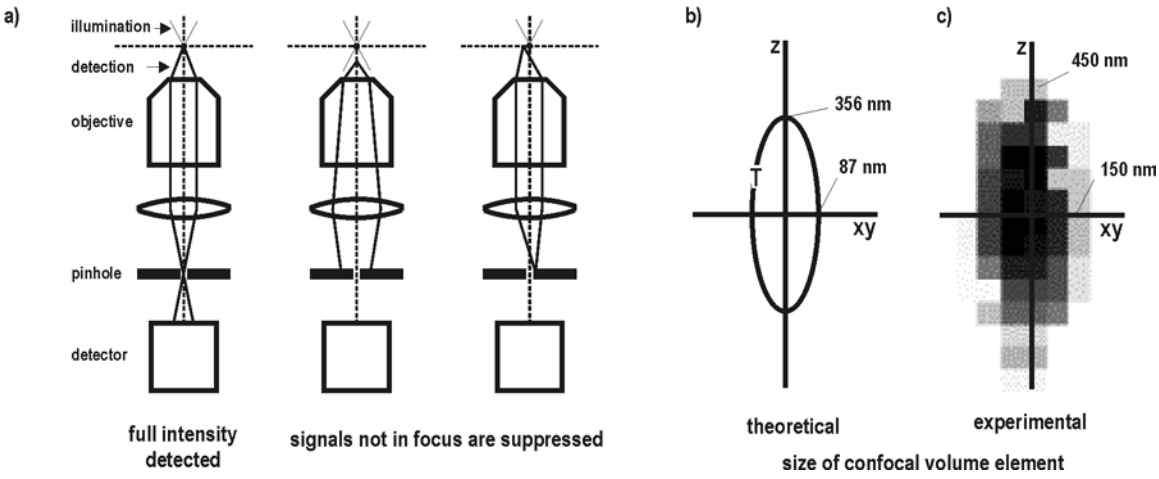

Figure 22: Confocal microscopy. a) Illumination and detection geometry. b) The theoretical size of the confocal volume element (using λ = 633 nm, n=1.51 and NA = 1.3). c) Experimental size of the confocal volume element (single molecule spot, λ_{ex} = 633 nm, n_1=1.51 and NA = 1.3; 78 nm per pixel). In b) and c) the z-axis corresponds to the optical axis, and the xy-plane to the focal plane.

Experimental setup: The confocal microscope used in this work is based on a commercially availiable Zeiss model LSM 410, schematically depicted in fig. 23. A series of modifications were implemented on the LSM410, making it a versatile tool that can be used in single moelcule microscopy and spectroscopy. These will be explained in more detail below.

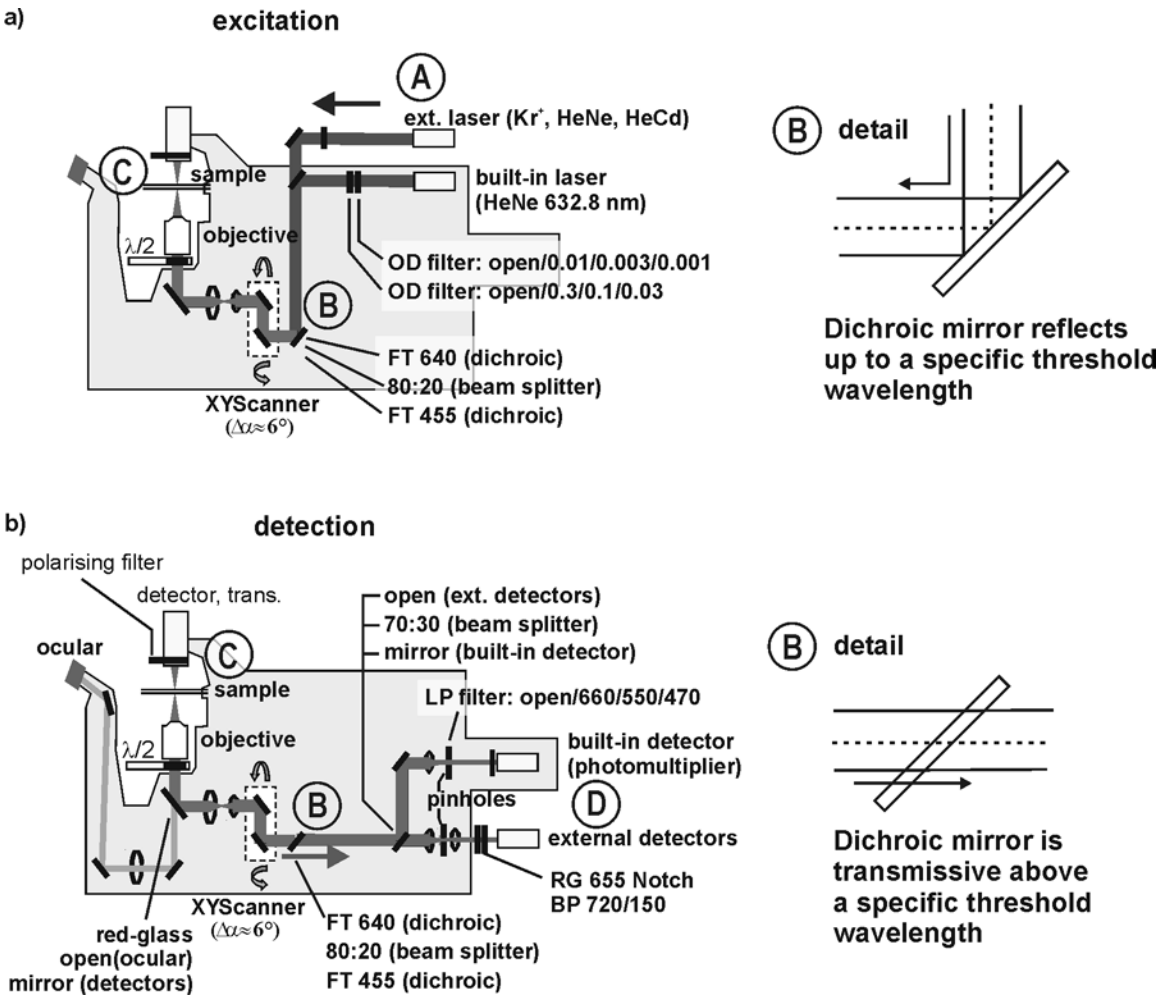

Figure 23: Schematics of the used confocal microscopy setup based on a Zeiss LSM410. a) Excitation arrangement. b) Detection arrangement.

The specifications of the used lasers (A in fig. 23) are gathered in the following table:

Laser	λ_{ex} **/ nm**	I_{ex} **/ µW (*)**
HeCd	442	45
Kr+	532	20000
Kr+	568	20000
HeNe	594	3000
HeNe (int)	633	34

(*)maximum measured at objective barrel entrance (not attenuated)

All laser beams are collimated and directed to the scanning unit via a (suitable) dichroic mirror (B in fig. 23a). The laser beams are expanded and directed to the objective barrel to excite the sample (C in fig.23a). The maximum intensities of the used lasers given in the table above are measured at the entrance of the objective barrel. The typical excitation intensities for single molecule experiments lie between 1-50 µW.

The fluorescence of the sample (C in fig. 23b) is collected by the microscopy objective and is directed to the dichroic mirror (B in fig.23b). Red-shifted fluorescence light passes the dichroic mirror and is separated from unspecific or backscattered excitation light. The fluorecence light can then be routed to a series of detector units (D in fig. 23b).

Data / Image acquisition: One of the consequences of the superposition of the detection and focal volumes is that the only intensity originating in the focal spot of the microscope objective is detected. This gives rise to three different types of data acquisition: (a) The confocal volume element can be placed in the sample at a specific position (in x, y and z), and can consequently be used to monitor intensity changes at a specific position of the sample or to address individual fluorescing molecules if they are isolated at a specific position. In this mode it is possible to record intensity transients (fluorescence dynamics, polarization dependencies) and fluorescence spectra from a specific molecule or from a specific position in a sample. (b) The confocal volume element can be scanned across an

xy-plane at a given depth *z*. The resulting two dimensional images are optical cross sections of the sample at a specific depth *z*. (c) Finally, it is possible to gradually vary the depth *z* and make an *xy*-scan at different depths. In this way it is possible to reconstruct a three-dimensional image of the investigated specimen (cf. figure 24).

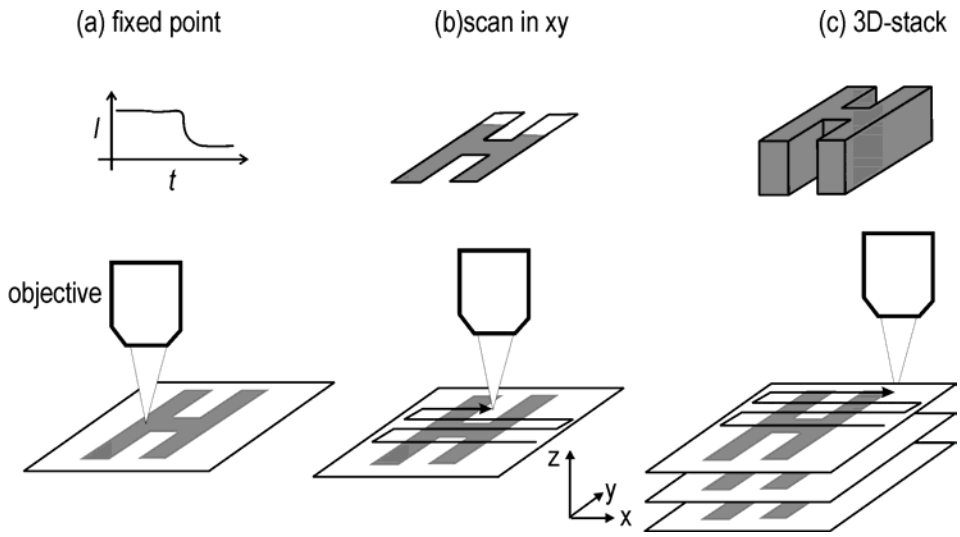

Figure 24: Image acquisition modes using the confocal microscope. (a) recording intensity from a fixed point in the sample. (b) xy-scans result in optical cross-sections (images) of the sample. (c) By varying the depth (z) a 3D image of the specimencan be reconstructed.

Temporal resolution: In case (a) - i.e. acquiring fluorescence from a specific point in the sample - the temporal resolution is limited only by the used detector and/or software. It can be as good as 100 ns, for example, using an autocorrelator device like the ALV-500. (b) The time resolution for the acquisition of a two-dimensional cross-section can be varied by adjusting the speed of the *xy*-scanner unit, which has an upper limit. For example, an image of 256 x 256 pixels cannot be recorded in less than 0.5 s with the LSM 410 hardware. (c) The time needed to record a stack of two-dimensional images is the product of the number of stacks multiplied with the time required to scan an individual cross-section (in the *xy*-plane) and with the time needed to move the objective to the next position on the *z*-axis. For example, a stack of 20 images of 256 x 256 pixels cannot be acquired in less than 20s with the LSM410.

Detectors / Modifications: The built-in detector of the LSM410 (a photomultiplier tube) is not sensitive enough for the detection of the fluorescence from isolated molecules. An important modification in the detection arrangement is that the fluorescence signal can be routed to more sensitive external detectors, that possibilitate SMS.

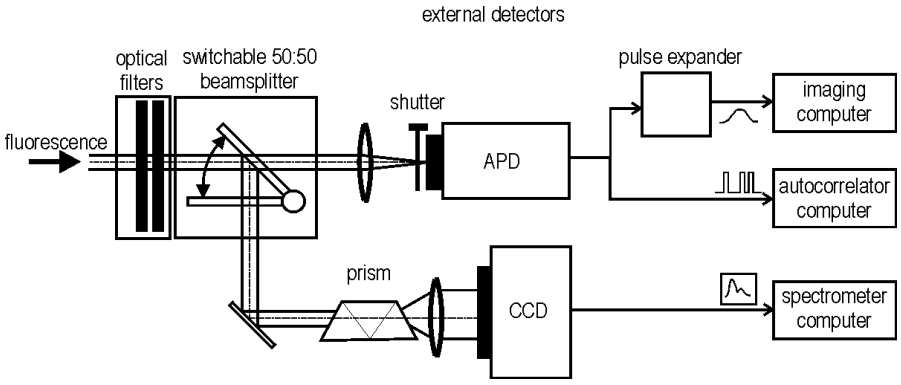

Figure 25: Schematical arrangement of the external detectors.

The two external detectors used are: (a) An avalanche photodiode, APD, which is sensitive enough to detect the comparatively weak fluorescence signal of individual molecules, and (b) a prism-CCD spectrometer, which is also sensitive enough and can be used to record emission spectra of individual molecules.

APD: The most sensitive of the detectors used in this setup is the avalanche photodiode (EG&G SPCM-AQR-141). The APD produces a 9 ns TTL pulse upon detection of a photon (50 ns dead-time; 70% detection probability in the spectral region between 600 and 800 nm). The TTL pulses can be routed directly into an autocorrelator device (ALV-500) for the anaylsis of intensity fluctuations (with a temporal resolution of approximately 100 ns), or processed by a pulse expander and re-routed to the microscope hardware to record images or intensity transients. The pulse expansion is required to convert the digital sequence of TTL pulses ('photon' / 'no photon') into a more gradual sum of pulses (≈ 'number of photons per time'), which can be processed appropriately by the microscope hard- and software. The pulse expander device also indicates the photon detection rate, and can be used to callibrate the intensity values indicated by the microscope (which are in arbitrary units).

CCD: Fluorescence light originating at the sample can be dispersed with an Amici-prism and detected with a peltier-cooled, back-illuminated CCD camera (Princeton Instruments, EEV 1300/100-EMB-chip) cf. schematical illustration in fig.26. The temporal resolution of the setup can be as good as 19 ms (with the system running instably), typically, however, sequences of spectra are obtained with a temporal resolution of 30-100 ms (depending on the fluorescence intensity). The time-limiting step for the aqcuisition of spectra is given by the chip read-out time. The spectral resolution of the setup in units per pixel varies with the dispersion strength of the prism, which in turn depends non-linearly on the respective wavelength of light The dispersion curve can be obtained empirically by imaging light with a known spectrum onto the CCD camera (cf. graphs in fig. 26). In effect, one pixel on the CCD covers between 0.5 and 2.5 nm of the spectrum in wavelengths (from 450 to 700 nm, respectively). As will be seen in detail later the spectra can be callibrated and analysed automatically.

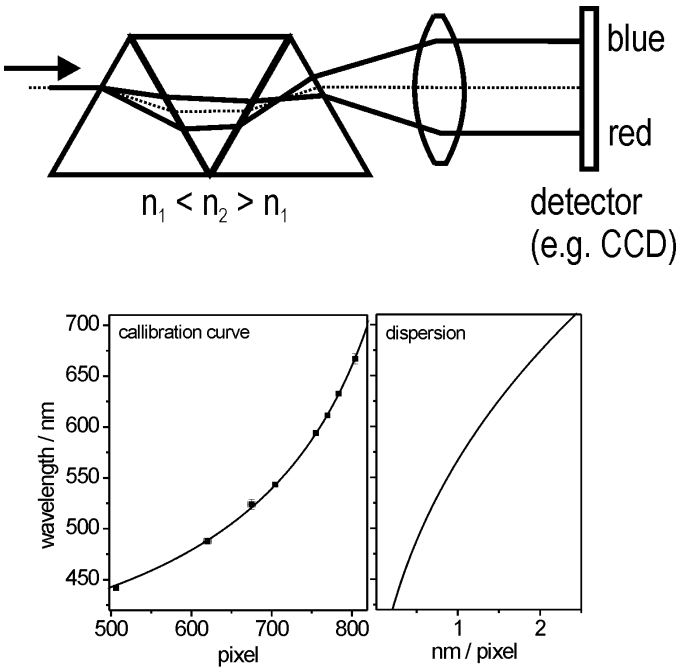

Figure 26: Schematics of the Amici-prism/CCD setup. This arrangement is particularly efficient because of the high transmissivity of the prism (*ca.* 80%) in comparison to grating-spectrometers (*ca.* 20%). Below the graphs show the non-linear dispersion of the prism.

Polarization: A further implementation on the LSM410 consists in the possibility to place polarization optics (λ/2 and λ/4 retardation plates) directly at the entrance of the objective barrel to avoid disturbing polarization dependent influences from the different optical components (like the dichroic mirror) in the excitation beam. The polarization plane of the excitation light can for example be modulated by rotating the λ/2 retardation plate continuously with a servo-motor. The polarization plane of the excitation light is monitored by a detector in transmission placed behind a polarizing filter. The setting of the polarization filter defines the frame of reference for the orientation. The modulation of the fluorescence signal in dependence of the polarization of the excitation light is recorded by the fluorescence detectors. The polarization dependent data can subsequently be analysed automatically.

3.1.2. Widefield Imaging Microscope

Widefield microscopy stands conceptually in contrast to confocal microscopy. The difference results from the used illumination geometry, which in the widefield-imaging technique is more similar to that used in conventional microscopy. A laser (A in fig. 27) is used to exitate the sample. The beam is expanded and focussed onto the back-focal plane of the microscopy objective (B in fig. 27). On the sample side the beam is parallel and illuminates the sample uniformly (C and B detail in fig. 27).

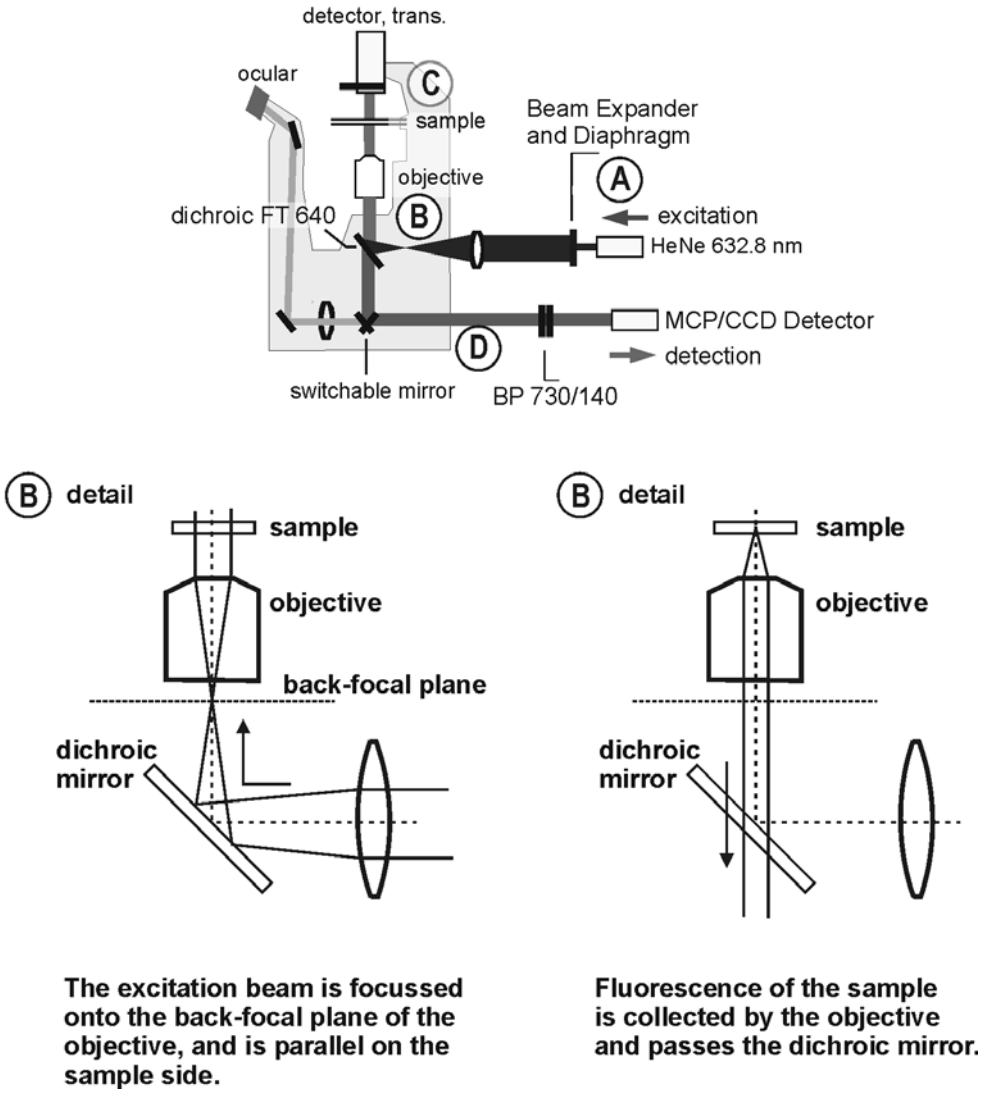

Figure 27: Widefield imaging setup based on a Nikon Eclipse TE200 microscopy stand.

Fluorescence is collected by the same objective. Residual exitation light is separated by using appropriate filters, in a similar way as shown before for confocal microscopy. The image, now originating simultaneously from the whole illuminated area is reconstructed on an area detector, such as a CCD camera (D in fig.26). The consequence for the PSF is that $I_{ill}(r,z)$ is merely a constant, because the sample is illuminated homogenously. Thus:

$$I_{PSF}(r,z) = I_{det}(r,z) \qquad (26)$$

$I_{det}(r,z)$ can be calculated and the exact result [Richards59], [Webb96], [Hell93], again, is difficult to handle mathematically. $I_{det}(r,z)$ can however be separated into a lateral $I_{det}(r)$ and axial component $I_{det}(z)$ and both components approximated by simple Gaussians:

$$I_{det}(r) = I_0 \exp(-r^2/ 2w_r^2) \qquad (27)$$

$$I_{det}(z) = I_0 \exp(-z^2/ 2w_z^2) \qquad (28)$$

with $w_r = 0.217 \cdot \lambda \cdot NA^{-1}$ and $w_z = 0.72\ n\lambda \cdot NA^{-2}$ found empirically. The full-width at half-maximum, *FWHM*, of eqns. 26 and 27 used to characterize the resolution limit are:

$$FWHM_{lat} = 0.51\ \lambda \cdot NA^{-1} \qquad (29)$$

$$FWHM_{ax} = 1.7\ n\lambda \cdot NA^{-2} \qquad (30)$$

The sizes calculated for $\lambda = 633$ nm, $n_1 = 1.51$ (immersion oil) and $NA = 1.4$ are, respectively for the lateral and axial *FWHM*s: 230 nm and 829 nm. The real sizes obtained with the microscopy setup (same conditions) are: 300 nm lateral ca. 3µm axial resolution.[Kirstein02]

Experimental setup / specifications: The setup is based on a Nikon Eclipse TE200 microscopy stand, using a 1.4 NA oil immersion objective (Plan Apochromat 100x) and a HeNe laser (633 nm 3mW power, NEC). The fluorescence images are recorded with an intensified multi-channel-plate-CCD (Pentamax / Princeton Instruments EEV, 512×512 pixel). Fluorescence light from the sample is projected onto the CCD on an area of approximately 150×150 pixels. The magnification factor, or the size of each pixel on the images can bedetermined from images of test patterns with a well-defined spacing. In all studies presented in this thesis the pixel size was 168 nm/pixel. Sequences of images can be acquired with a frame rate of 25 frames per second (or 40 ms per frame). An exemplary sequence showing patterns from individual molecules is shown in figure 28.

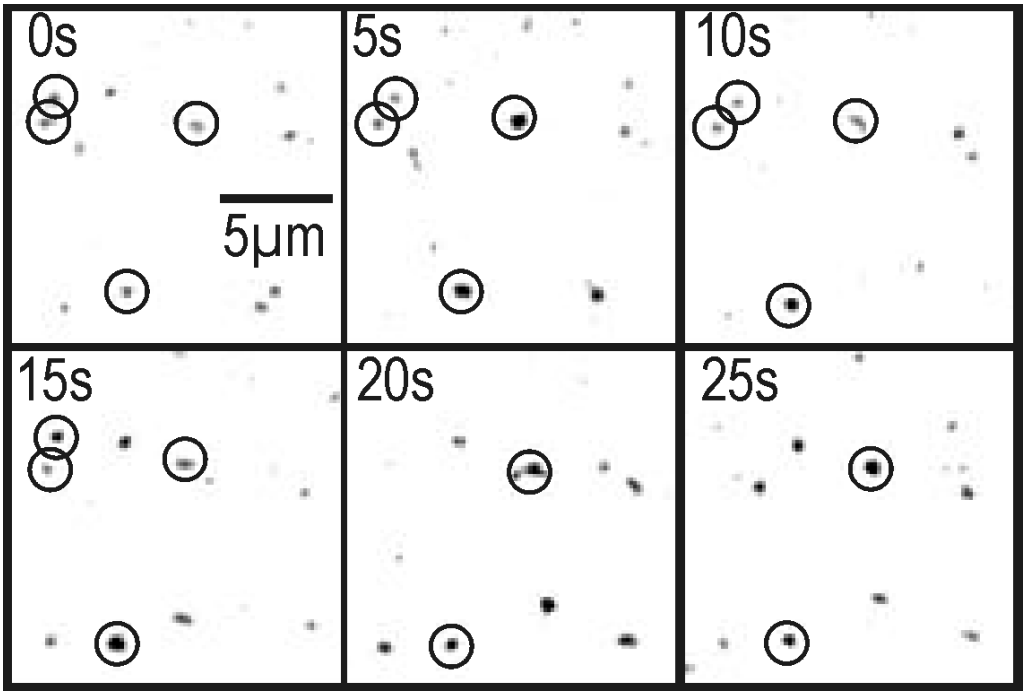

Figure 28: The typical image sequence showing individual diffusing molecules was acquired with the described widefield imaging setup.

Confocal and Widefield Microscopy in Comparison:

	Confocal LSM 410	Widefield
lateral resolution (1.3 NA / 633 nm)	300 nm	300 nm
axial resolution	900 nm	3 µm
pol. measurements	yes	no (limited)
temp. res. 1D	0.1 µs	-
temp. res. 2D	0.5 s (256 x 256)	20 ms (256 x 256)
temp. res. 3D	20 s	-
address SM's	yes	no
installed wavelegths	442 nm 534 nm 568 nm 594 nm 633 nm	532 nm 633 nm
advantages	(i) versatile, (ii) possibility to addresses individual molecules (iii) high depth resolution	(i) fast acquisition of 2D images (ii) parallel acquisition of SM signals
limitations	(i) slow acquisition of images (ii) serial acquisition of SM data	(i) limited to imaging.

3.2. Analysis Programs

The setup described in the previous sections produces an extensive amount of raw-data, in the form of (a) sequences of images (movies) showing the diffusion of individual particles, (b) sequences of spectra showing diverse forms of spectral dynamics from an individual emitter, (c) sequences of polarization dependent intensity traces that characterize the orientation of individual emitters and (d) sequences of intensity transients which can be used to characterize the photostability of a certain type of molecule. In the evaluation of this data every sub-set of data (every frame in a movie, every spectrum in a sequence of spectra, etc.) has to be analysed individually, for example callibrated or fitted. It is not feasible to evaluate this amount of data manually. Suitable programs that analyze this kind of data automatically are, however, not commercially availiable.

In the next sub-sections four different sets of programmes are presented, which have been conceived and written in order to evaluate the different types of data automatically. The first set of programmes are utilized in the tracking of individual diffusing particles in a sequence of microscopy images. The second set of programmes are used in the analysis of spectral parameters. The third set is used to evaluate polarization dependent data to determine the orientational angles of individual molecules. The last set of programmes was written in order to obtain photostability parameters of the used dye molecules such as a number of emitted photons prior to photobleaching and typical on and off-times.

3.2.1. Evaluation of Diffusion

This sub-section is subdivided into two parts. The first part describes how the tracking programme recognizes the patterns of diffusing particles in a sequence of microscopy images and how accurately it obtains the position of the pattern in an image. The second part describes how the obtained positions of the individual patterns, that make up the trajectories of the molecules, can be analysed in order to obtain diffusional parameters, like the diffusion coefficients and step-size distributions.

3.2.1.1. Automated Tracking

The automated tracking programme obtains the positions of well-defined patterns in a sequence of images consisting of *m* individual frames. An exemplary excerpt from a sequence with diffusing patterns from individual molecules is shown in figure 29.

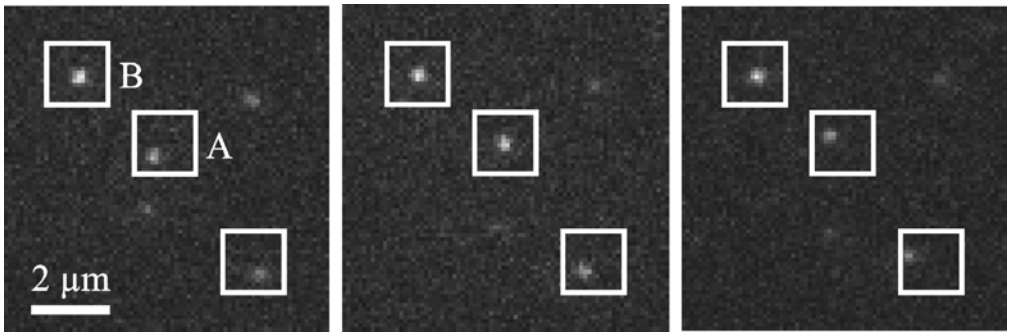

Figure 29: The fluorescence of individual molecules are detected as diffraction limited patterns on a sequence of microscopy images. In this figure the individual frames are separated by approximately 0.25 s. Note the movement of molecule in square A relative to the molecule in square B. Image taken from [Hellriegel05].

The patterns originating from the fluorescence of individual molecules can be approximated by a two-dimensional Gaussian:

$$R_n(x,y) = A_n \exp\left(-\frac{(x-x_{0,n})^2+(y-y_{0,n})^2}{2\sigma_n^2}\right) \qquad (31)$$

In this equation $R_n(x,y)$ is the approximated intensity distribution of a pattern on a two-dimensional plane in the *n*-th frame. A_n is the amplitude of the two-dimensional Gaussian (given in arbitrary units). Parameter σ_n is related to the full width at half maximum, FWHM, of the pattern by FWHM = $\sigma_n \sqrt{4\ln 4}$ or FWHM = $2.355\sigma_n$. The parameters $x_{0,n}$ and $y_{0,n}$ give the central positions of the fitted pattern, in units of pixels. The size of the pixels in units of nanometers varies with the magnification used to project the images

onto the plane of detection. This size is determined by acquiring reference images of objects with a known size, or by calculating the exact magnification used.

To obtain the central positions of a pattern in a frame *n*, the part of the data that contains the pattern (a two-dimansional pixel versus intensity map, in the form of a matrix) is fitted according to eq. 31. Fig. 30 illustrates the fitting procedure. The experimentally obtained intensity map (left) is subtracted from the fit according to equation 31 (middle graph) giving the residue plot (right graph). With 100 nm per pixel, the integral area exceeds 5σ. The SNR in this example is ca. 7 ($\xi \approx 0.143$) and the error for the position in this case is 35 nm.

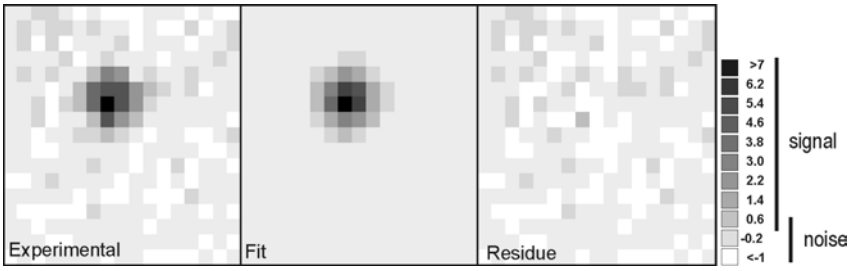

Figure 30: Demonstration of the 2D fitting process. An experimental signal (left) is subtracted from the fit (middle) producing the residue plot (right). $\xi \approx 0.143$.

The obtained coordinates for this frame are then written to a file and used as an initial guess for the fitting of the pattern in the subsequent frame *n*+1. In this new frame the diffusing pattern will be located at a slightly different position in the image, but still close to the position found in the previous frame. The fitting procedure finds its position, writes it to the file and uses the new posion as an initial guess for the next frame *n*+2. This iterative procedure is interrupted if a pattern vanishes (e.g. due to photobleaching, blinking, diffusion out of the focal plane, etc.). When this is the case a new pattern (a new molecule) can be selected and the procedure is repeated for that next pattern.

The output file is an array consisting of the pattern number, the frame number, the fit parameters and their respective errors. The sequence of *xy*-coordinates for a specific pattern, for example, gives the two-dimensional spatial trajectory of the respective molecule. Before turning to the analysis of the trajectory file with a second programme, a few considerations on the fitting accuracy and its relation to the errors of the parameters are given.

Fitting accuracy: One of the central concerns in the evaluation of trajectories is the error or the accuracy with which the individual positions of the trajectory can be obtained. Many algorithms can be used to find the central position of a pattern, for example, the evaluation of the center of mass or finding the peak, median or mean value of the pattern. The error, however, is not usefully estimated by these methods. This is not the case for well-defined fitting procedures. The errors in the fit parameters (e.g. the errors for the four parameters of equation 31, dA_n, $dx_{0,n}$, $dy_{0,n}$ and $d\sigma_n$) are related to the overall fitting accuracy, which in turn can be shown to depend on the relative noise ξ (the inverse of the signal-to-noise ratio) and on the data density.[Bobroff86], [Lampton76]
This can be demonstrated in more detail for the used χ^2 (or maximum likelihood) fitting algorithm using only one fit parameter. The χ^2-method compares the experimental data with the model function $R(x)$ in dependence of the fit-parameter and gives a value, χ^2, that describes the discrepancy between the data and the fit. The discrepancy is smallest, that is χ^2 reaches a minimum, when the parameter fits best. Variation of the parameter about the best fit value will increase χ^2 indicating a less likely probability that the parameter is the correct one. The underlying equation according to [Bobroff86] is:

$$(x_{0,n} - x_n)^2 \cong \frac{c}{\int_{-L}^{L} \frac{1}{\xi^2(x)} \left[\frac{\partial R(x)}{\partial x_n}\right]^2 dx} \qquad (32)$$

Where $x_{0,n}$ is the best fit parameter (e.g. the central position of a Gaussian), x_n a less ideal value and c is the confidence level. For the time being, the integral in the denominator will be taken as constant. The first consequence of eq. 32 is that the confidence is zero if

$x_{0,n} = x_n$ and that it increases the more x_n deviates from $x_{0,n}$. The absolute difference between the fit values $|x_{0,n}-x_n|$ represents an error for a given confidence level. If the confidence level is chosen to be 68% the error will correspond to the standard deviation (or '1σ' deviation).

We turn now to the integral in the denominator of eq. 32. The fixed level of confidence c (say 68%) is directly proportional to $(x_{0,n}-x_n)^2$, and the proportionality coefficient is the integral. The contribution of the integral is biggest in the area with the highest difference in signal (the squared differential is large). The influence of the noise $\xi(x)$ can be estimated in a first approximation by assuming it is independent from x and taking the integral as constant for small differences in x_n. Equation 32 is thus simplified to:

$$\mathrm{d}x_{0,n} = |x_{0,n} - x_n| \cong \xi \cdot C \,. \qquad (33)$$

with all constants gathered in C. That is: The error is directly proportional to the relative noise ξ.

The integral, however, is not constant, and depends on (a) the fitting model, and (b) on the boundaries $-L$, $+L$. The contribution of the integral is highest, at the positions which suffer the biggest changes with variation of the parameter x_n, or positions which contain most of the signal edge. This has two basic consequences: First, if the boundaries of the integral cut the signal at a region where $\partial R(x)/\partial x_n$ is big, then the integral becomes small, and the error increases. Second, adding regions with no signal (that is, merely increasing the integration boundaries $\pm L$) will not significantly reduce the error.

Both assertions, (a) the direct proportionality between error and noise, and (b) the effect of different integral boundaries on the error can be verified experimentally, using, for example single molecules (producing different SNR) as idealized point-like emmitters in fluorescence microscopy, and by subsequently fitting the obtained data to the two-dimensional Gaussian given above in equation 31.

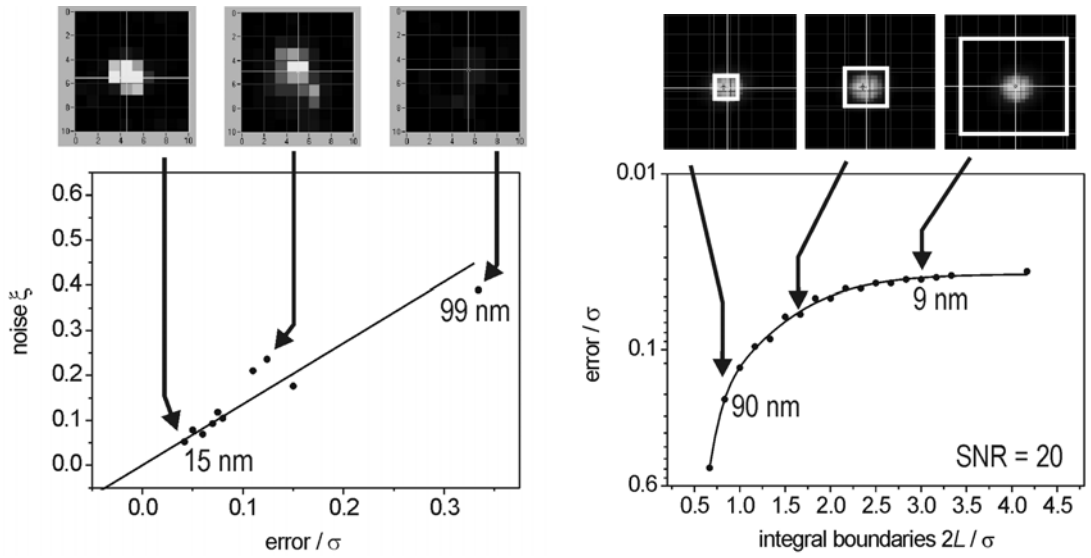

Figure 31: The error of a fit-parameter is directly proportional to the relative noise ξ. This is verified for experimental data (different individual molecules) shown in the left graph. The effect of the integral boundaries (ΔL=2L in units of σ) on the error is shown in the graph to the right. The values in units of nm correspond to the errors for the specific examples using $\sigma \approx$ 300 nm.

In the graphs of fig.31 the error is given as a fraction of the signal width σ, which is approximately 300 nm for the used optical microscopes (λ=633 nm). The relative noise ξ is estimated from the SNR of the raw data. The integral boundaries (2L) in the right graph of figure 30 are also given in units of σ. In practical terms, the smallest SNR needed to obtain a position with 30 nm accuracy is 7 (ξ = 0.143), and the region of interest used to do the fitting should ideally have a width > 3σ or approximately 900 nm (e.g. on an image with 168 nm per pixel that gives 6 pixels). Depending on the measurement technique and integration times, it is possible to obtain a SNR as good as 100, reaching a positioning accuracy below 1 nm. Note that, strictly, this is only valid for point-like objects. Nanobeads or labelled vesicles in a cell, for example, which have a diameter of 30 nm and above cannot be taken as point-like emitters. As a consequence their RF is not accurately described by a Gaussian. The positioning accuracy according to the considerations made so far are not strictly valid for these objects.

A comparison between the positioning accuracy (the errors) obtained via fitting for an immobile molecule should coincide with the '1σ' confidence width, or standard deviation of the positions themselves. This can be verified experimentally (cf. fig 32).

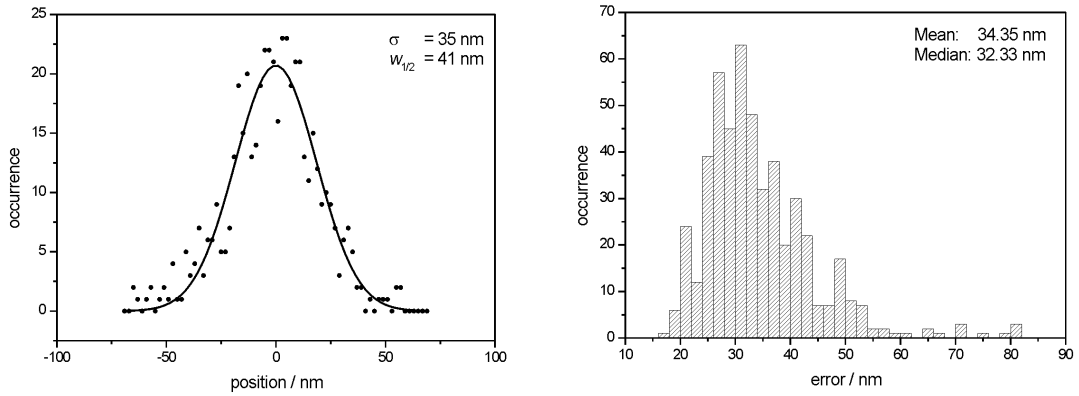

Figure 32: The positions of an immobile molecule are determined over a sequence of 500 frames with the automated tracking programme. a) The found positions are distributed around a mean value with a standard deviation of 35 nm. b) The distribution of errors is shown as a histogram, the mean error is 34.5 nm.

Graph a) in figure 31 shows the histogram over the positions centered at origin. The positions are distributed around that value with a standard deviation of 35 nm. The histogram over the errors is shown in figure 32b. The errors must not be normally distributed as they depend on different parameters than the position itself (e.g. the noise, which may vary significantly from frame to frame). The average error is 34.4 nm and stands in good agreement with the standard deviation of the position distribution, which is 35 nm.

3.2.1.2. Trajectory Analysis

The data array obtained with the tracking software is analysed with a separate programme. In this programme the individual positions found for one pattern in a given frame can be displayed as trajectories and analysed to obtain several diffusion parameters. In the following the whole evaluation procedure is described in detail using an exemplary trajectory of a molecule diffusing in a porous material. In this example it will become apparent that the molecule is undergoing normal isotropic diffusion in two dimensions.

Trajectory: The trajectory of the exemplary molecule can be displayed as a sequence of coordinates with the respective positioning errors (figure 33).

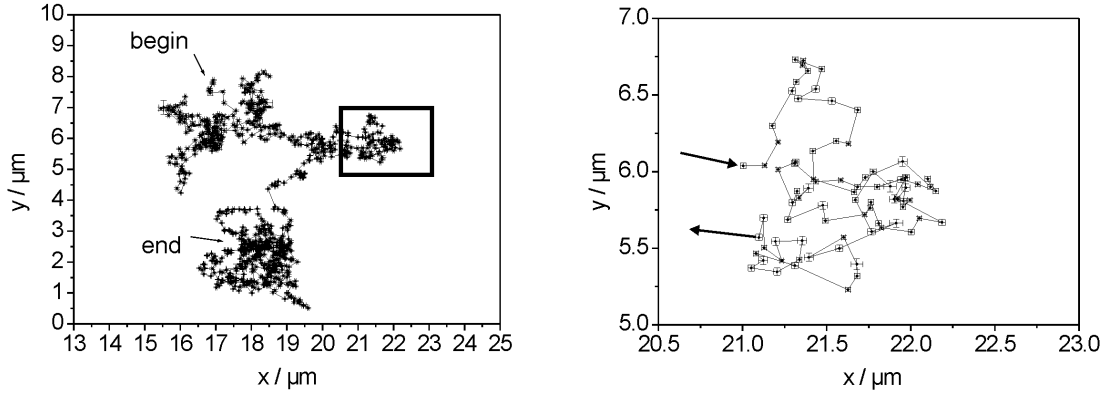

Figure 33: The trajectory of an individual molecule is represented as a sequence of coordinates connected by broken lines (here δt = 100 ms). The right graph shows a zoomed-in view of the trajectory to emphasize the size of the individual errors (≈ 30 nm) in comparison to the whole trajectory.

The trajectory itself may already point towards some spatial anomaly in the diffusional behaviour, for example a region in which the molecule becomes trapped, or a region in which the diffusion shows a preferential direction. Such a recognition 'by eye' is only possible if the part of the trajectory containing the anomaly is particularly pronounced. The features in the exemplary trajectory shown in figure 33 might suggest that there are

regions in which the molecule becomes trapped or confined. On the other hand, it is known from simulations of random walks that such areas in which the particle seems to be confined are normal. [Berg86] For this reason the analysis of diffusion cannot rely on the observation of pronounced features in the trajectory. Instead, diffusion is more properly characterized by inferring other parameters such as the behavior of the mean square displacement (MSD) versus time, by analysing the step length distributions or the angles between consecutive steps.

Step length distribution: The length of each step (and for every time lag) is obtained by analysing the coordinates separated by 1,2,3 etc. frames. The respective time lags, in turn, are obtained by using $t = n \cdot \delta t$, where n is the number of steps between two coordinates and δt the time corresponding to the frame-rate of the acquired sequence of images.

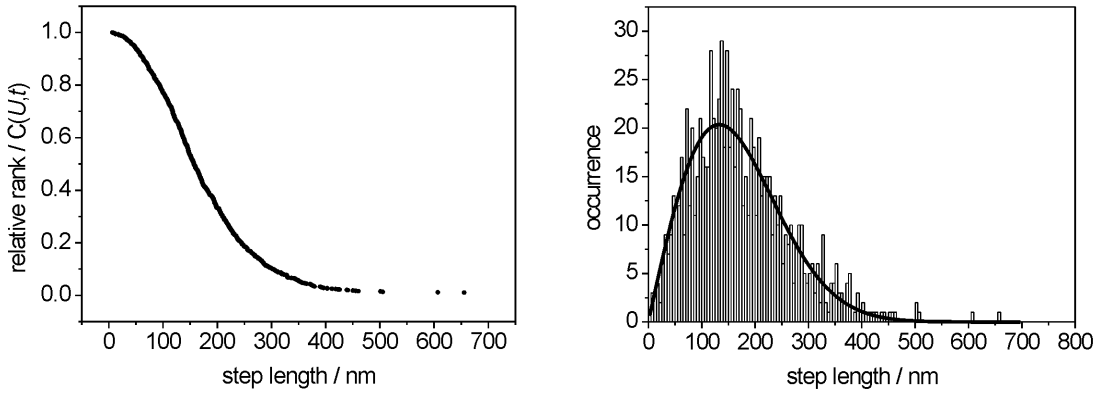

Figure 34: The ranked step length (for n=1) of the trajectory (left) can be analysed to yield the histogramme (right graph). The straight line in the right graph is not obtained by fitting the histogramme directly. Note that the parameters to generate the (smooth) distribution curve are obtained from the fit to the ranked data on the left graph.

The statistical analysis, as described in section 2.3.2., examines the step length distribution. In contrast to the analysis of a simple average over the individual displacements, the information contained in the individual steps is not lost due to averaging. In this way it is possible to check for a deviation from the distributions expected for a single population undergoing normal diffusion. The analysis program

therefore computes all step lengths between 2, 3 and more consecutive frames and assigns them a relative rank j/N (cf. section 2.3.2; left graph in figure 34). The conventional histograms (using an arbitrary binning parameter) are also computed in order to illustrate the population distribution in a more intuitive way (right histogram in figure 34). The curve enveloping the histogram (right graph in figure 34) is obtained by fitting the ranked step-lengths according to $C(R,t)$ (see section 2.3.2.):

$$C(R,t) = 1 - P(R,t) = \sum_{i=1}^{m} A_i \exp\left(\frac{-R^2}{\left\langle r_i^2(t)\right\rangle}\right). \qquad (18b)$$

and using the obtained $\langle r_i^2(t)\rangle$ in the equation for the step-length distribution:

$$q(r,t) = \sum_{i=1}^{m} \frac{A_i 2r}{\left\langle r_i^2(t)\right\rangle} \exp(-r^2/\langle r_i^2(t)\rangle). \qquad (16b)$$

Note that the graphs in figure 28 use $m = 1$, because the use of a further population is not justified by the data. Note also $A_1=1$ since the sum over all A_i is 1

Squared steps and the MSDs: The squared displacements are obtained simply by squaring the step-lengths. As pointed oput in section 2.3.2. the time dependence of the mean squared displacement can be used to characterize diffusion, and the mean squared displacement, in turn, can be obtained via population analysis from the ranked data, according to equation 14 (section 2.3.2.):

$$C(U,t) = 1 - P(U,t) = \sum_{i=1}^{m} A_i \exp\left(\frac{-U}{\left\langle r_i^2(t)\right\rangle}\right) \qquad (13b)$$

The analysis program computes the squared step lengths for different time intervals and assigns each squared step a relative rank j/N. The ranked squared displacements for the exemplary trajectory are shown in figure 34 (left). The population analysis according to

$C(U,t)$ using m=1 gives the respective value for $\langle r^2(t)\rangle$ (MSD) in dependence of the time lag t. (note that here m = 1). The MSDs obtained in this way are plotted versus time in the right graph of figure 35. The resulting MSD versus time plot can be analysed via linear regression. For this trajectory a diffusion coefficient of $D = (1.02 \pm 0.02)\ 10^{-9}\ cm^2s^{-1}$ is obtained, assuming an isotropic random walk in two dimensions.

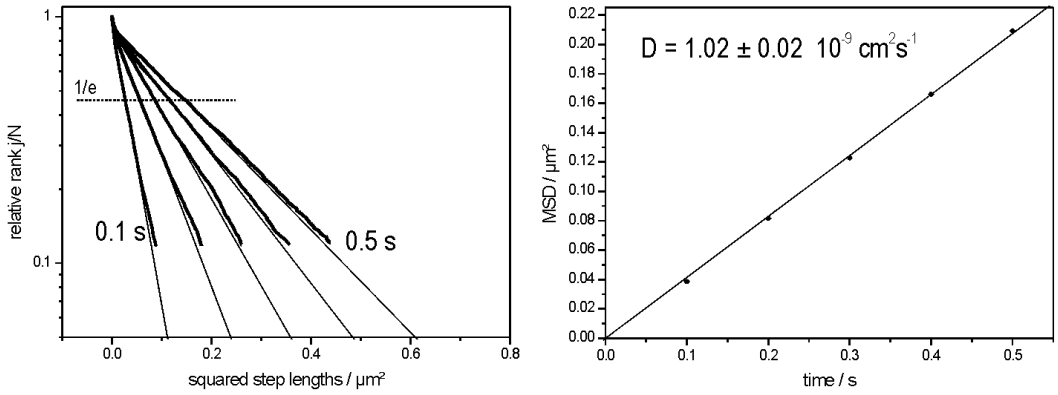

Figure 35: Analysis of squared steps. a) Population analysis with ranked MSD for five time intervals (0.1 - 0.5). b) The obtained values for $\langle r^2(t)\rangle$ are plotted versus time.

This type of analysis can be carried out for all steps in all trajectories. The simpler analysis via averaging of the squared step lengths gives the same diffusion coefficient if the population is homogenous, and can be carried out for molecules which do not show diffusional anomalies. As pointed out in section 2.3.2 the advantage of the evaluation using the ranks is that it is very sensitive towards the presence of diffusional sub-populations. Different populations can be separated without the necessity of introducing an arbitrary cut in the analysed trajectory. (A clear example demonstrating this is given in section 4.5.)

Angles between steps: Another important parameter in the analysis of diffusion is the angle between consecutive steps. It is the only parameter pointing to the orientational differences in a trajectory. It is defined as 0° for two consecutive forward steps and ±180° for a forward step followed by a backward step. Negative angles are defined as steps in a

counter-clockwise direction, whereas positive angles denote steps in a clockwise direction. The angles between steps are calculated by the programme with assigned ranks and in the form of a histogramme (left graph in figure 36).

Another useful way to check for angular anomalities (e.g. due to an influence of structures on the motion of the molecules) is given by the analysis of a so-called common origin plot. Here all steps start from the origin. If the resulting plot deviates from a perfect circle then some deviation from normal isotropic behavior is present (right graph in figure 35).

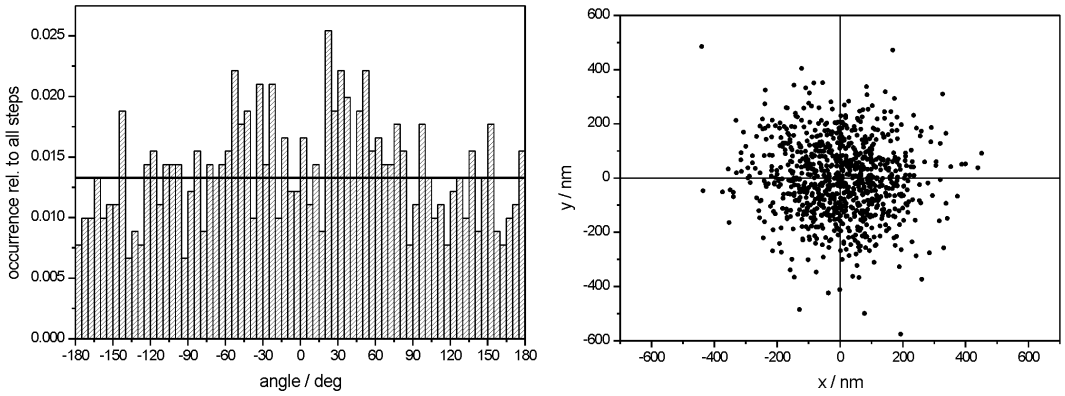

Figure 36: Left is the histogramme over all angles in relation to the total number of steps. The right graph shows the common origin plot.

The evaluation of angles is of particular interest for trajectories with structural features (as have been observed in the case of molecules diffusing in unidimensional tortuous channels - cf. section 4.6.), and need to be analysed thoroughly. If all angles have an equal probability of occurring the expected equal distribution occurs at the reciprocal value of the number of bins (in this case at 5° per bin the value is 1/72). The slight overrepresentation of forward steps in this exemplary trajectory is not significant. There is room for improvement in the evaluation of step angles, the analysis of the temporal evolution of the angle as the molecule diffuses along its trajectory could lead to a parameter comparable to a trajectory persistence length. Structured trajectories are more appropriately described by the unidimensional diffusion model, however, the uni-

dimensional track along which the molecule diffuses has to be corrected for its tortuosity. The angles between the steps could be used to do this correction.

Global analysis: Finally, the programme also returns a global picture of the diffusion in a particular movie, by including all trajectories that have been tracked in a film in a common plot. This type of data allows to determine the presence of spatial heterogeneities in the sample, or heterogeneities in the diffusional behaviour on going from one molecule to another. In the chosen example, except for two molecules that appear to be significantly less mobile than the remaining molecules, no significant heterogeneity is observed (cf. fig.37). The global MSD versus time plot for the diffusing molecules (right graph in fig.37) confirms that the diffusional behaviour of the individual molecules is narrowly distributed around a mean value. The diffusion coefficients for these trajectories lie between 0.8 and 1.5 10^{-9} cm^2s^{-1}.

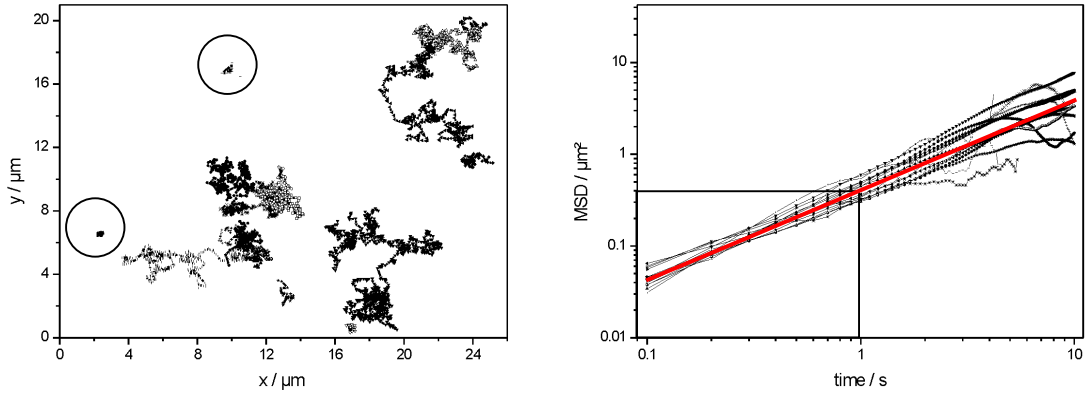

Figure 37: The global analysis of all trajectories in a film can be visualized in the form of a trajectory 'map' (left) and in the form of a MSD versus time plot (right) for all trajectories. In this example the diffusion appears narrowly distributed around a mean value for $D = 1 \cdot 10^{-9}$ cm^2s^{-1} (red curve, with $\langle r^2(t) \rangle = 4D \cdot t$ and 0.4 $\mu m^2 = 4 \cdot D \cdot 1$ s).

3.2.2. Evaluation of Single Molecule Spectra

Spectra of individual molecules can be obtained with the Prism/CCD setup described above. As mentioned there, the individual spectra must be corrected to account for the non-linear dispersion curve of the prism and the wavelength dependence of the elements in the detection. In effect the correction does not change the overall shape of the spectrum much (see fig 38 on going from top to bottom). Such a correction, however, is essential to obtain an appropriate fit.

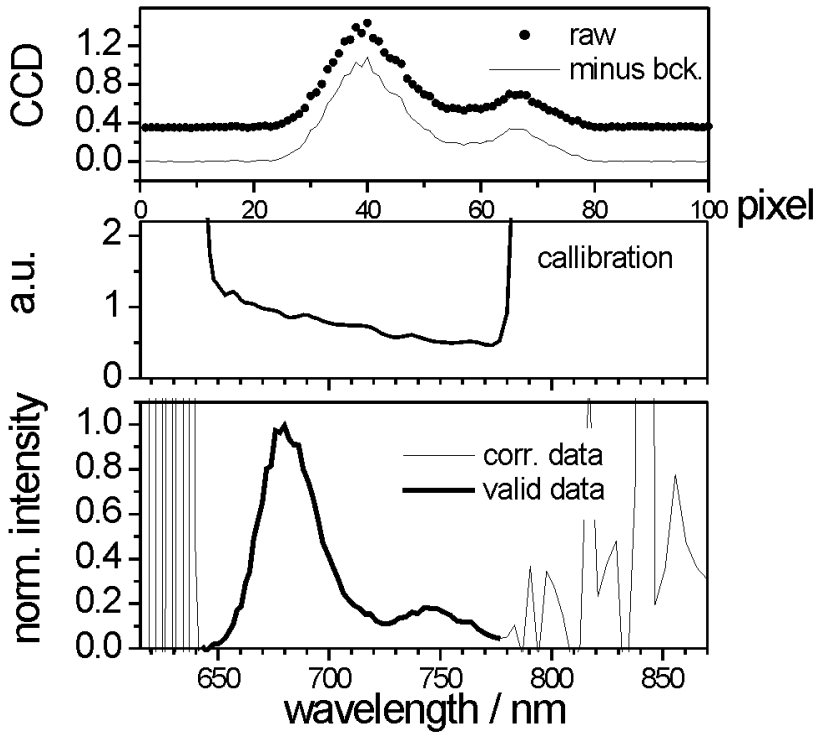

Figure 38: Experimentally obtained spectra have to be corrected. First the background is subtracted, then the data is callibrated to account for the non-linear dispersion curve of the prism and the wavelength dependence of the elements in detection. (adapted from [Seebacher02])

In general, the room temperature fluorescence spectrum of an individual molecule resembles the static ensemble spectrum and consists of a main emmission band

accompanied by more- or less-well resolved vibronic bands. The presence of these bands and how well-resolved they appear in the spectrum depends on the used molecule itself and on its immediate surroundings. A typical emmission spectrum can be characterized by the energetic position of the bands (main and vibronic if possible) their intensities and respective widths. To find these parameters the spectra can be modelled by gaussian shaped curves, which can be used to fit the experimental data. In fig. 39 two examplary spectra of different dye molecules, Cy-5 in MCM-41 and TDI in PMMA are shown, to illustrate that different shaped spectra may require different fitting models.

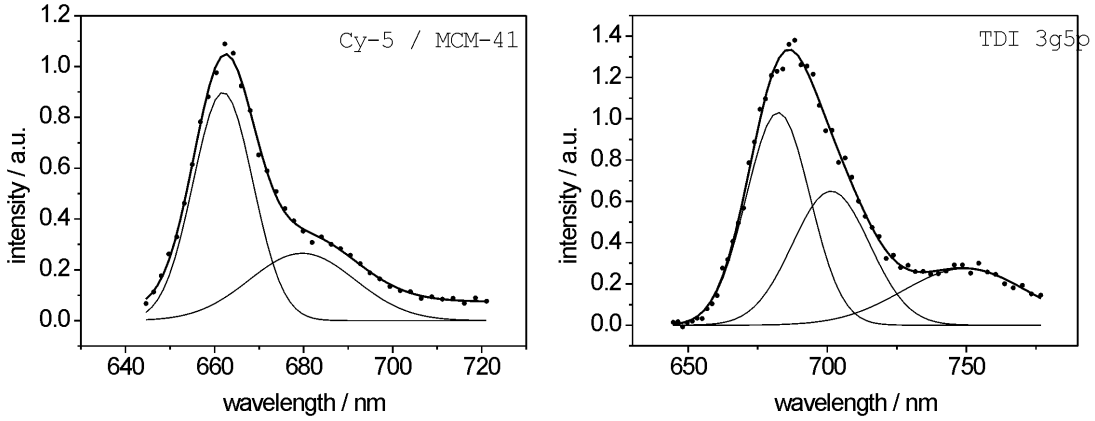

Figure 39: Two exemplary spectra of single molecules at room temperature. (a) The spectrum of Cy-5 in MCM-41 can be described by a model consisting of two Gaussians. (b) The spectrum of TDI in PMMA is described by a model consisting of three Gaussians.

The analysis programme obtains several parameters of the spectra, like the position of the emmission maximum, location of the vibronic shoulder or overall width of the spectrum by fitting the experimental data to the respective multi-gaussian function. A sequence of *n* spectra can be analysed by the programme automatically. As a result one obtains an array containing the respective number of the spectrum (corresponding to the time-axis as the acquisition time is known), the fit parameters and the respective errors. The output can then be analysed statistically, in terms of populations and spectral dynamical behaviour in a further step.

3.2.3. Evaluation of Orientation Measurements

The orientation of fluorescent dye molecules can be determined by polarization dependent measurements, because the transition dipole moment of dyes is a vector: Light with polarization parallel to the transition dipole moment will excite the dye molecules with a high probability, whereas light with a polarization perpendicular to the transition dipole moment will have a negligible probability of exciting the dye (see fig. 40).

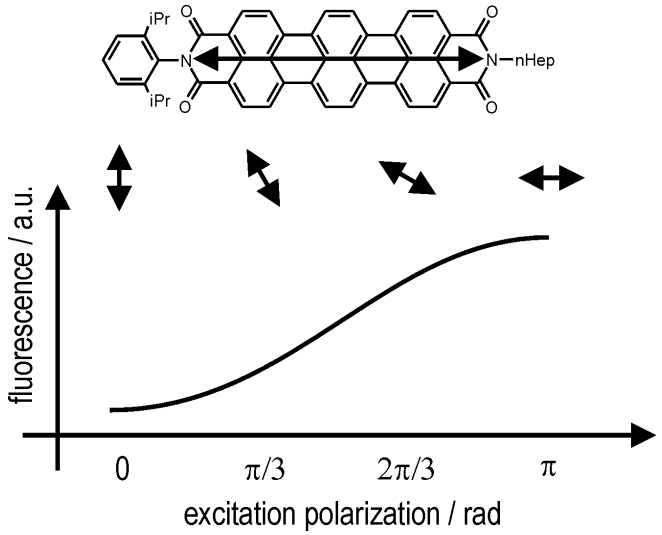

Figure 40: The fluorescence intensity of a dye molecule depends on the orientation of the molecule's transition dipole moment and the relative orientation of the polarization plane of the excitation light.

To determine the orientation of fluorescent dyes (on ensemble or SMS levels) the fluorescence intensity is recorded in dependence of the polarization of the excitation light. A rotating λ/2 plate in front of the objective barrel modulates the polarization plane continuously (fig.41). The polarization plane is monitored in transmission with a detector after a polarizing filter, with a known orientation (see figure 41). The polarization dependent data obtained with the setup described above consists of two curves (a) the modulated transmission signal (A) and (b) the modulated fluorescence signal (B) of a particle, or molecule.

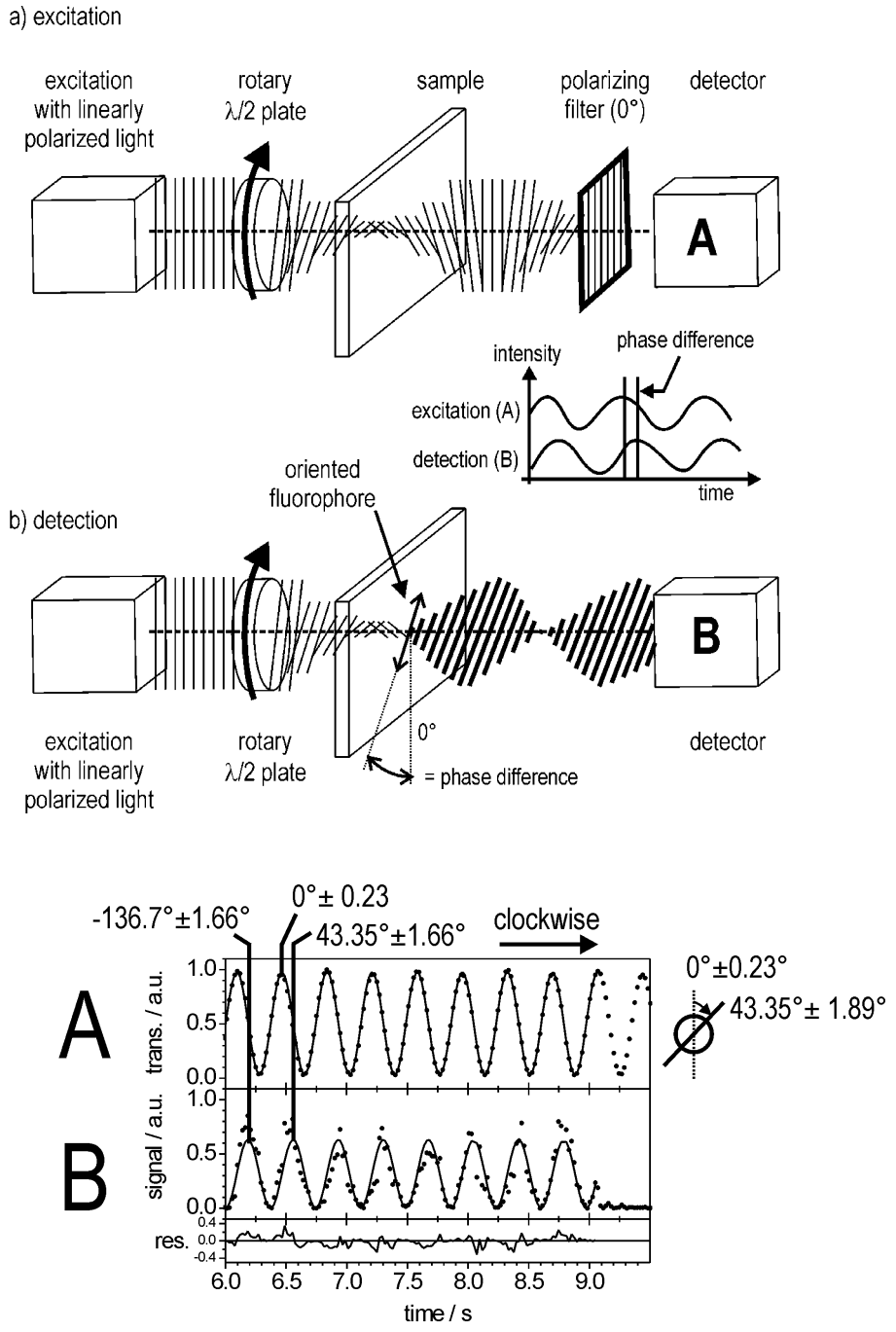

Figure 41: Schematics of polarization dependent measurements. a) Excitation with modulated polarization. b) Detection of modulated emission. c) Experimental data for an individual molecule. The phase difference ϕ of the curves is obtained by fitting the data to a cosine-square function (eq. 34). Note also the abrupt end of the fluorescence intensity trace at ca. 9.1 s, which is typical for individual fluorophores.

The evaluation program first analyses the transmission curve (upper graph in fig.41c) to obtain a good estimate for the frequency and phase of the modulated transmission curve. The data then fitted to a set of cosine-square equations (eq. 34), in order to obtain the phases of the modulated curves:

$$\begin{cases} I_T(t) = A_T \cos^2(\omega t + \phi_T) \\ I_F(t) = A_F \cos^2(\omega t + \phi_F) \end{cases} \tag{34}$$

Both equations describe the transmission and fluorescence intensity curves as a function of time *t* and are labelled with the indices 'T' and 'F'. Note that both equations share the same frequency parameter ω and are **not** independent. The amplitudes A_T and A_F may vary from curve to curve. The main parameter for the evaluation of the orientation are the phases ϕ_T and ϕ_F of the transmission and fluorescence signals with respect to the rotation of the λ/2 retardation plate. The difference between the phases gives directly the orientation angle of the fluorophore in the focal plane of the microscope and in relation to the setting of the transmission polarizer.

The data can be divided into *n* smaller segments, typically containing two oscillation periods, with a length (τ). The fitting procedure can be applied to all *n* segments and the phase differences, or the in-plane orientation angle of the transition dipole of the emitter $\Delta\phi = \phi_T - \phi_F$ can be obtained as a function of time $\Delta\phi(t)$ where $t = n\tau$. In that way it is possible to monitor changes in the orientation of the emitter, for example if a molecule turns around. The temporal resolution with which the phase-difference is determined can be increased by reducing the segment legth τ, however segments with a length smaller than one oscillation period do not yield values with a satisfactory error. Conversely, longer segment lengths improve the accuracy with which the angle can be determined, but worsen the temporal resolution.

The orientation of an individual fluorophore is an important parameter that can be used to (a) determine the alignment of pores and (b) to decide if translationally immobile molecules are otherwise free to turn (e.g. in a sizeable confinement).

3.2.4. Photostability of Fluorescent Dye Molecules

Fluorescent dye molecules that are used in microscopy and, particularly, in SMS studies have to be clearly distinguishable from the remaining signals coming from the sample. In other words, suitable molecules have to deliver a good signal-to-noise ratio steadily. Fluorescent dye molecules, however, have a limited duty-life.

The intensity with which one molecule fluoresces can be recorded as a function of time. After a certain time, the molecule loses its capability to fluoresce abruptly - it has photobleached (fig.42). This event, that marks the last step in the duty-life of a fluorescent molecule is also a key feature of an indivudual, isolated emitter and is often used to prove that an individual fluorophore was observed.

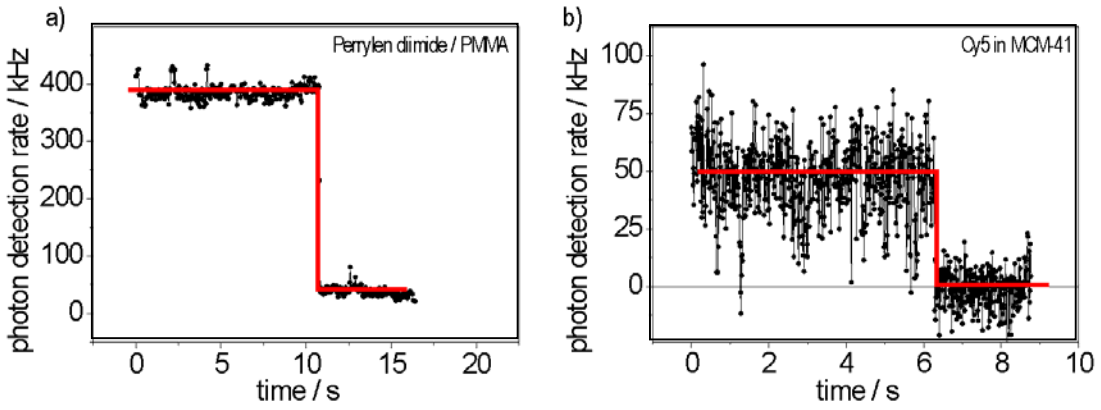

Figure 42: Two typical single molecule fluorescence intensity transients. The trace for a perrylendiimide derivative in PMMA (a) and for Cy-5 covalently bound to the pores of a molecular sieve(b) can be compared directly, showing (a) is the superior dye / matrix system.

Clearly, a good fluorescent dye molecule fluoresces strongly and is particularly photostable (compare fig.42 a and b). The essential idea behind the characterization of a fluorescent molecule, in this sense, is to find a parameter that describes its photostability and allows a comparison with other fluorescent species.

Theoretical background: The photobleaching process can be formulated, in a very simplified way, as a chemical reaction:

$$A + h\nu \leftrightarrows A^* \longrightarrow B$$

In this description the molecule A in the ground state is excited by a photon and reaches an excited state A^*, from where the molecule either relaxes back to A (via fluorescence or non-radiative relaxation processes) or undergoes some irreversible reaction to species B. If species B is not fluorescing the molecule has 'photobleached'. Note that the reaction leading to B can be arbitrarily complex, e.g.:(a) reaction via triplet state, (b) reaction from higher excited states or dark-states (c) reaction via the formation of radicals, (d) reactions with solvent.

Assuming a quasi-continuous irradiance, the probablility of an excited fluorophore of being fluorescent after time t, is (according to [Eggeling05]):

$$p(t) = k_z \cdot \exp(-k_z t) \qquad (35)$$

Despite the various reaction pathways leading to B the photobleaching reaction for isolated molecules can be considered to be of pseudo-first order, with an effective constant k_z comprising all microscopic rate constants. Instead of time t, it is often more convenient to use a number of survived photocycles n, which - within limits - is independent from the irradiation wavelength and intensity.

$$p(n) = k_n \exp(-k_n n) \qquad (36)$$

With $k_n = \langle n \rangle^{-1}$ and $\langle n \rangle$ being something like a characteristic number of survived photocycles (strictly speaking, this number is only valid for molecules kept under identical conditions). Note that $\langle n \rangle$ is not a *mean* value. The total number of cycles $\langle n \rangle$ is connected to the number of emissive cycles $\langle n_{FL} \rangle$ via the fluorescence quantum yield: $\langle n \rangle \phi = \langle n_{FL} \rangle$. The number of *detected* photons $\langle n_{DET} \rangle$ is the actually measured quantity.

$\langle n_{DET} \rangle$ relates to $\langle n_{FL} \rangle$ via the detection efficiency of the setup (3% in the case of the LSM410). To keep this part general, however, $\langle n_{FL} \rangle$ will be used in the following. Equation 36 can be written down as follows:

$$p(n_{FL}) = \langle n_{FL} \rangle^{-1} \exp\left(-n_{FL} / \langle n_{FL} \rangle\right) \qquad (37)$$

$\langle n_{FL} \rangle$ is the characteristic number of emitted photons prior to photobleaching. It determines the number of emitted photons when the probability to survive the next cycle and emit a photon reaches 1/e (≈ 0.368). In an ensemble of identical molecules 63 out of 100 will already have bleached. $\langle n_{FL} \rangle$ depends on the chemical structure of the dye itself and the matrix in which it is situated. It is sensible to assume that the characteristic number of photons is a narrowly distributed property for a dye in a homogenous sample.

It is possible to obtain the number of emitted photons prior to photobleaching, n_{FL}, from an intensity transient of a molecule that photobleached. It corresponds to the area under the typical step curve. This area and other parameters used in the following discussion are depicted schematically in figure 43:

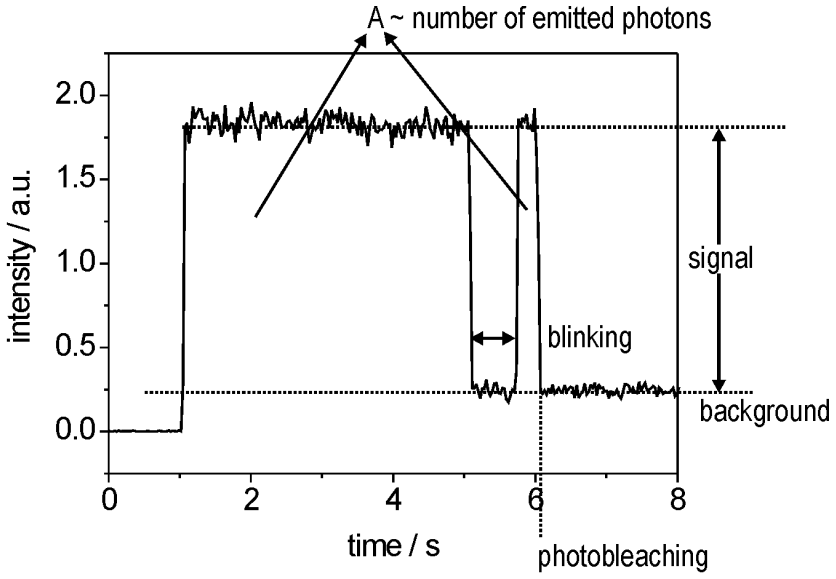

Figure 43: A typical intensity transient as obtained by the microscopy apparatus, with typical parameters.

The histogram of the experimentally obtaind n_{FL} should correspond to an exponential decay as in equation (37). However, often it is not possible to exclude the presence of different sub populations of molecules behaving distinctly - for example molecules close to a surface of the matrix, molecules in apolar regions of a polymer, or in water pockets.

An convenient possibility to obtain the various $\langle n_{FL} \rangle$ of distingishable sub-populations is given by a statistical population analysis (similar as seen for the evaluation of diffusion in the previous chapter). The cumulative probability $P(N)$, or the probability that a molecule emits between 0 and N photons is thus:

$$P(N) = \int_0^N p(n)\, dn = 1\text{-}\exp\left(-N / \langle n_{FL} \rangle\right) \qquad (38)$$

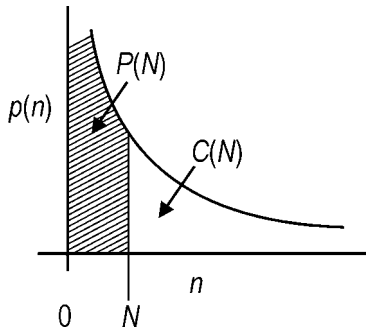

and the complementary function $C(N)$ is:

$$C(N) = 1 - P(N) = \exp\left(-N / \langle n_{FL} \rangle\right) \qquad (39)$$

Assuming different populations of isolated molecules with different bleaching probabilities $C(N)$ turns into a sum:

$$C(N) = \sum_{i=1}^{m} A_i \exp\left(-N / \langle n_{i,FL} \rangle\right) \qquad (40)$$

With $\Sigma A_i = 1$ and A_i being amplitude for each individual population. As shown for the discussion concerning diffusional data the relative ranks j/N of the individual data correspond to $C(N)$.

Experimental evaluation of photostability: The evaluation of photostability consists in acquiring bleaching curves for a number of individual molecules (ca. 100) and then analysing the results statistically. A typical photobleching curve, or intensity transient, for a single molecule is described by a constant signal which ends abruptly, and which may or not contain intermittencies (described by on- and off-times, cf. figure 43).

The intensity transient is acquired in the form of an intensity versus time. The intensity is given as a rate (number of detected photons per time) which is obtained from a callibration curve (that has to be obtained for every set of measurements). The signal of a molecule is given in relation to the background signal, which is set to zero in the analysis. This background signal is unspecific and may vary from molecule to molecule (see fig.43). It is determined for every recorded intensity transient from the last values of the intensity transient - this number (ca. 100) can be modified, but it is important to record sufficient background signal to obtain a reliable value. The time scale is adjusted so that the beginning of the irradiation is set to $t = 0$ - The beginning of the irradiation is marked by unblocking the excitation beam (cf. the first on-jump at ca. 1 s in fig. 43) With the callibrated curve, it is possible to find the on and the off-times as well as the total number of emitted photons before photobleaching. These characteristic times are found by scanning the intensity trace point by point and finding the positions of all abrupt jumps that exceed an adjustable threshold value (typically, the half-signal). The integral is obtained numerically.

The program is written so that the intensity transients for many molecules, in the form of a sequence of files, can be evaluated automatically. All parameters (number of emitted photons, photobleaching times, on and off-times) are returned in a separate file. With sufficient traces for individual molecules (usually between 50 and 100) it is possible to evaluate the parameters, like the number of emitted photons, on- and off-times statistically. In this group such an evaluation is carried out for all dye molecules used in SMS studies. Two specific examples for such a characterization will be described in the next chapter.

4. Results and Discussion

This chapter presents the results of the investigations on host-guest materials using the techniques and methods described in chapters 2 and 3. It is subdivided in eight sections.

The first section addresses the more general and straightforward measurements performed on the level of molecule ensembles. These measurements provide important details on the samples, for example if they are of appropriate optical quality for the more complex studies involving single-molecule spectroscopy (SMS). The second section introduces SMS methods, and describes a study on the photostability of two new dyes in comparison to commercially availiable and commonly used fluorophores. The SMS measurements on the diffrent host-guest materials are presented in the last six sections. Section 4.3. describes the investigations of the orientational distribution of differently sized dyes in a zeolite. Sections 4.4, 4.5, and 4.6 present diffusion studies based on single-particle tracking in various materials. Section 4.7 shows a study on the spectral diffusion of a dye in a polymer matrix. Section 4.8. covers the investigations made on a porous material with fluorophores covalently attached to the inner surface of the material.

4.1. Characterization of Host-Guest Materials / Ensemble Measurements

The subject of the majority of the investigations carried out at single-molecule level described in this thesis were host-guest materials consisting of organic dye molecules loaded into (or covalently bound to the inner surface of) the channels and cavities of micro- and mesoporous molecular sieves. Before going to the experimentally more sophisticated SMS studies, the materials are often investigated using 'bulk' measurements (i.e. ensemble measurements). These experiments define whether the sample is suitable for further, more detailed, studies based on single-molecule spectroscopy, or if there are more fundamental problems with the samples that need to be addressed first. For example: (a) Are the individual crystals or particles big enough to allow for optical microscopy? Suitable particles have to be in the order of a few microns in width, length and depth to ensure that the optical measurements are taking place within the porous host material. (b) Are the samples free of defects and cracks? If not, to what extent are defects present in the sample? (c) Is the loading of the dye in the material homogenous, or does it show specific heterogeneities? (d) Do the samples become degraded, for example, during treatment with solvents or while the particles are embedded in polymers? Ideally, host-guest materials should not become dissolved or lose guests.

In a conventional approach, host-guest samples based on mesoporous materials are often characterized by electron microscopy, X-Ray diffraction techniques, and adsorption isotherms. The use of optical microscopy techniques is less common. However, it provides important complementary information which is not readily available from other methods: (a) The main advantage of optical microscopy is the possibility to gather spatially resolved information (static and dynamic) from the interior of a sample. It is possible, for example, to locate sub-structures in the inner volume of an otherwise well-behaved crystal (i.e. the habitus, and X-ray diffraction patterns point to near-perfect structures). (b) Optical microscopy is a non-destructive method and does not require specific sample preparation procedures such as gold-sputtering or thinning, for example as required for electron microscopy techniques.

4.1.1. Defects

Crystals often form defect structures which may vary in size and shape, going from single defects in the crystal lattice (on the atomic or molecular scale), to boundaries between twin crystals or cracks (which have sizes comparable to that of the crystal or particle). It is of some importance to know if and to what extent defects are present in the samples studied. Sample surfaces can easily be studied in high resolution using electron microscopy techniques, as shown in figure 44 exemplarily for an $AlPO_4$-5 sample.

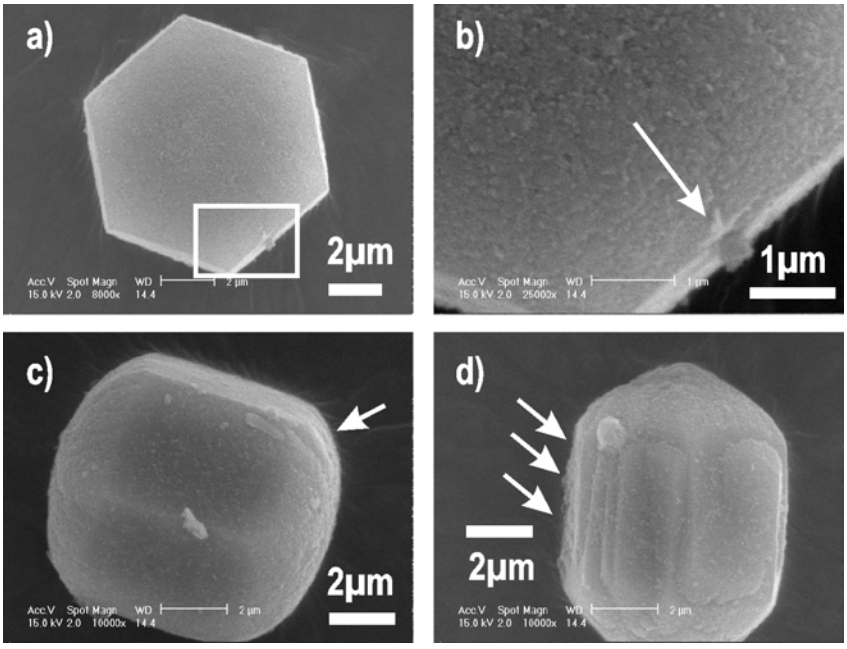

Figure 44: Scanning electron micrographs of Au-coated $AlPO_4$-5 crystals (containing Oxazine-1). The scale bar indicates 2µm. [Micrographs taken with Ken Yasuda in the group of Prof. Dr. Bein]

The scanning electron micrographs in figure 44 reveal defect structures on the surface of the $AlPO_4$-5 crstal (as indicated by the arrows) with a size well below 100 nm. Defect structures of this size are not resolved by optical microscopy methods. While electron microscopy techniques produce images of surfaces with a spatial resolution in the order of a few nanometers, it is, however, limited to the surface of the investigated samples. In

the best case, using transmission electron microscopy (TEM) it is possible to detect structures in the volume of a very thin sample (usually with less than 50 nm thickness). Structures in the volume of larger materials are not detectable using electron microscopy techniques. Another limitation of high resolution electron microscopy methods is that the specimens often have to be prepared in some way, e.g. metal coating, thinning, freeze-fracturing, etc. For this reason it is not possible to exclude the possibility that defects originate during the sample preparation procedure.

Optical microscopy, while operating with a comparatively lower spatial resolution (of a few hundred nanometers), has access to the inner volume of a (transparent) sample, and may resolve structures, for example in the inner part of a crystal, that are not accessible to electron microscopy. The difference between a scanning electron microscope and an optical microscope is shown schematically in figure 45.

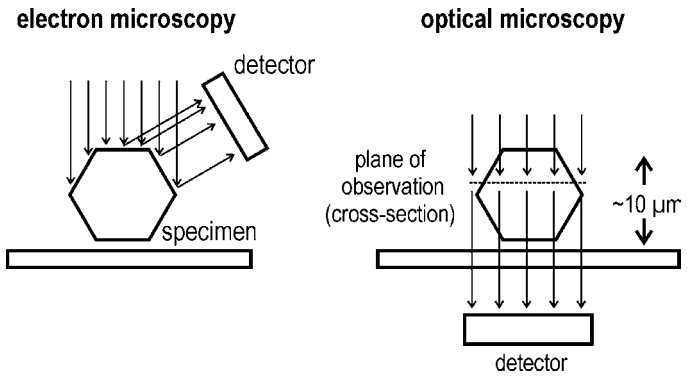

Figure 45: The difference between electron microscopy and optical microscopy. In electron microscopy the acquired images are restricted to the surface of an object (or to a very thin layer of ≈ 50 nm in the case of TEM - not depicted here). In optical microscopy it is possible to obtain information from the volume of a transparent sample.

Typical optical micrographs showing a cross-section through the interior of a micrometer sized $AlPO_4$-5 sample are depicted in figure 46. In these images the samples consist of $AlPO_4$-5 crystals containing different fluorescent dye molecules. It is possible to observe different structural features in the inner part of the crystals.

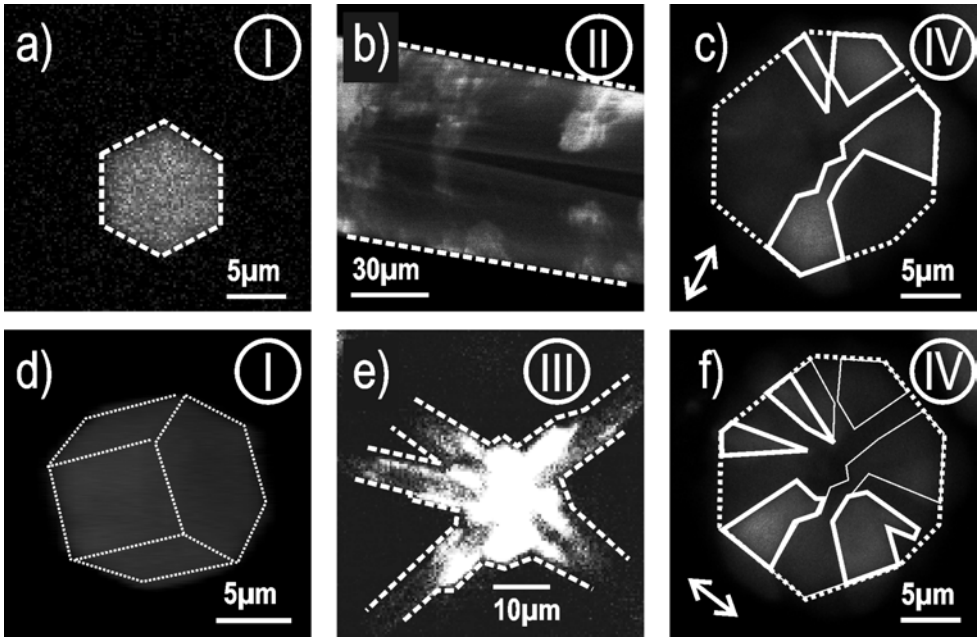

Figure 46: Structural features situated in the inner part of $AlPO_4$-5 can be visualized via fluorescence microscopy. a) and d) show homogenously loaded crystals (d is a 3D reconstruction based on individual cross-sections). b) shows a cross section through a very large crystal with heterogenous loading of dye. e) shows a twinned crystal with a pronounced irregular structure. c) and f) show polarization dependent images (the polarization is indicated by the arrows), indicating that the dyes are arranged with a preferential orientation in the indicated domains.

In case I, (figure 46a and 46d) the fluorescence images show a homogenous loading of dyes (Oxazine-1) in $AlPO_4$-5 (dyes incorporated during synthesis). Figure 46d is a 3D reconstruction based on individual optical cross sections. Samples in such quality represent the ideal case. In case II (figure 46b) very large crystals (> 100 µm) have been synthesized containing a DCM dye which was incorporated during synthesis. X-Ray diffractometry and the habitus of the crystal point to nearly ideal structures. The fluorescence images, however, reveal that the material is organized in domains into which DCM is incorporated more or less effectively during the formation of the material. The central region of the crystal is not hollow, but does not contain dye molecules, denoting that this region is somehow sealed off during the formation of the solid body of

the crystal. The peripherial region of the $AlPO_4$-5 crystal shows a heterogenous distribution of dyes [Weiss03] Case III (figure 46e) shows the 'worst' case, in which the crystals form an irregular structure. Case IV (figures 46c and 46f) shows polarization dependent images (the polarization plane is indicated by arrows) of an optical cross section through a large $AlPO_4$-5 crystal containing oxazine-1. The dye is incorporated with different preferential orientations in irregular domains, possibly reflecting the direction of the unidimensional pores.

With confocal microscopy it is not only possible to visualize and to characterize quality and homogeneity of crystal samples but also to detect defects and boudary structures that give insight into the crystallization mechanism of the host. Such data is of valuable help for the collaborating groups working on the synthesis of these materials.[Weiss03]

4.1.2. Staining of Structures in a Host-Guest Material, Dye Uptake

One of the main features of porous materials is that their interior is accessible to molecules coming from the outside. The dye uptake, however, depends on a series of parameters like the size and the polarity of the molecules and of the pore. Furthermore, the presence of other co-adsorbed species (like template molecules and structure directing agents used during the synthesis of the material) might also hinder an efficient inclusion of dye molecules. On the other hand, the removal of these co-adsorbed species, by applying vacuum or by calcining the template (i.e. heating the sample to ca. 600 °C), might induce the formation of defects or cracks in the sample.

The dye uptake of a microporous material from the outside (in contrast to encapsulation of dyes during sythesis) is another important observation, that points to the accessibility of the pores. There are basically two experiments involving dye-uptake that can be performed: (a) Experiments on the basis of the macroscopic diffusion model (cf. section 2.3.1) in which a dye gradient diffuses into a porous host. These experiments (i.e. by analysing the temporal evolution of the dye concentration) allow to obtain a first estimate

of the diffusion coefficient for a molecule moving inside the porous material. (b) Size-exclusion experiments that allow to characterize the presence of differently sized pores or cracks. This is done by varying the size of the dye molecule. For example, materials with a defined pore size (such as AFI or MFI) will not be accessible to molecules that are significnatly larger than the pore size. If such a molecule penetrates into the material, this can only occur via irregular pores, cracks and defects.[Seebacher01]

One important dye molecule used in dye-uptake experiments is the so-called stilbene derivative - 4-(4-dimethylaminostyryl)-N-methyl-pyridinium iodide (Sigma D-3418, the structure is depicted in fig. 47). This dye molecule has an increased fluorescence quantum yield of about 0.35 when it is adsorbed to a surface (as opposed to a fluorescence quantum yield of about 0.1 in solution). This increased fluorescence quantum yield is likely due to a reduction of the molecular flexibility, leading to the elimination of non-radiative relaxation channels.[Seebacher02d] The resulting difference in the molecular brightness can be used to generate contrast in fluorescence microscopy.

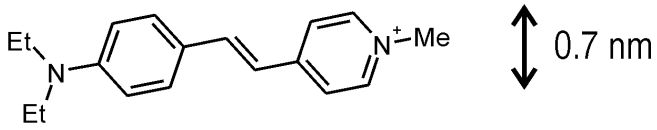

Figure 47: Chemical structure of the stilbene derivative Sigma D-3418, λ_{exc} = 488 nm, λ_{emm} = 550 - 630 nm (depending on the solvent or matrix).[Cao98]

The stilbene derivative is a thin (~ 0.7 nm) and flexible enough molecule that can penetrate into the pores of $AlPO_4$-5 zeolites (pore diameter ~ 0.76 nm), but not to penetrate into the pores of MFI-type structures (pore diameter ~ 0.56 nm). In that way the molecules of the stilbene derivative molecules can be used to stain porous materials with large pores or to stain accessible defect structures in crystals with small pore diameter. Two examples will be shown in the following, using the stilbene-derivative, in which (a) the diffusion coefficient is estimated via a dye-uptake experiment and (b) the stilbene-dyes are used to detect defects.

(a) Estimation of the diffusion coefficient: In the fisrt example, the uptake of the stilbene-derivative by two sol-gel glass samples (with a mesopore diameter of 10 and 4 nm) was studied. The dye-uptake experiment is performed as follows: The material particles (shrapnels of 10-30 µm in size) are placed in a microscopy cavity and embedded in ethylene glycol. A few hours are allowed for the sample to equilibrate, and for the particles to deposit on the coverslip of the microscopy cavity. Then, a sequence of 20 images covering a total time span of ca. 10 minutes is acquired (one image every 30 s, with 2 s acquisition time per image).

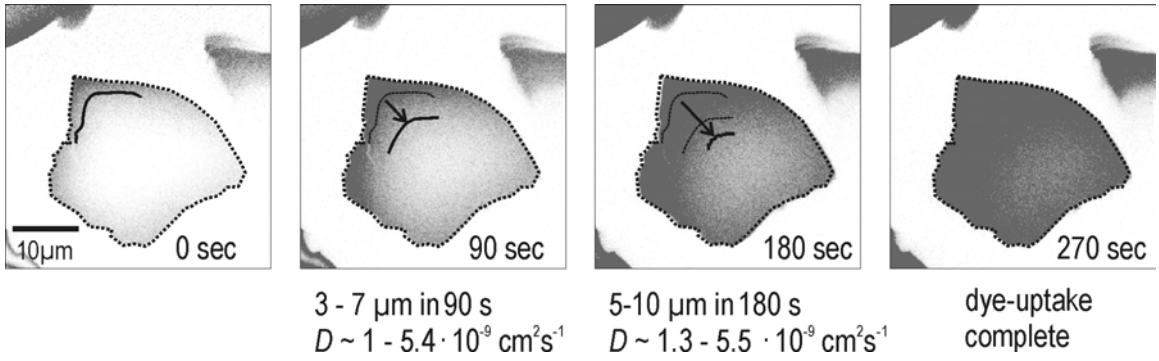

Figure 48: Sequence of images showing the dye uptake of the stilbene derivative in ethylen glycol by a sol-gel-glass sample with an average 10 nm mesopore diameter (Sil100), the acquisition time for one image is 2 s.

After starting the acquisition of the sequence a drop of a stilbene dye solution in ethylen glycol (10^{-6} M) is given into the cavity. After a few seconds the dye diffusing freely in the solution reaches the particle boundary, and starts fluorescing with a higher intensity. The diffusion of the dye into the volume of the porous particle is observed. (see fig. 48). After a few minutes the entire particle is homogenously loaded with the dye. The diffusion coefficient can be roughly estimated from the temporal evolution of the concentration gradient perpendicular to the crystal boundary (cf. section 2.3.1.). For the sample with the 10 nm pores (Sil100, fig.48) the diffusion coefficient lies between 1 and $5.5 \cdot 10^{-9}$ cm^2s^{-1} (it is not possible to determine a more accurate value, beacuse the boundaries of the particles are not well-defined). The diffusion coefficient is an order of magnitude smaller in the material with the 4 nm pores (Sil-40, data not shown).

(b) Staining defect structures: In the second example the investigated sample consists of porous alumina beads covered by two layers of MFI crystals.

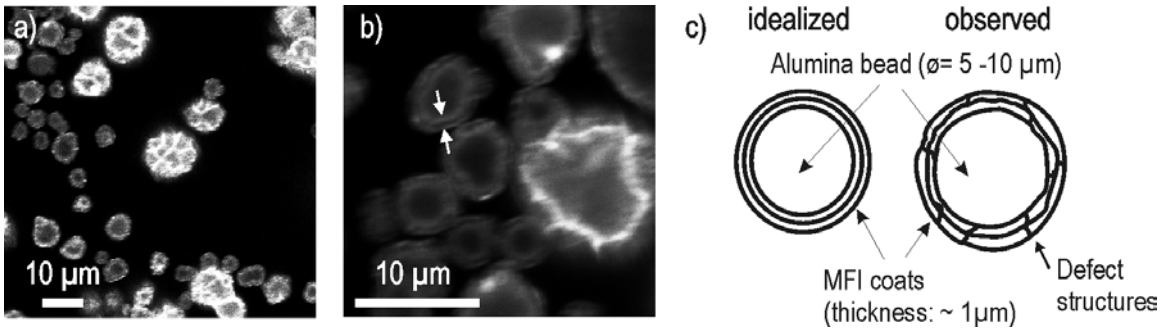

Figure 49: MFI coated alumina beads stained with the stilbene derivative. a) Overview image showing large (diameter > 10 µm) and smaller (diameter ~ 5µm) particles. b) This image shows the particles in detail (optical cross-sections through the middle of the particles. c) The schematical illustration summarizes of the observations made.

The strategy behind such an arrangement of materials is, that the catalytic activity of a material (e.g. alumina loaded with a catalyst) is combined with the size and shape selectivity of the molecular sieve coat (e.g. the MFI crystals). In such a 'hierarchical material' the MFI layer would only allow the passage of the educts and products with the right size in and out of the alumina 'reaction chamber'. It is of crucial importance that the MFI coat is defect-free, since otherwise the size and shape specificity is reduced as the sieving can be circumvented via diffusion though the cracks and defects. In the case of the studied sample it could be shown that the material in question is not free of defects (cf. fig.49). The smaller particles in this sample show less pronounced defects, but it is possible to detect dyes in the inner part of the MFI coat. It is also possible to confirm the presence of the two layers of MFI. Bigger particles have more pronounced defects in the MFI coat. Also it was possible to verify that the coat is formed by two layers of MFI crystals (indicated by the arrows in the right micrograph in fig. 49) - the interlayer region is accessible to dye molecules.

4.1.3 Encapsulated Dyes

The possibility to create ordered dye arrangements that enable light harvesting and energy-transfer has been demonstrated recently using zeolites as host-materials. This has been accomplished, for example, by loading dyes with overlapping absorbtion and emission bands (in a cascade) successively into the channels of Zeolite L [Ban04], [Calzaferri03], [Yatskou03], [Gfeller98]. Apart from the method of loading the host by diffusion of guest species after synthesis (and possibly after calcination), there are more efficient procedures to incorporate chromophores into porous hosts, one being guest inclusion during synthesis, i.e. encapsulation.[Hoppe93], which is often a simpler and more effective procedure to synthesize these host-guest materials (e.g. the micrometer sized dye laser based on $AlPO_4$-5.[Ihlein98], [Vietze98], [Braun00], [Weiss02]).

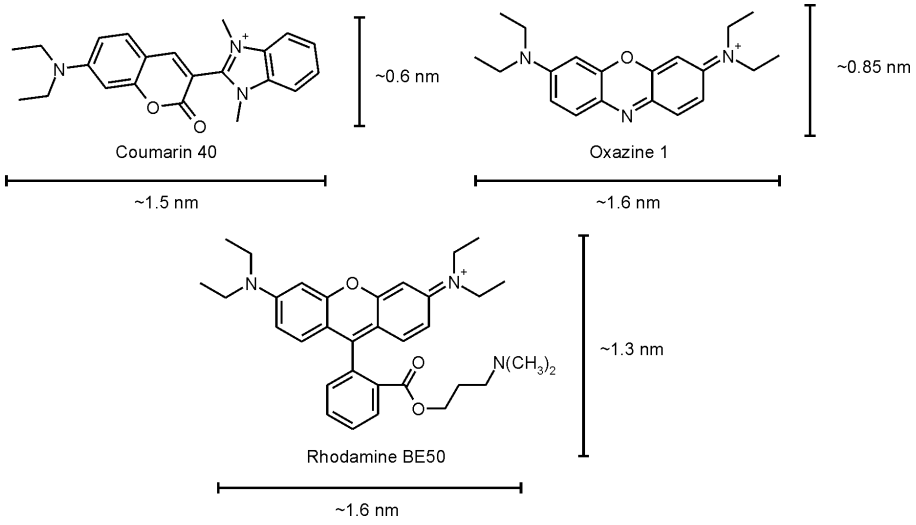

Figure 50: Chemical structures of dyes encapsulated into $AlPO_4$-5 crystals. The sizes are estimated from the bond lengths [Dewar77] and van-der-Waals radii [Bondi64].

Micrometer-sized $AlPO_4$-5 crystals containing three dyes (Coumarin 40, Oxazine-1 and Rhodamine BE50; cf. figure 50) with overlapping emission and absorption bands were sythesized using microwave assisted hydrothermal synthesis (dye encapsulation). The spatial distribution and the energy transfer between the dyes was studied using fluorescence microscopy techniques.[Hellriegel04a]

Spatial distribution: The dyes' spatial distribution was observed via fluorescence microscopy. It was possible to select the fluorescence of the different dyes with appropriate optical filters and selecting appropriate excitation wavelengths.

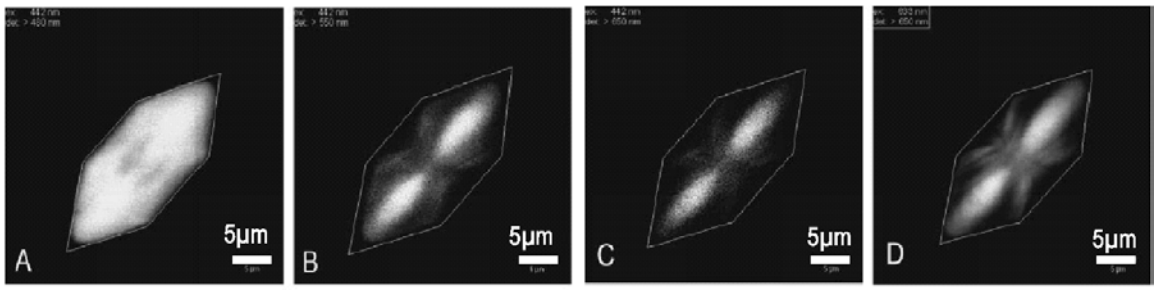

Figure 51: Fluorescence microscopy images of $AlPO_4$-5 crystals loaded with a mixture of fluorescent dyes: Coumarin 40, Rhodamine BE50 and Oxazine 1. a) Fluorescence of Coumarin 40 (excitation at 442 nm, detection above 450 nm). b) Fluorescence of Rhodamine BE (excitation at 442 nm, detection above 550 nm) c) Fluorescence of Oxazine 1 (excitation at 442 nm detection above 650 nm). d) Fluorescence of Oxazine 1 (excitation at 633 nm, detection above 650 nm). Picture taken from [Hellriegel04a]

The spatial distribution of the dyes is visibly heterogenous (cf. fig 51). The thinnest molecule coumarin-40 (excited at 442 nm - absorbtion maximum in $AlPO_4$-5 at 444 nm, emission maximum at *ca.* 490 nm), is found distributed over the entire $AlPO_4$-5 crystal. Polarization dependent measurements also show that the dye is well-oriented along the main crystal axis. The larger molecules Rhodamine BE50 (absorbtion maximum in $AlPO_4$-5 at 563 nm; emission at *ca.* 585 nm) and Oxazine-1 (absorbtion maximum in $AlPO_4$-5 at 642 nm; emission at *ca.* 670 nm) are found localized predominantly in the central region of the crystal. Polarization dependent measurements show a less pronounced preferential orientation along the pore axis. The heterogenous distribution of the bigger dyes versus the smaller dye can be attributed to different crystal growth rates during the formation of the material and different solubilities of the dyes.[Ehrl94] The regions with the fastest growth speed are less selective in the incorporation of foreign (dye) molecules, whereas the slower growing regions will be less tolerant towards a size-mismatch between the pore diameter and molecule width [Hellriegel04a].

Energy transfer: Energy transfer occurs in the samples containing a mixture of all three dyes: (a) It is possible to detect fluorescence above 650 nm (coming from Oxazine-1) if the sample is excited with 442 nm laser. (b) Crystals containing only Oxazine-1 do not show any fluorescence if exited with λ_{ex} = 442 nm.. The analysis of fluorescence lifetimes of the dyes (carried out by Erwin Kneuper) shows that the predominant energy transfer mechanism is radiative. Non-radiative transfer channels could not be observed in the studied samples. The fluorescence life-times for the different dyes were acquired with a time-correlated single-photon counting (TCSPC) microscopy setup. In this measurement (a start-stop experiment) short laser pulses (≈0.2 ns) separated by 12.5 ns exite the sample. The time-lag between excitation and emission of a fluorescence photon (in the 12.5 ns between pulses) can be measured and all recorded arrival times used to make a histogram. This histogram (e.g. fig. 52) can be evaluated to find the fluorescence life-time of the sample.

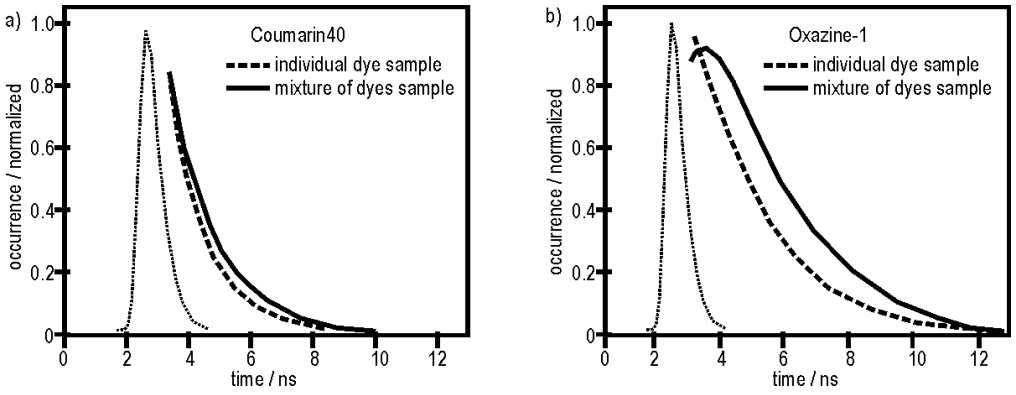

Figure 52: Normalized fluorescence life-time histograms. a) Coumarin40 as the only dye (dashed lines) and in a mixtured sample (solid lines) in AFI. and b) Oxazine-1 as the only dye in AFI (dashed lines) and in a mixtured sample (solid lines). The instrument response function is indicated in a) and b) by thin dotted lines.

The fluorescence lifetimes were acquired for samples in which the dyes are present as a mixture and in crystals containing only one of the dyes. The fluorescence decay time for Coumarin 40, increases slightly (from ca. 0.9 ns to ca. 1.5 ns) on going from the crystals containing the dye alone to crystals containing a mixture of dyes (a non-radiative

mechanism, such as Förster resonant energy transfer or electron transfer, would significantly *reduce* the dye's lifetime). The life-time of Oxazine-1 dos not change significantly (about 2.1 ns). Interestingly, the fluorescence decay of Oxazine-1 in the sample containing the mixture of dyes is preceded by an ascending component (0.7 ± 0.1 ns), indicating that the dye is not being excited by the laser alone but by absorbing the emitted photons from Coumarin 40 and/or Rhodamine BE50. Altogether these observations indicate that in this sample the predominant energy transfer mechanism from Coumarin-40 to Oxazine-1 (via Rhodamine BE) is radiative.[Hellriegel04a]

$AlPO_4$-5 sample with	**average τ / ns (%pop)**	**remarks**
individual dyes		
Coumarin 40	0.50 ± 0.1 (63) 1.3 ± 0.1 (37)	biexponential decay
Oxazine-1	1.9 ± 0.1 (76) 3.1 ± 0.1 (24)	biexponential decay
mixture of dyes		
Coumarin 40	0.9 ± 0.1 (34) 1.8 ± 0.1 (66)	biexponential decay
RhodamineBE	1.1 ± 0.5	triexponential decay(*)
Oxazine-1	-0.67 ± 0.1 2.54 ± 0.1	ascending component before monoexponential decay

(*) the average life-time given in the table is the weighed mean value.

4.2. Photostability of new dyes for SMS

The photostability and the steadiness with which a fluorescent dye molecule emits are crucial parameters, that determine whether a dye is (or not) suitable for SMS studies. A useful way to characterize a fluorophore, is to observe it directly under specific SMS conditions and to compare it with other dyes measured under the same experimental conditions (e.g. matrix polarity, temperature, excitation power and wavelength).

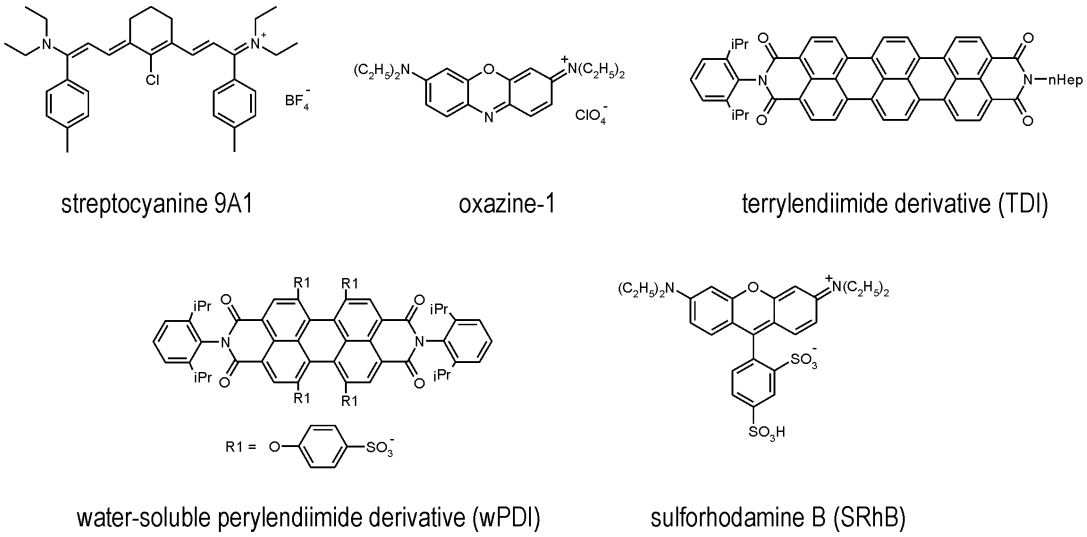

Figure 53: Structural formulas of a selection of dyes used in SMS experiments. The typical photostability parameters and blinking behaviour of two new dyes, streptocyanine 9A1 and a water-soluble perylene-diimide dye (wPDI) are characterized in comparison to other, previously characterized dyes Oxazine-1 (Ox1), terrylene-diimide derivative (TDI) and Sulforhodamine B (SRhB)

In this way it is possible to obtain a comparison table (cf. below and complete table in appendix) between other, commonly used or commercially availiable dye moelcules that absorb and fluoresce in the same spectral region. In this section the results of such a study for two new fluorescent dyes, a water-soluble perylen-diimide derivative (wPDI, from Prof. Müllen, Mainz) and a streptocyanine dye (9A1, Dr. Corinne Payrastre, Toulouse) are presented. The chemical structures of the dyes are depicted in figure 53.

a) Water-soluble perylen-diimide derivative (wPDI): The group of the so-called rylene dyes (perylene, terrylene etc.) are known for their exceptional photophysical quality and their usefulness in SMS studies. A major limitation for these molecules, however, is their poor solubility, especially in aqueous media. Recently a water soluble perylen dye could be synthesized by attaching suitable side-chains to the perylen backbone [Qu04] (in the group of Prof. Dr. Klaus Müllen, MPI für Polymerforschung, Mainz). A study was carried out for this molecule showing that it is particularly stable for SMS applications, in comparison to different dyes, in particular to sulforhodamine B (SRhB) which absorbs and amits in the same spectral region (cf. figure 54).

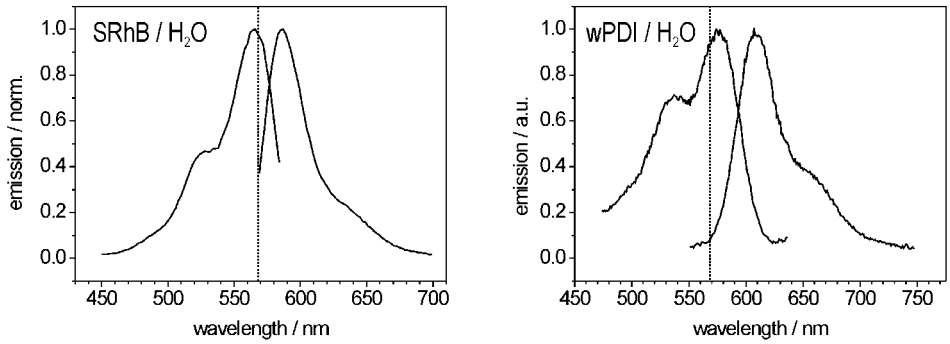

Figure 54: Excitation and emission spectra of sulforhodamine B (left) and perylen-derivative (right). λ_{ex}=568 nm (indicated by dashed line) and λ_{det} = 587 nm for SRhB and λ_{det}=610 nm for wPDI.

wPDI and SRhB are embedded in low concentrations (ca. 10^{-9} M) in poly-vinylalcohol (PVA), which mimicks a polar (aqueous) environment, as would be found for instance in a cell or in a protein pocket. In fluorescence microscopy images the samples show spatially separated and immobile diffraction limited fluorescence spots of the individual wPDI and SRhB molecules. The fluorescence versus time (the intensity transients) can be recorded for individual molecules using the confocal microscope described in section 3.1. The dyes are excited with circularly polarized light (using a λ/4 retardation plate in front of the objective barrel) and a wavelength of 568 nm (Kr^+-laser), and 61 µW at the entrance of the objective barrel.

On the level of individual molecules ca. 100 individual intensity transients are acquired from individual wPDI and SRhB molecules (both in PVA). The number of emitted photons (under consideration of the setup's detection efficiency of 3%) for every molecule is obtained from the transients (see figure 55).

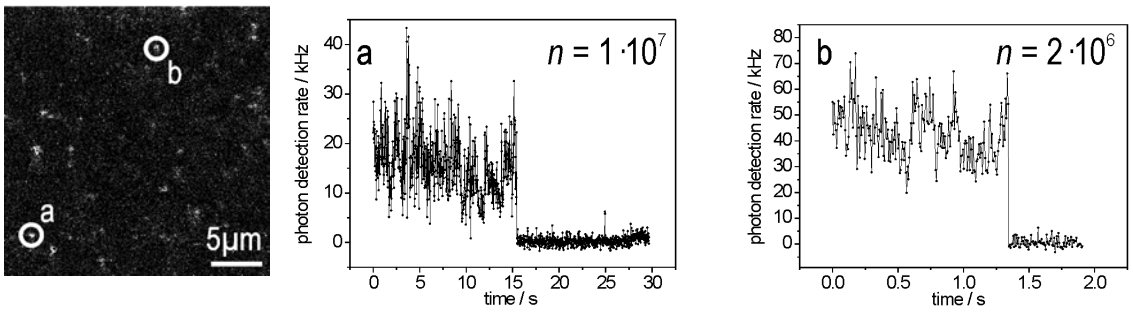

Figure 55: Individual intensity transients are obtained from the diffraction limited spots, here due to individual wPDI molecules in PVA, on the fluorescence microscopy image.

The individual numbers of emitted phtons are sorted and assigned a relative rank (j/R, where j is the absolute rank in R total ranks). j/R is plotted versus n, and this curve corresponds to the complementary cumulative probability function $C(N)$ (cf. eq. 40, section 3.2.4). The j/R versus n plots for wPDI/PVA and SRhB/PVA are in fig. 56:

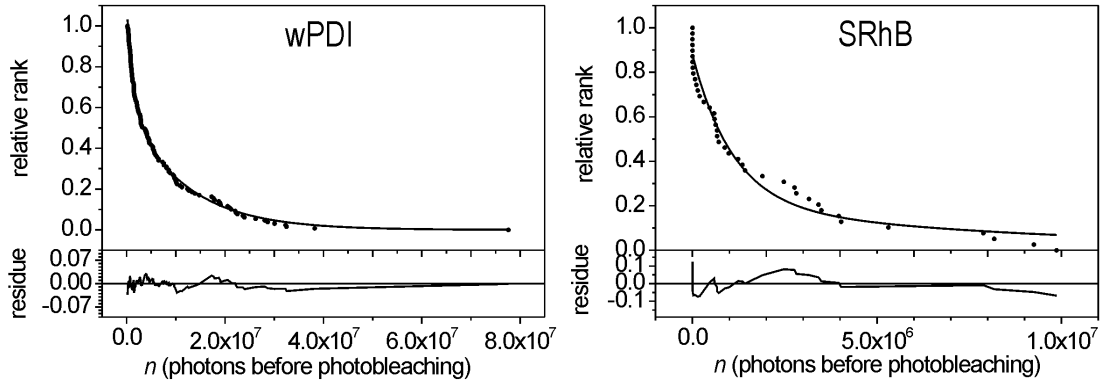

Figure 56: A population analysis is the most appropriate method to obtain a characteristic number of emitted photons prior to photobleaching for the obtained data. A double exponential decay was used to fit the data to eq. 40 (cf. section 3.2.4, and below).

Two populations of differently bleaching molecules are found to coexist in the samples - the best fit is obtained with a double exponential decay, according to eq.40 (section 3.2.4, and below). The results are summarized in the following table:

	SRhB / PVA	**wPDI / PVA**
R	42	130
m	2	2
$A_1 : A_2$	3	1.3
$\langle n_1 \rangle$ / 10^6 photons	2.3 ± 0.1	11 ± 0.2
$\langle n_2 \rangle$ / 10^6 photons	0.003 ± 0.001	0.1 ± 0.005
$\langle n_{AVG} \rangle$ / 10^6 photons	1.7 ± 0.1	6.7 ± 0.2

$$C(N) = \sum_{i=1}^{m} A_i \exp(-N / \langle n_{i,FL} \rangle) \qquad \text{(eq. 40, section 3.2.4)}$$

An average number of emitted photons under consideration of the statistical weight of each population gives an average characteristic number of emitted photons before photobleaching for both dyes $n_{AVG} = (6.7 \cdot \pm\ 0.2)\ 10^6$ in the case of wPDI and $n_{AVG} = (1.7 \cdot \pm\ 0.1)\ 10^6$ for SRhB. wPDI is emits roughly four times more photons than SRhB. The blinking - or on/off - behaviour does not show a pronounced difference between the two molecules, and is currently being characterized in detail. A similar study has been [Margineanu04] published recently, but fails to give a number of emitted photons prior to photobleaching for the compared dyes (wPDI and SRhB). The only statement that can be made from [Margineau04] is that wPDI has a superior quality in comparison to Sulforhodamine B (SRhB). The study presented here confirms this observation and allows for a a more quantitative statement.

b) Streptocyanine 9A1: A new streptocyanine dye (9A1, synthesized in the group of Corinne Payrastre in Toulouse, France)[Hellriegel04] was used in the context of an SMS diffusion experiment (see section 4.5). The dye was studied in a similar way as described above for wPDI, using λ_{ex} = 633 nm (34 µW); the matrix is PMMA. The results are summarized in figure 57. The ranked data is fitted according to equation 40 (fig. 57c and 57d).

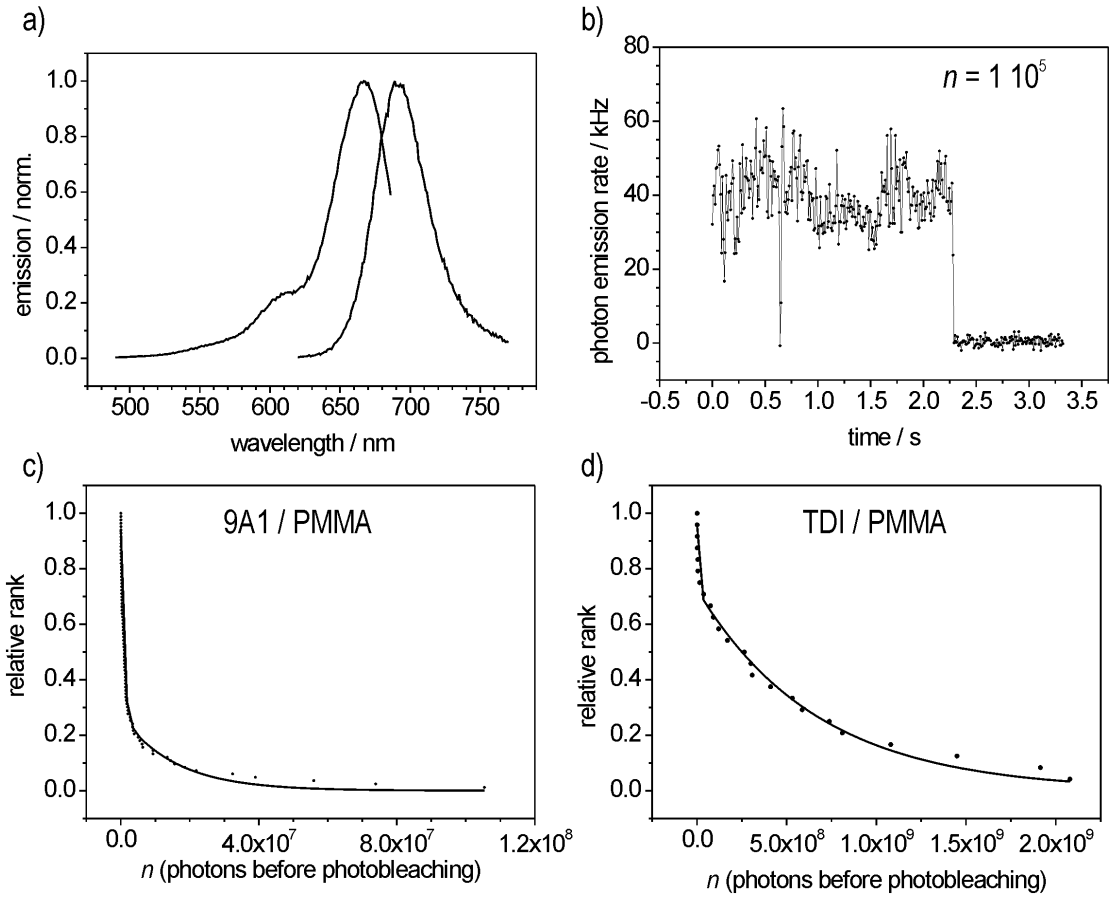

Figure 57: Photostability of 9A1 in comparison to TDI. a) Excitation (λ_{det} = 690 nm) and emission spectra of 9A1 (λ_{ex}=633 nm). b) Typical instensity transient of a single 9A1 molecule in PMMA. c) and d) show the ranked data for 9A1 and TDI in PMMA and the respective fits according to eq. 40.

The results of the fits according to equation 40 are summarized in the following table:

	9A1 / PMMA	**TDI / PMMA**
R	83	25
m	2	2
$A_1 : A_2$	2.3	0.4
$\langle n_1 \rangle$ / 10^6 photons	0.8 ± 0.05	3.7 ± 0.9
$\langle n_2 \rangle$ / 10^6 photons	15 ± 2.5	(6.7± 0.7) · 10^4
$\langle n_{AVG} \rangle$ / 10^6 photons	4.4 ± 1.7	(1.9± 0.9) · 10^4

Global comparison of dye photostability: A table with photostability parameters has been acquired for many different dyes used in this group over the past years, an excerpt is given here (the full table is given in the appendix to this thesis).

dye	**Matrix**	**λ_{ex} / nm**	**I_{ex} / µW**	**$\langle n \rangle$ / 10^6 Photons**
TDI	PMMA	633	34	(1.5 ± 0.8)·10^4
Oxazine-1	PMMA	633	34	40 ± 10
Streptocynine 9A1	PMMA	633	34	4.4 ± 0.7
Cy-5	PMMA	633	34	4 ± 2
wPDI	PVA	568	61	6.7 ± 0.2
wPDI	PMMA	568	61	200 ± 90
SulforhodamineB	PVA	568	61	1.7 ± 0.1

wPDI is, so far, the most photostable water-soluble dye in the 568 nm range, being about 4 times more photostable than the comercially availiable and commonly used dye SulforhodamineB. 9A1 is significantly less stable than TDI or Oxazine-1, but is comparable to Cy-5, a commercially availiable dye, commonly employed in SMS studies.

4.3. Orientational Distribution of Oxazine Dyes in $AlPO_4$-5

Introduction: Host-guest materials based on zeolites and incorporated dye molecules are usually idealized as highly organized systems in which the arrangement of molecules adapts to the crystal structure of the host material, for example the dye molecules aligning to the channel structure. This chapter presents an SMS study that, for the first time and in a direct way, revealed the orientational distribution of various guest molecules of different size encapsulated into the unidimensional channels of $AlPO_4$-5 during synthesis.

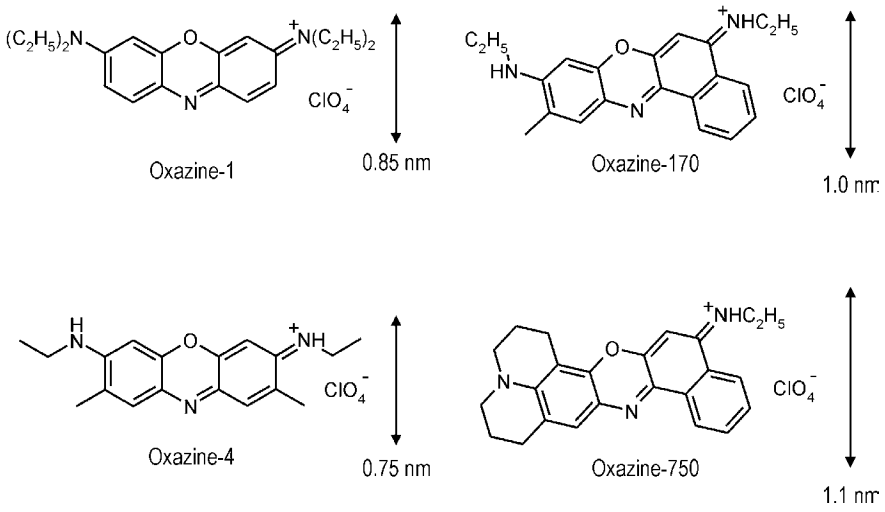

Figure 58: Chemical structures of dye molecules incorporated into the channels of $AlPO_4$-5. The sizes have been calculated from the bond lengths [Dewar77] and van-der-Waals radii [Bondi64].

$AlPO_4$-5 has unidimensional, nearly cylindrical pores with a diameter of 0.73 nm which are oriented parallel to the main crystal axis. Molecules incorporated in this matrix may align more or less well to the pores, in dependence of their respective sizes. Four different Oxazine dyes, that is, molecules with a comparable chemical structure but differing in size (cf. fig.58 for the structures and sizes) were incorporated into $AlPO_4$-5 crystals during microwave assisted synthesis. The central question addressed by this study is how the interplay between guest and host-size determines the structural arrangement in the resulting host-guest material.

From the structures of $AlPO_4$-5 and of the Oxazine molecules the expected orientational distribution would be as follows: The slimmest molecules, Oxazine-1 and -4, (estimated width 0.85 and 0.75 nm respectively) tightly fit the pores of $AlPO_4$-5 (0.73 nm), considering that the molecules and the host structure also have a certain degree of flexibility. Oxazine-1 and -4 should therefore become incorporated aligned more or less perfectly with the pore orientation. The larger dyes, Oxazine-170 and -750, (estimated width 1.0 and 1.1 nm respectively) are not expected to align with the pores in the resulting host-guest material, as their size significantly exceeds the pore size of $AlPO_4$-5. Instead, these molecules are likely to induce defects upon encapsulation and thus become incorporated in random orientations. Schematically:

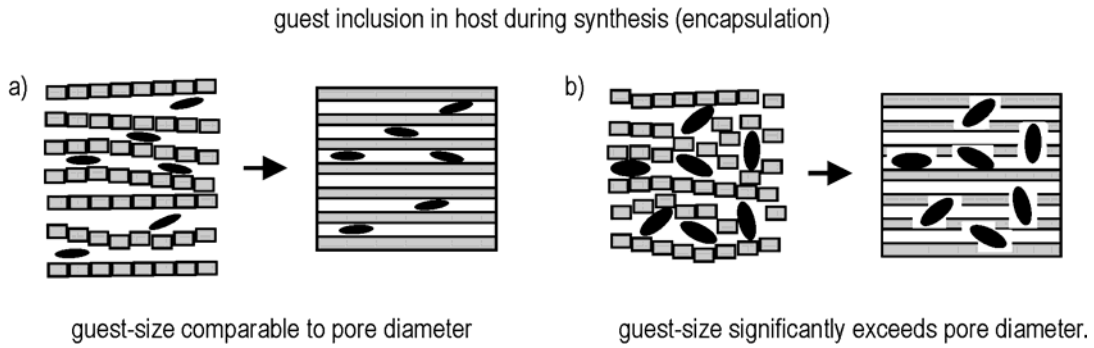

Figure 59: Encapsulation process of a guest species (dye) into a porous host material such as $AlPO_4$-5. a) If the guest is small enough its encapsulation will not significantly affect the host structure. b) If the size mismatch is significant the molecular guests are likely to induce defects in the host structure and may become incorporated in random orientations.

The orientational distribution of the dyes with respect to the crystal main axis is obtained directly via polarization dependent SMS measurements. Before turning to the individual results it is important to note here that polarization dependent measurements conducted on the level of molecule *ensembles*, while possibly pointing to the *presence* of a preferential orientation of the guests, will fail to describe the *distribution* of orientations. [Hellriegel03]

The orientational distribution of a dye in the pores of $AlPO_4$-5 is in the following described in detail for the oxazine-4 / $AlPO_4$-5 sample. The orientational distribution of the other dyes (described for example in [Hellriegel03] and [Seebacher02]) are acquired in the same way.

Orientational distributrion of Oxazine-4 in $AlPO_4$-5: The orientational angle of an individual Oxazine-4 molecule is determined by analyzing the polarization dependent emission data (see figure 60b). The polarization angle of the excitation light is constantly modulated as the fluorescence intensity of an individual fluorophore is recorded (cf. section 3.2..3.). The orientation angle of the pores is obtained from transmission images of the $AlPO_4$-5 crystals with an accuracy of ±3°.

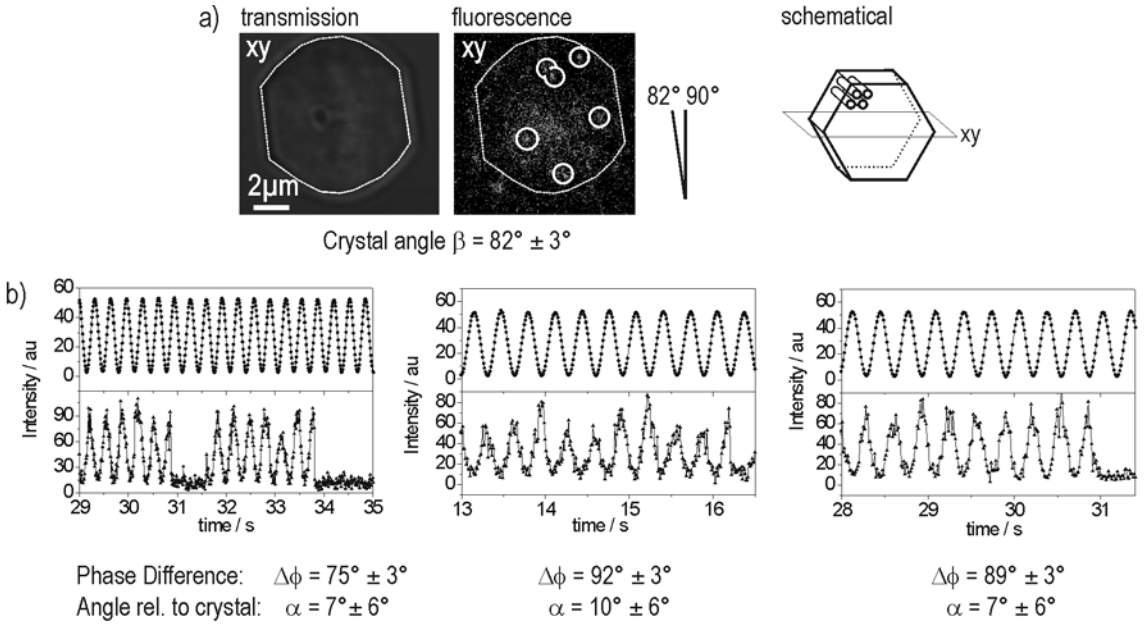

Figure 60: Orienations of individual Oxazine-4 molecules in $AlPO_4$-5. a) Typical trasnsmission and fluorescence images (cross-sections as indicated in the schematical drawing) showing the diffraction limited patterns produced by single molecules. b) Three examples for polarization dependent data used to determine the angle of a molecule with respect to the crystal axis. (Note the abrupt photobleaching / blinking steps in the curves that point to the presence of individual molecules)

The angles of 62 individual molecules in 5 different crystals are plotted in figure 61a. The histogram in figure 61b shows that the dyes have a preferential orientation along the main crystal axis with a narrow distribution width. The half-width at half-maximum of the curve is determined to be 14°± 2 using a Gaussian to model the curve. It is also possible to notice that a small population of moleucles is found oriented transversally to the main pore direction.

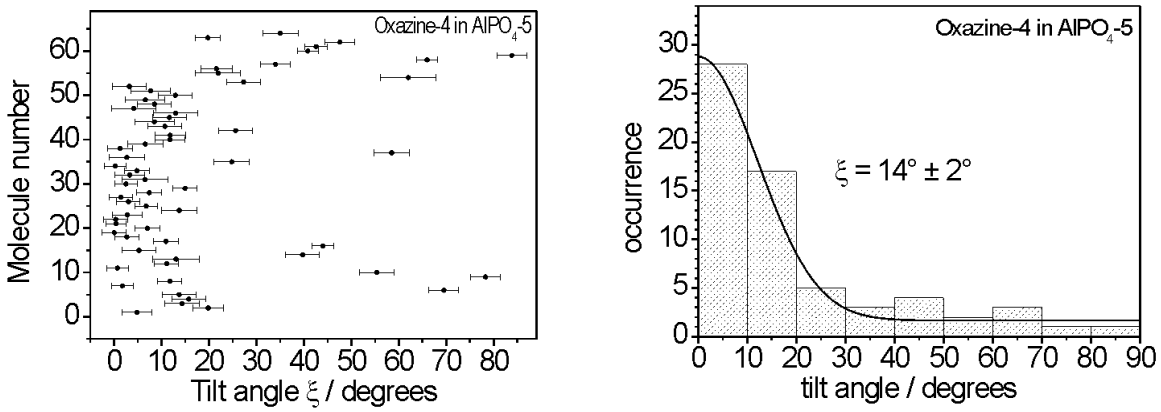

Figure 61: Orientational distribution of Oxazine-4 in $AlPO_4$-5. a) Raw data b) Histogram showing a narrow ($\xi = \pm 14°$) distribution around the main crystal axis.

Orientational distribution of oxazine dyes in $AlPO_4$-5: The histograms for all studied molecules are shown in figure 62. The histogrammes confirm that the distribution of the slimmer dyes, oxazine-1 and oxazine-4 is narrow, whereas the distribution of the largest molecule oxazine-750 is random. Interestingly, oxazine-170, with a 'thickness' of ~1.0 nm - clearly exceeding the pore size (0.7 nm) shows a broad distribution, but still with a preferential orientation along the pores.

In all cases the incorporation of dyes into the channels of $AlPO_4$-5 is not perfect. Even the slimmest molecules oxazine-1 and oxazine-4 become incorporated transversally to the pores, possibly in pronounced defects.

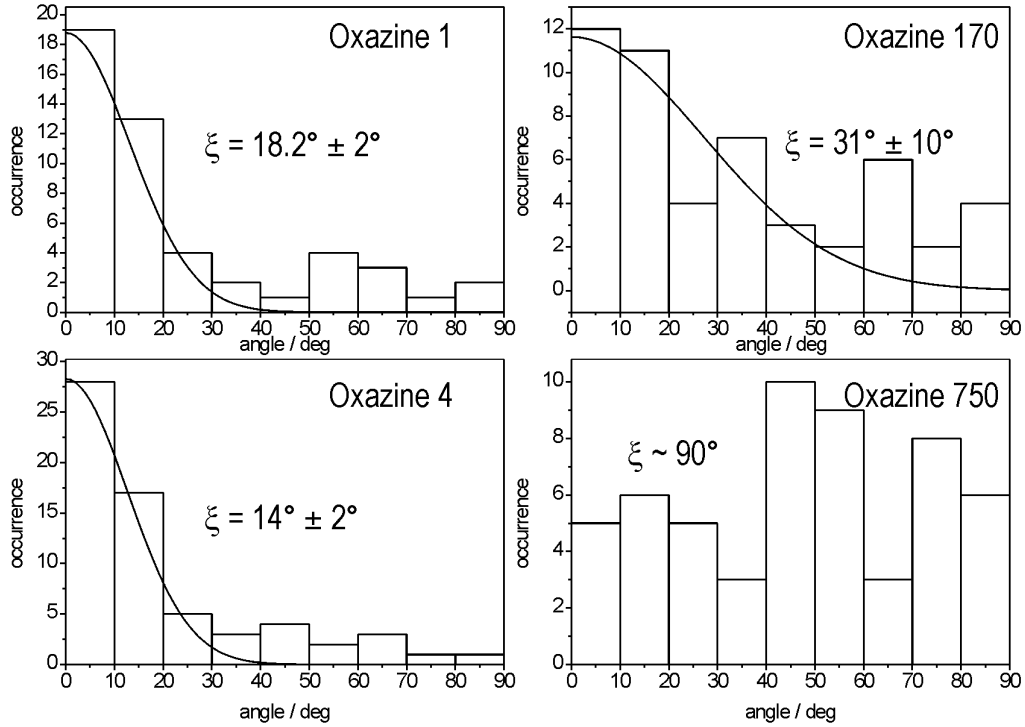

Figure 62: Orientational distribution histogrammes for the four studied dye molecules. (An angle of 0° is defined as parallel to the pore orientation). ξ denotes the half width at half maximum of the model curves.

Summary: The orientational distribution of four differently sized oxazine dyes incorporated in $AlPO_4$-5 crystals was reconstructed from the orientations of many individual molecules. It is shown that a host system like $AlPO_4$-5 can still have a directing influence on the incorporation of guest molecules, even when the sizes of these molecules exceed the diameter of the channels, as is the case for oxazine-170. There is, however, an upper size limit for this effect, the largest dye, oxazine-750 with approximately 1.1 nm width does not become incorporated with a noticeable preferential orientation. A comparison between this method and conventional ensemble studies clearly shows that the SMS approach allows a description of the dye orientational distribution at a more fundamental level, leading to the actual orientational distribution function.

4.4. Translational Diffusion of TDI Molecules in MCM41S Monoliths

The diffusion of a molecular species (terrylendiimide dye molecules, TDI, cf. fig 63) in a structured molecular sieve was observed for the first time in 2002 via SMS and confocal microscopy and analysed by single particle tracking. The work described in this sub-section was published in [Seebacher02] (cf. also[Seebacher02d] and [Hellriegel00]) and introduced the observation of molecular diffusion via particle tracking in structured mesoporous materials such as M41S and SBA-15.

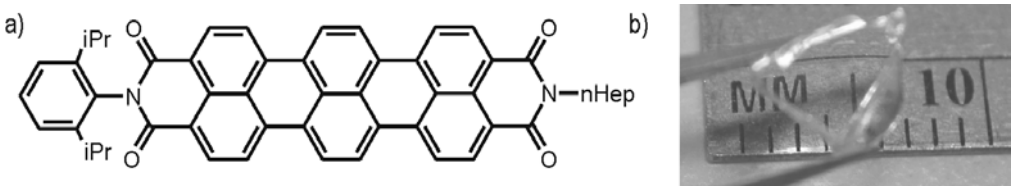

Figure 63 TDI in M41S sample: a) Strctural formula of the used terrylendiimide-derivative (TDI). b) General appearance of monolithic M41S particles.

The monolithic, centimetre sized M41S materials(see fig.59) were synthesized (in the group of Prof. P. Behrens) via a liquid crystal templating mechanism, using the non-ionic surfactant, monododecyloctaethylene-glycol-ether, OMO, as template and tetramethoxy-silane, TMOS as silica source.[Attard95], [Gölltner97]. The structure and the porosity of the material were confirmed by X-ray diffractometry, giving a nominal pore size of 4 nm. The dye molecules were present in the synthesis batch prior to the condensation of the solid matrix around the liquid crystalline micellar template. The concentration of TDI in the synthesis batch was in the order of 10^{-11} M. The material was left uncalcined after formation of the solid matrix. Thus the pores contained template micelles and the TDI molecules, which were probably situated in the hydrophobic part of the micellar structure since TDI is not soluble in polar media.

Using fluorescence correlation spectroscopy FCS it was possible to determine the diffusion coefficient for the motion of TDI molecules dissolved in chloroform ($CHCl_3$), $D_{solv} = 0.9 \cdot 10^{-6}$ cm^2s^{-1} and in the pure liquid crystal phase formed by the template OMO,

$D_{LC} = 2.7 \cdot 10^{-8}$ cm^{2}s^{-1} (sililar measurements confirming the data can be found in [Mahurin04] and in [Kawai04]) The diffusion coefficient for the motion of TDI in the M41S material was obtained by evaluating trajectories of individual molecules. These first observations were made using a confocal microscope and have therefore a limited temporal resolution of 4 s per frame. For this reason the description of the diffusion - in terms of a diffusion coefficient - is based on the population analysis performed for many individual molecules. The effective diffusion coefficient of a fictitious average TDI molecule in this material is found to be $D = 3 \cdot 10^{-10}$ cm^{2}s^{-1}. The full advantages of the tracking method, that is an analysis based on individual trajectories (cf. section 3.2.1.) could not be explored in this study because the trajectories were too short.

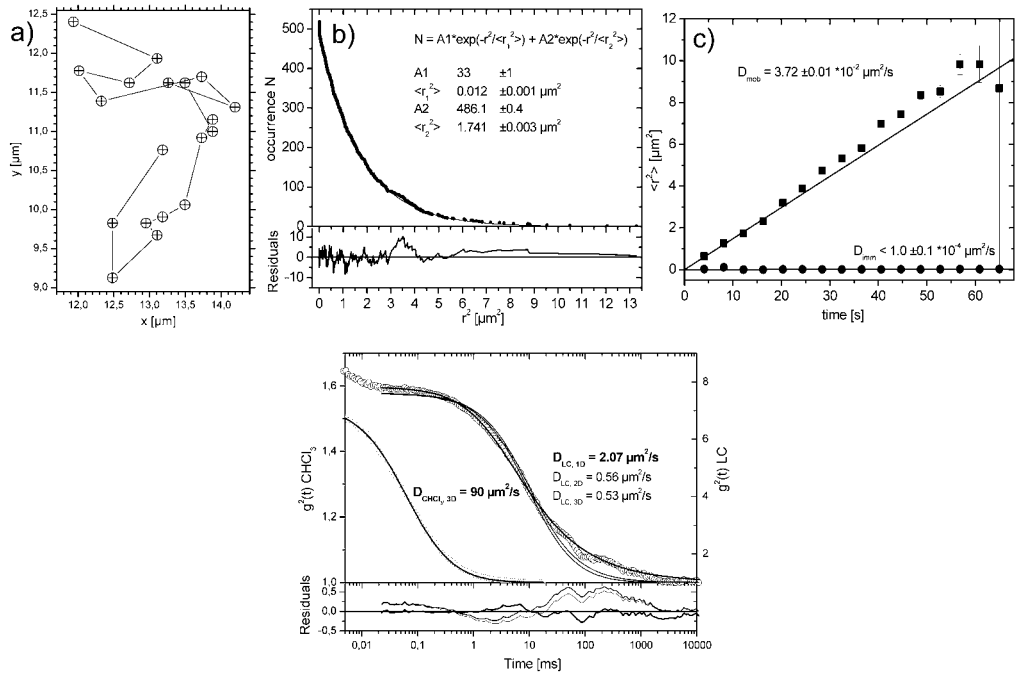

Figure 64: The panel shows the analysis of molecular diffusion in an M41S host, in the underlying liquid crystalline phase and in 'free' solution. a) Trajectory of TDI in MCM-41 (δt = 4 s.) b) Population analysis (see section 3.2.1.) and c) MSD versus time plot for the two found populations. Bottom: FCS analysis of TDI diffusion in $CHCl_3$ and in the micellar liquid crystalline phase of the template OMO. The various fit curves in the graph demonstrate that the best model for the diffusion in the LC corresponds to a one-dimensional random walk. (from [Seebacher02])

Despite the limitations imposed by the low temporal resolution of the confocal setup and the small number of steps per trajectory it is possible, however, to notice pronounced curves in the individual trajectories: This implies that the pores are either interconnected or have a high tortuosity (or both). Furthermore it was also possible to observe a population of immobilized molecules (10% of all observed molecules) coexisting with a mobile population in the sample. Polarization dependent measurements indicated that these molecules show orientational dynamics (data not shown here), and must thus be incorporated in comparatively large voids (of 3-30 nm in size).

The diffusion coefficient D of the diffusing molecules is decreased by almost two orders of magnitude on going from the 'free' solution ($D_{solv} = 0.9\ 10^{-6}$ cm^2s^{-1}) to the liquid crystalline template ($D = 2.7\ 10^{-8}$ cm^2s^{-1}) and another two orders of magnitude on going from the liquid crystalline template to the monolithic host ($D = 3\ 10^{-10}$ cm^2s^{-1}). This decrease of the diffusivity can be attributed to two major effects: (a) An increased viscosity in the compressed LC template leading to an overall slower diffusion; and (b) a high tortuosity of the channels, which could not be resolved, contributing to a decrease of the diffusivity on the relevant temporal and spatial scale.

Altogether, these measurements showed for the first time the direct detection of heterogeneities (i.e. each molecule showing its own behavior) and sub-populations (i.e. diffusing and non-diffusing molecules coexisting in the same sample) in the diffusional behavior of molecules in a porous material. These examinations marked the first step in the direction of using single particle tracking to evaluate diffusion in the volume of porous materials. In spite of the obvious shortcommings of the used setup - the poor temporal resolution of the confocal microscope in the acquisition of image sequences - it was possible to detect tortuous trajectories and to detect the presence of sub-populations of (diffusing and immobile) molecules coexisting in the same sample. This information is not directly availiable from other methods that probe diffusion. A more detailed analysis of diffusion in porous materials could be obtained with the widefield imaging setup (cf. next sections) which has a significantly better temporal resolution

4.5. Translational Diffusion of 9A1 Molecules in Sol-Gel Glass

Introduction: While the investigations described in the preceding section already provided a substantial improvement in the characterization of molecular diffusion the temporal resolution limited the description of the diffusion processes taking place in that porous material. A better temporal resolution could be achieved by using the widefiled-imaging technique to acquire sequences of images. Already in the first experiments it was possible to observe the diffusion of individual molecules in a porous material with a time resolution of up to 50 ms (this is an improvement of nearly two orders of magnitude in time resolution compared to the confocal technique). These first examinations with this setup were carried out to characterize diffusion of a streptocyanine dye (9A1, figure 65a) incorporated into a cast monolithic sol-gel glass (figure 65b).

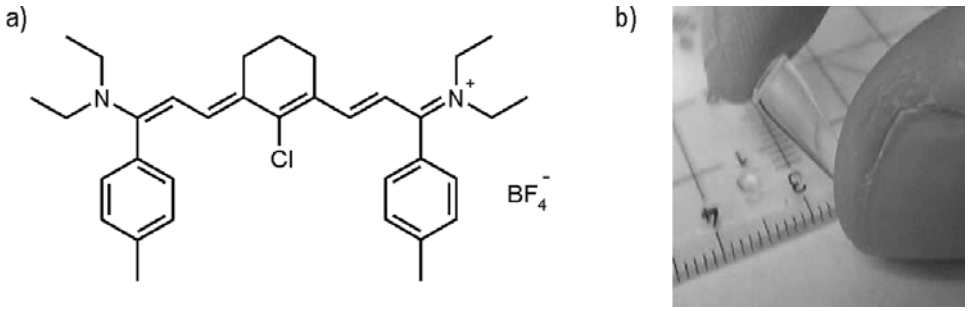

Material Name	Microporosity	Mesoporosity
M22	0.8 nm	22.4 nm
M3	0.8 nm	3.1 nm

Figure 65: Streptocyanine 9A1 in sol-gel-glass samples. a) Structural formula of streptocyanine dye 9A1 b) Typical appearance of a cast, centimeter-sized, monolithic sol-gel-glass. Table: The two investigated materials were named after the differing size of the mesopores (which have been estimated from adsorption isotherms).

The sol-gel glass materials doped with 9A1 were synthesized (in the group of Dr. Ross Brown, CNRS Pau, France) according to [Brinker90] and form macroscopic cm-sized bodies with a broad distribution of porosities depending on the ratio of silica source (TMOS), water and methanol used in the synthesis procedure. Two recipes differing in the silica source concentration were used to produce materials differing in porosity. The resulting porous materials do not show any structure in XRD measurements, they are completely amorphous. The pore architecture in both samples does not show any order. The porosity is estimated by recording adsorption isotherms.. The pore sizes are distributed in two populations: a) Micropores of similar size (in average 0.8 nm, from isotherms), which occur in both materials, and b) mesopores which are distributed around 3.1 nm and 22.4 nm in each type of material. The materials are named M3 and M22, respectively, reflecting the difference in mesopore size (cf. table in fig.65).

Preliminary experiments on the level of molecule ensembles showed that the inner voids of the material is accessible to solvents and dyes from the outside, and that the pores extend to the inner volume of the sample (see section 4.1.2). From these experiments it was possible to estimate the diffusion coefficients which are in the order of 10^{-9} cm^2s^{-1} and 10^{-10} cm^2s^{-1} for M22 and M3 respectively.

Analysis of Diffusion using SMS: The sol-gel-particles particles containing 9A1 at an estimated concentration of 10^{-10} M are embedded in ethylen glycol and allowed to equillibrate for a few hours. The samples are then examined under the widefield imaging microscope. The focal plane is adjusted, so that the measurements were made at a depth of at least 10µm inside the particle. The concentration of 9A1 in these samples is low enough so that the fluorescence originating at the individual molecules produces distinguishabe patterns in the recorded images. Sequences of images consisting of 500 images separated typically by a time interval of ~100 ms were obtained in the form of movies (see fig.66). The positions of the patterns are obtained from the sequences with a typical accuracy of 50 nm using the software described in the experimental section.

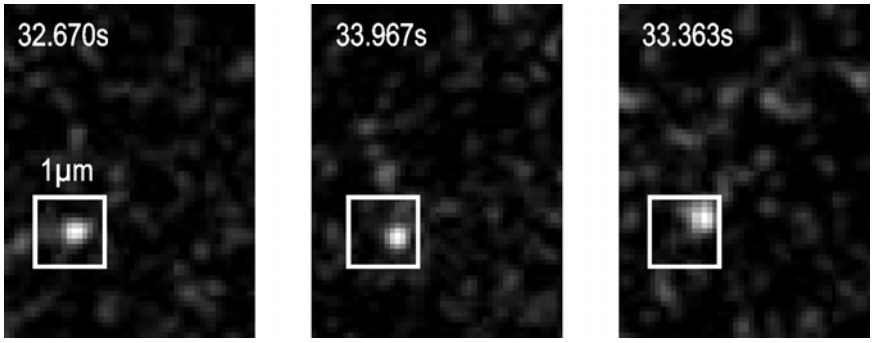

Figure 66: Sequence of images showing diffusion of a 9A1 molecule in M22.

Two sets of trajectories for molecules diffusing in M3 and M22 are shown in fig.67. The diffusion of 9A1 molecules in M22 is evident. In this sample the individual molecules diffuse over a distance of several micrometers (fig.63a). In M3 the diffusion is barely perceptible on this scale of length (see fig 63b and inset).

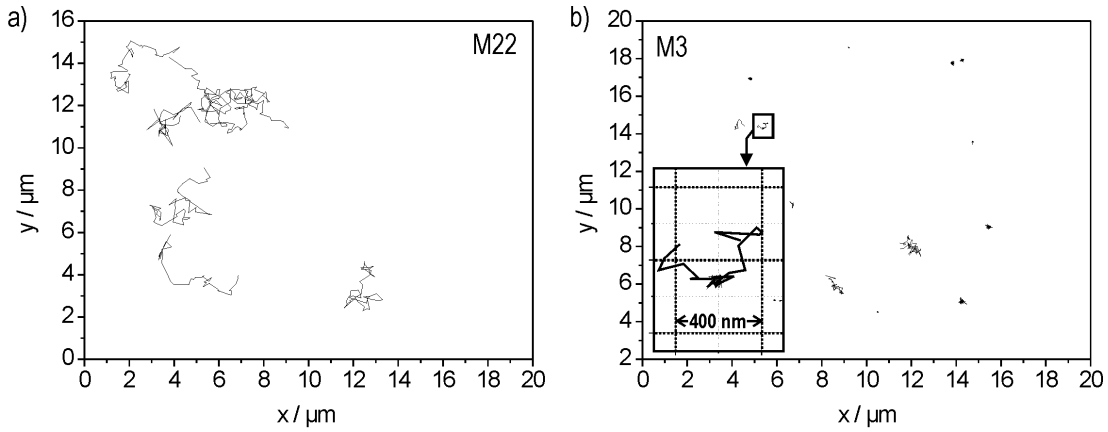

Figure 67: Diffusion trajectories of 9A1 in a) M22 and b) in M3 sol-gel-glasses (the acquisition time is 100ms per frame, in both graphs). The trajectories of 9A1 in M3 barely show any movement on this scale of length (see inset).

Non-diffusing molecules, that is, molecules that do not appear to be moving within the spatial resolution of the apparatus, occur in both samples, but in different proportions: Less than 20% of the observed molecules in M22 are non-diffusing, whereas in M3 this population reaches 80%. The analysis of these non-diffusing sub-populations, is described in more detail later.

Global Analysis of Diffusion: The motion of all molecules in the diffusing fractions in M22 and M3 can be analysed to give an effective diffusion coefficient, D_{eff}. These effective diffusion coefficients are $D_{eff} = 4.7 \cdot 10^{-9}$ cm^2s^{-1} and $D_{eff} = 3.5 \cdot 10^{-10}$ cm^2s^{-1} in M22 and M3, respectively, under assumption of normal isotropic motion (cf. figure 68).

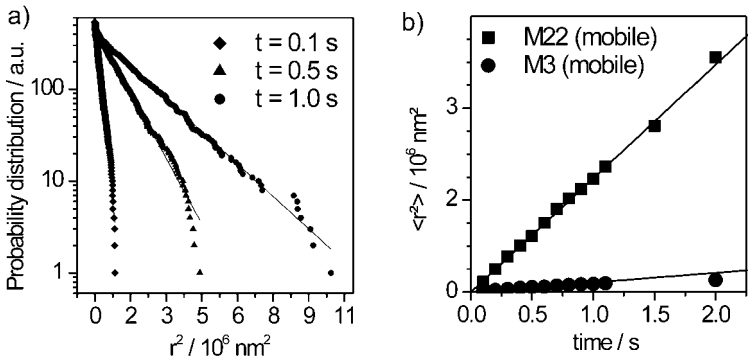

Figure 68: Global analysis of diffusion of 9A1 in M22 and M3. a) Shows the population analysis for the mobile fraction in M22. b) The mean square displacements obtained from the population analysis are plotted versus time for M22 and M3, giving the effective diffusion coefficients $D_{eff} = 4.7 \cdot 10^{-9}$ cm^2s^{-1} and $D_{eff} = 3.5 \cdot 10^{-10}$ cm^2s^{-1} respectively.

The expected reduction in the diffusion coefficient in the material with the smaller pores is confirmed. A number of factors may influence the diffusion of a molecule containing both micro and mesopores. One of them is the question as to whether the molecule is diffusing freely in the pore fluid, or if it diffuses along the surface of the pore wall. Factors likely to influence free diffusion include: the rate of diffusion in the bulk of the pore fluid and the facility of alignment of the molecular long axis with the pore axis to pass pore windows. Both these processes will slow down if there is an increase of the viscosity due to the presence of more wall-fluid interactions in narrower pores in comparison to the wide pores. Surface diffusion is also expected to be slower in the narrow pore gel because of the increase of surface area to be explored in order to make a 'step' of given length in either gel. With the spatial and temporal resolution of the experimental setup it is, however not possible to distinguish the contributions of these processes in the data.

Analysis of Individual Trajectories in M3: On turning to the analysis of the individual trajectories further differences in the diffusional behaviour, that is, differences other than merely an overall decrease of the diffusion coefficient *D* become apparent. In some cases a significant heterogeneous behaviour of the molecules diffusing in M3 could be detected. These molecules seem to interrupted in their diffusion by periods in which the molecules appeared to be trapped in a region with less than 50 nm in diameter. Such distinguishable trapping regions do not occur in the trajectories of molecules diffusing in M22. Two trajectories of 9A1 diffusing in M3 and which show particularly pronounced trapping regions are depicted in fig. 69.

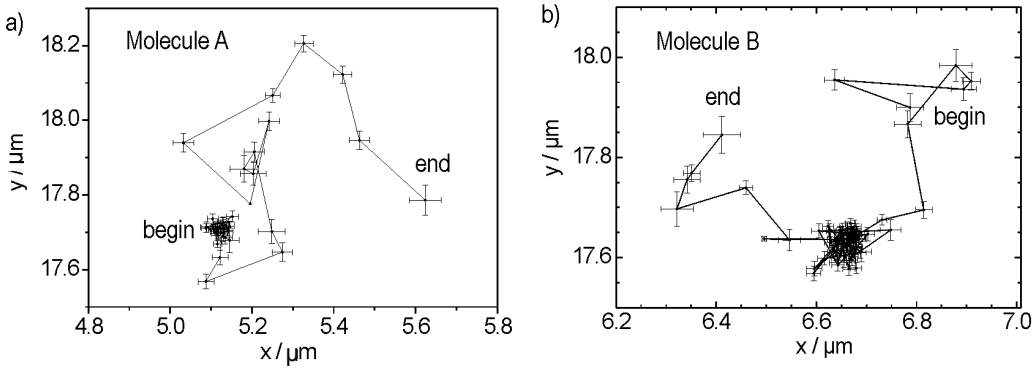

Figure 69: Two trajectories of 9A1 diffusing in M3. a) The trajectory of this molecule (A) begins in a region in which it seems to be immobile. b) The trajectory of this molecule (B) is interrupted by a region in which it seems to remain immobile for approximately 6 seconds. (The time lag between steps is 100 ms in both trajectories)

In the first example, the trajectory of molecule A begins in a region which is smaller than the mean positioning accuracy of 50 nm and seems to remain confined there. After ca. 5 seconds it leaves the region and visibly diffuses for another 1.5 seconds before it disappears. The trajectory of molecule B is interrupted by such a region in which the molecule appears to remain immobile. To obtain a more proper value for the diffusion coefficient the trapped and the mobile parts of the trajectory have to be separated. This is done by analysing the probability distributions of mean square displacements according to $C(U,t)$.

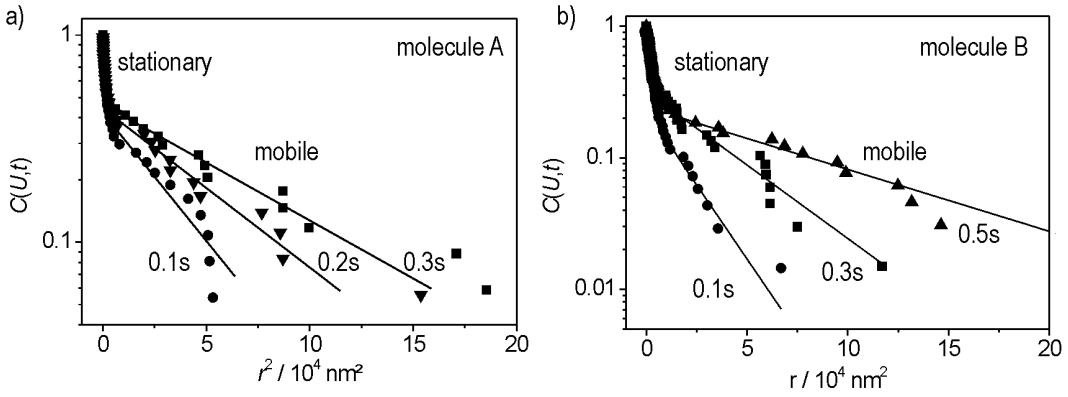

Figure 70: Two trajectories of 9A1 diffusing in M3 show a pronounced heterogenous behaviour due to a trapping region. The population analysis allows a separation between the fast and slow parts of the trajectory (for details cf. text)

The distribution in both cases clearly show the presence of two diffusional components. The ranked squared steps - corresponding to $C(U,t)$; equation 14b below - are fitted to a biexponential decay, yielding two values for the mean square displacements, which can be plotted as a function of time and analysed according to appropriate diffusion models. The underlying equations in question are - adapted from eqns 12, 13 and 14 with $m = 2$:

$$p(u,t) = \left[\frac{A_1}{\left\langle r_1^2(t) \right\rangle} \exp\left(\frac{-u}{\left\langle r_1^2(t) \right\rangle} \right) + \frac{A_2}{\left\langle r_2^2(t) \right\rangle} \exp\left(\frac{-u}{\left\langle r_2^2(t) \right\rangle} \right) \right] \qquad (12b)$$

$$P(U,t) = \int_0^U p(u,t)\, \mathrm{d}u = 1 - \left[A_1 \exp\left(\frac{-U}{\left\langle r_1^2(t) \right\rangle} \right) + A_2 \exp\left(\frac{-U}{\left\langle r_2^2(t) \right\rangle} \right) \right] \qquad (13b)$$

$$C(U,t) = 1 - P(U,t) = A_1 \exp\left(\frac{-U}{\left\langle r_1^2(t) \right\rangle} \right) + A_2 \exp\left(\frac{-U}{\left\langle r_2^2(t) \right\rangle} \right) \qquad (14b)$$

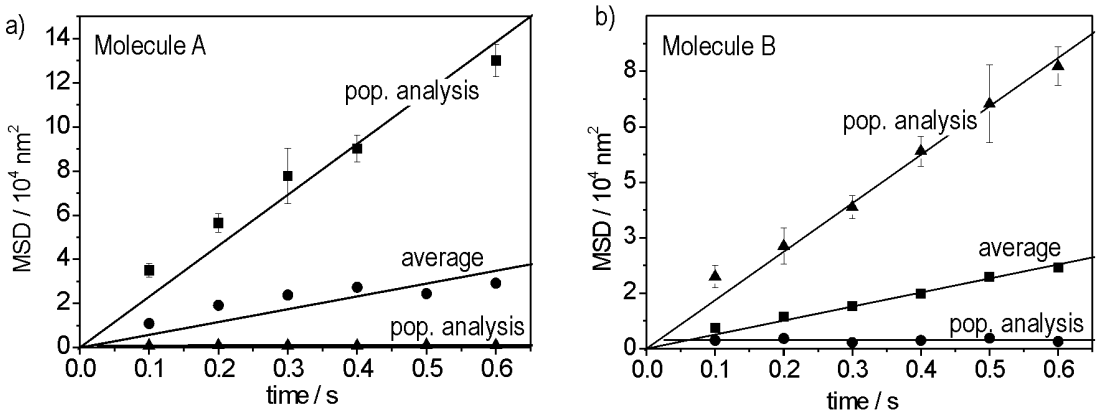

Figure 71: The mean squared displacements for the two populations obtained from the population analysis are plotted versus time for molecules A and B. The simple average calculated over the entire trajectory gives a value that lies between the two populations, but has no physical meaning.

A linear regression through the data for the mobile part, assuming the simplest model of diffusion in this case, gives the diffusion coefficients $D_{MA} = 5.8 \pm 0.5 \cdot 10^{-10}$ cm^2s^{-1} and $D_{MB} = 3.3 \pm 0.3 \cdot 10^{-10}$ cm^2s^{-1} respectively for the mobile part of the trajectories of molecules A and B. The immobile or slow components have in both cases a constant value of approximately 2500 nm^2. These values are comparable to what would result from an artificial jittering movement caused by the positioning inaccuracy of ca. 50 nm (resulting in an effective confinement of 2500 nm^2), therefore the trap size has an effective diameter below 50 nm. It is not possible, however, to decide directly whether the molecules are immobile on a mlecular scale, e.g. specific adsorbtion to silanol groups of the pore walls (as proposed for example by [Wirth98]), or if they are incorporated into a spatial confinement via a bottle-neck opening. This question will be addressed again in more detail below in the discussion of the immobile or confined trajectories.

Analysis of Individual Trajectories in M22: The trajectories in M22 appear to be significantly more homogenous. Traps similar as to the ones observed in M3 are not observed. The analysis of an exemplary trajectory is shown in fig.72.

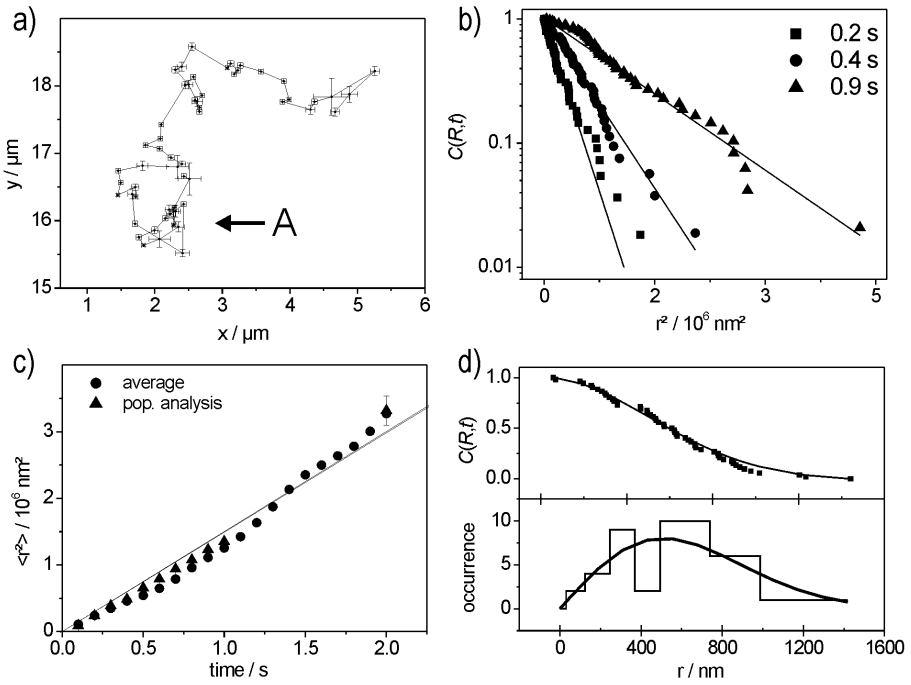

Figure 72: Evaluation of a 9A1 trajectory in M22 sol-gel-glass (a) Trajectory. (b) The population analysis based on the cumulative probability for different times. (c) The mean squared displacements versus time plots, averaged from the individual steps (circles) and obtained from the population analysis (triangles) coincide. The diffusion coefficient for this trajectory is $D = 3.7 \pm 0.5 \cdot 10^{-9}$ cm^2s^{-1} according to a random walk in 2D. (d) The step length distribution for δt = 100 ms (lower graph) is obtained via a population analysis of step lengths (upper graph) has a maximum at 508 ± 16 nm.

In fig. 72 a) the trajectory shows a region (marked A) that might be interpreted as a local heterogeneity. The behaviour in this region, however, does not deviate from what would be expected from a normal isotropic random walk. The ranked squared displacements (fig.72b) show a unimodal distribution, and the use of an additional population in the

analysis is not justified by the data. The mean squared displacements obtained via population analysis and by computing the simple average coincide in the MSD versus time plot (fig. 72c). Any heterogeneity (such as the marked region in the trajectory) that might be present in the trajectory is not statistically significant, and cannot be distinguished from the remaining data. A linear regression through the data in figure 72c gives a diffusion coefficient of $D = 3.7 \pm 0.5 \cdot 10^{-9}$ cm^2s^{-1} according to the model of a two-dimensional isotropic random walk.

The step length distribution (lower graph in fig.72d) can be obtained in a similar way via population analysis. The complementary cumulative probability distribution $C(R,t)$ of step lengths, shown in the upper graph of figure 66d is obtained by ranking the experimentally found data. This data is fitted by:

$$C(R,t) = 1 - P(R,t) = 1 - \int_0^R q(r,t)\, dr = \exp\left(\frac{-R^2}{\left\langle r_i^2(t)\right\rangle}\right), \qquad (17b)$$

which in turn is obtained from equations 15, 16 and 17 using $m = 1$ (one population). The characteristic value $\langle r_i^2(t)\rangle$ is obtained by fitting the ranked data to $C(R,t)$. For consecutive steps (that is $\delta t = 100$ ms) $\langle r_i^2\rangle = 584 \pm 7$ nm^2. The smooth curve enveloping the histogramme of step lengths shown in figure 72d (lower graph) is obtained by using $\langle r_i^2\rangle$ in equation 15 with m=1:

$$q(r,1) = \frac{2r}{\left\langle r_i^2\right\rangle} \exp(-r^2/\langle r_i^2\rangle). \qquad (15b)$$

Note that the maximum of the histogramme does not correspond to $(\langle r_i^2\rangle)^{0.5}$. The maximum, or the most frequent step sizes found in this trajectory, is at 508 ± 16 nm.

Confined trajectories: One question left open in the evaluation of the trajectories so far, is whether the confined trajectories, or the parts of the trajectories in which the molecules seem to be immobilized are (a) due to an interaction of the molecule with the matrix (fig.73a), (b) due to a molecule situated in a (sizeable) geometrical confinement in which it may move, but from which it cannot escape (fig. 73b), or (c) due to bottleneck-traps into which a molecule may diffuse and eventually escape (fig. 73c).

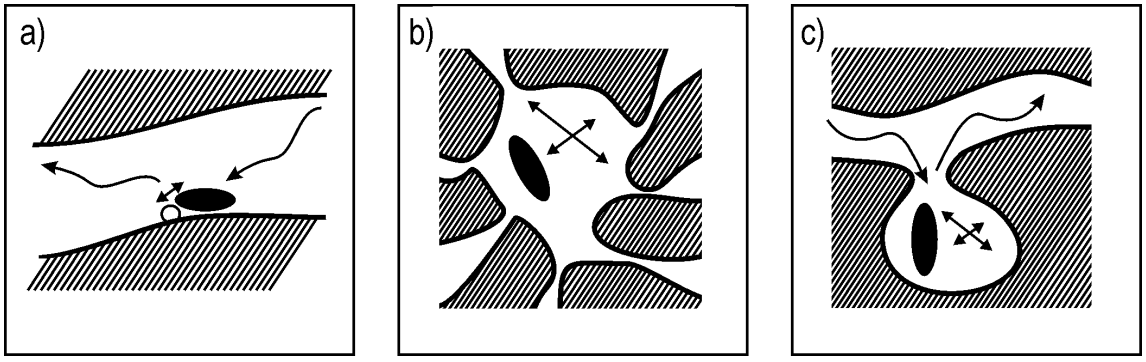

Figure 73: Schematical showing possible mechanisms leading to a confined trajectory: a) A molecule may become immobilized on a small scale of length if it interacts with an adsorption site on the walls of the porous matrix. b) It may be encapsulated or sealed-off within a small cage formed during synthesis. c) A molecule may enter a cavity through a small opening, remain trapped (bottle-neck trap) and eventually escape the confinement.

The trajectories of 9A1 that become interrupted by a confinement region, could in principle be interpreted according to (a). Such cases, however, were not detected in the case of 9A1 diffusing in M22. Observation of case (a) should be independent from the pore-size of the material, since the chemical composition of the pore walls in M3 and M22 is similar. If such a process takes place, then it occurrs at a shorter time scale (<40 ms), presently not accessible to the microscopy apparatus. In cases (b) and (c) it should be possible to detect the mobility of a molecule in the cage, if it is larger than the positioning accuracy. In this case it should be possible to determine the effective size of the confinement.

We turn now to the analysis of the confined trajectories. Two extreme cases of such trajectories will be discussed in the following: (a) A molecule that seems to be confined on a region smaller than the positioning accuracy (≈ 50 nm) and (b) a molecule that is clearly situated in a confinement of measurable size. Fig. 74 a) and b) show the trajectories of the two molecules (δt = 100 ms).

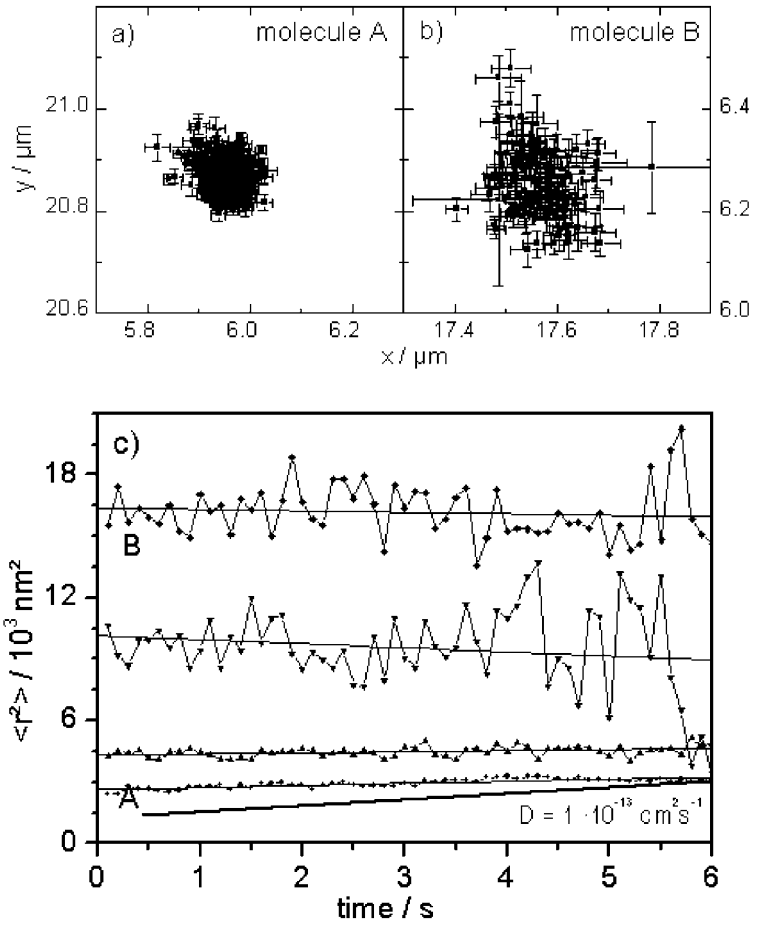

Figure 74: Analysis of confined trajectories. a) and b) show two extreme cases, respectively, of a trajectory confined to a region smaller than the positioning accuracy, and a trajectory confined to a region that is visibly larger than the positioning accuracy. c) Shows the MSD versus time plot of four confined trajectories. Molecules A and B are the two extreme cases in this plot. (The line on the bottom shows the MSD vs t curve for D=10^{-12} cm^2s^{-1}, the smallest detectable diffusion coefficient)

Both trajectories can be analysed according to a confined motion model. The expression for a two-dimensional random walk in a confinement (eq.19, section 2.3.2.) is:

$$\left\langle r^2(t)\right\rangle \cong \left\langle r_C^2\right\rangle \left[1 - A_1 \exp\left(\frac{-4A_2}{\left\langle r_C^2\right\rangle} Dt\right)\right] \qquad (19)$$

In this equation the mean square displacement reaches an asymptotic value of $\langle r_c^2 \rangle$ for long obeservation times. This value corresponds to the effective confinement area. The diffusion coefficient D can be obtained if the ascending component (the exponential term in eq. 19) is availiable from the data - this is not the case here (fig. 68c), the confinement region is completely explored by the molecules within 100 ms. The values for $\langle r_c^2 \rangle$, however, are readily obtained from the experimental data. The confinement area for molecule A and B are $\langle r_c^2 \rangle_A = 2500$ nm^2 and $\langle r_c^2 \rangle_B = 16500$ nm^2 respectively (D is therefore larger than $1.65 \cdot 10^{-9}$ cm^{2}s^{-1} in the case of molecule B). The effective confinement diameter $d_C = 2 \cdot [\langle r_c^2 \rangle \pi^{-1}]^{0.5}$ is 56 nm and 144 nm for molecules A and B. The mean positioning accuracy in both cases is $\langle dr_A \rangle = 40$ nm and $\langle dr_B \rangle = 57$ nm. In the case of molecule B the confinement region exceeds the positioning accuracy by a factor ~3 - in this case it is clear that the molecule is moving in a sizeable confined region. The case is not so clear-cut for molecule A, where the confinement size is similar to the positioning accuracy. In this case it is not possible to determine whether the molecule is genuinely immobile or if it is moving in a small confinement with a diameter <50 nm.

Summary and Conclusion: The decreasing porosity of a sol-gel material leads to a reduction of the overall diffusivity. This reduction of the overall diffusivity can be attributed (a) to the increasing frequency of the pore-molecule interactions on going to the material with the smaller porosity and (b) to the presence of 'bottleneck-traps', which are more likely to occur in a material with smaller pores.

The diffusion of 9A1 in the sample with the wider pores M22 can be described by a normal diffusion model with an effective diffusion coefficient of $D_{eff} = 4.7 \cdot 10^{-9}$ cm^{2}s^{-1}.

The individual diffusional behaviors of the molecules are distributed around this mean value (see fig. 75a). In M22 a sub-population of non-diffusing molecules (ca. 20%) is found to coexist in the sample. The diffusion of 9A1 in M3 is more heterogenous than in M22 (see fig. 75b). The reduction of the $D_{eff} = 3.5 \cdot 10^{-10}$ cm^2s^{-1} by one order of magnitude is accompanied by an anomalous behaviour found in many trajectories. In such cases 9A1 molecule become trapped and are subsequently released. A more pronounced population of confined molecules (80%) is observed in this sample.

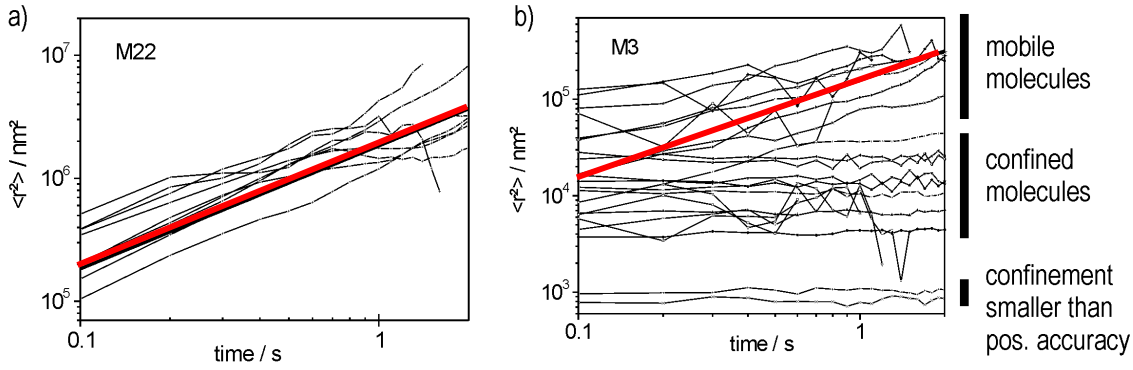

Figure 75: Diffusion in M22 (a) is more homogenous than in M3 (b). The red line in both graphs indicates the average MSD versus time curve.

While the characterization of diffusion on the basis of individual trajectories allows for a very thorough characterization of the diffusional behaviour, there are still a few questions that remain open and that could be adressed in the near future.(a) Is there a more direct way to prove if the molecules trapped in the small voids are genuinely immobile? This could for example be answered by looking at the orientational behaviour of the confined molecules. If the molecules are jittering in an area (of a few nm in size) instead of being adsorbed, then some form of orientational diffusion should be observed. (b) Are the confined regions truely sealed off? There is good reason to assume that the observed confinements are accessible via micropores. Smaller solvent molecules could therefore reach the dyes in these confinements. To analyse this, one possibility would be to monitor the spectra of confined molecules which may vary if different solvents reach the cage.

4.6. Translational Diffusion of TDI Molecules in SBA-15 Films

Introduction: The particle tracking method in combination with widefield microscopy proved to be the method of choice for the characterization of molecular diffusion in mesoporous materials. In a second study, this appraoch was used to readdress the question of diffusion in a structured mesoporous material with unidimensional pores, like the MCM-41 material. In this study TDI (fig. 76a) was incorporated into the channels of a spin-coated SBA-15 film (see fig.76c and 76d), which has hexagonally arranged unidimensional cylindrical pores - very simialr to MCM-41 (cf. section 4.4.).

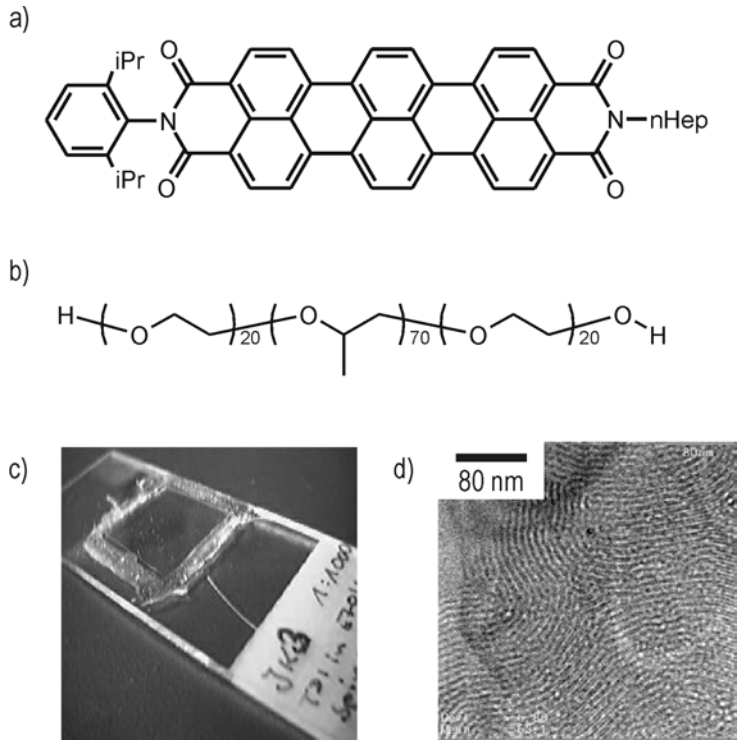

Figure 76: TDI in SBA-15 films. a) Structural formula of TDI. b) Structural formula of the template Pluronic P123. c) General appearance of a spin coated SBA-15 film d) TEM images of a thinned SBA-15 sample showing the pores arranged in (fingerprint) domains

The SBA-15 material is synthesized (in the group of Prof. Dr. Thomas Bein, LMU) using P123 (a block co-polymer, fig. 76) as a supramolecular template for the formation of the unidimensional channels. TDI is added during synthesis at a concentration of ca. 10^{-9} M,

and the material is left uncalcined. The diameter of the hexagonally arranged cylindrical pores can be estimated from XRD data and are between 6 and 7 nm. TEM images of materials synthesized under identical conditions show that the pores are organized in domains, in which the pores lie parallel to the surface of the substrate (the microscopy cover-slide). The size of these domains are in the order of a few hundred nanometers (fig. 76d).

The main advantage of the spin-coated material over the monolithic material discussed in the previous study, is that the out-of-plane diffusion of the molecules is suppressed, because the thickness of the spin-coated films is considerably smaller than the focal depth of the microscopy apparatus (100-200 nm film thickness versus 3 µm focal depth). Trajectories can thus be observed over a longer period of time, allowing for a significant improvement in the statistical quality of the data.

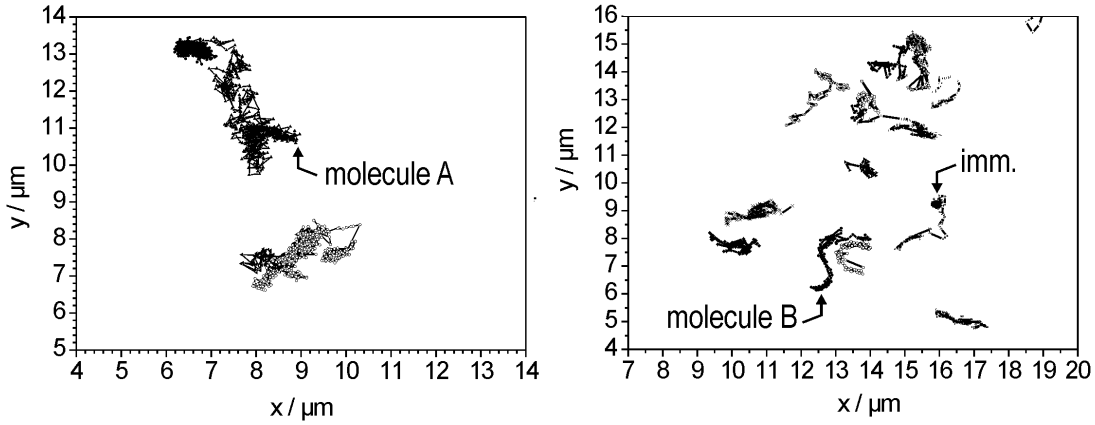

Fig 77: Trajectory map obtained from different sequences of images on different regions of the the same sample. The two trajectories of molecule A and molecule B are discussed in more detail.

Microscopy image sequences show the individual diffraction limited patterns, from the individual TDI molecules, which are mobile. The trajectories are obtained by tracking the emission patterns in a sequence of images, like shown before for 9A1 diffusing in the sol-gel-glass. The average positioning accuracy in this case is 30 nm, typical acquisition

times lie between 40 ms and 100 ms depending on the quality of the sample. Two sets of trajectories are shown as an overview map in figure 77. A quick characterization of the diffusion on a global level, that is, estimating an effective diffusion coefficient from all mobile trajectories assuming a 2D random walk, gives an effective diffusion coefficient of $D_{\text{eff}} = 4.4 \cdot 10^{-10}$ cm^{2}s^{-1}. This value, however, only describes a fictitious average behavior. Most of the trajectories in these maps show particularly pronounced structural features. The analysis of individual trajectories, carried out here on two exemplary trajectories (figure 78), reveals (a) details that are not sensed by other techniques used to characterize diffusion and (b) that the simple model of a 2D random walk is not describing the data well.

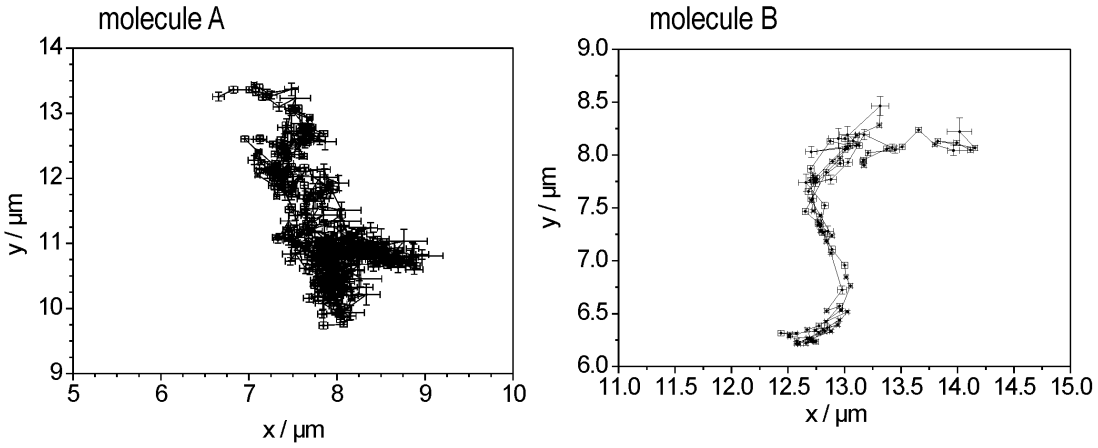

Fig 78: Two trajectories of TDI diffusing in SBA-15 films. The trajectory of molecule A shows regions in which the molecule appears to remain for a longer time, and regions in which the molecule appears to be moving faster. The trajectory of molecule B is visibly structured.

Step-size distribution: The trajectories of the two molecules are first analysed in order to obtain the step-size distributions between successive frames. As described in section 2.3.2. the individual step lengths are sorted and assigned a relative rank *j/N*. The plot of *j*/*N* versus step length corresponds to the complementary cumulative probability $C(R,t)$ (equation 18 - given below, cf. also section 2.3.2)

$$C(R,t) = 1 - P(R,t) = \int_0^R q(r,t)\,\mathrm{d}r = \sum_{i=1}^{m} A_i \exp\left(\frac{-R^2}{\left\langle r_i^2(t)\right\rangle}\right). \qquad (18)$$

$C(R,t)$ which is a Gaussian or a sum of Gaussians centered at origin, depending if different distinguishable sub-populations of step sizes are present in the data. The curves for the two trajectories are shown in figure 79. The results of the fitting procedure are resumed in the table given below.

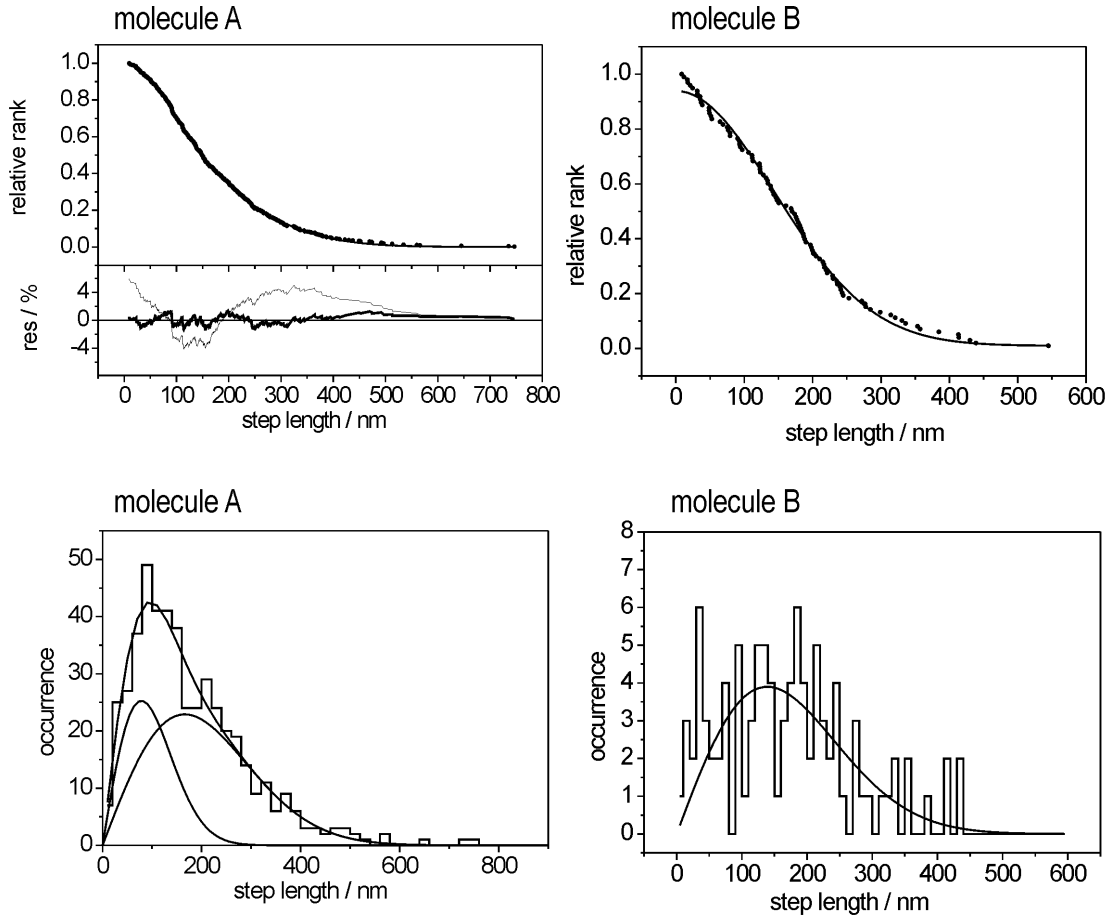

Figure 79: Step length distribution for the trajectories of molecules A and B (N = 482 and N=97, respectively). Below the histogrammes and the corresponding envelope curves are shown for the two trajectories.

	molecule A	molecule B
δt	42 ms	78 ms
m	2	1
N	482	97
$\langle r_1^2 \rangle$	27600 ± 1000 nm^2	67600 ± 5000 nm^2
$\langle r_2^2 \rangle$	121100 ± 2000 nm^2	-
$r_{max,\,1}$	83 ± 10 nm	143 ± 20 nm
$r_{max,\,2}$	174 ± 10 nm	-

In the case of molecule A the distribution points to the presence of two distinguishable sub-populations of step lengths. These two populations of step lengths in the case of molecule A are not spatially separated, the longer steps occur on the entire trajectory (fig.80). This molecule alternates between fast and slow steps throughout the trajectory.

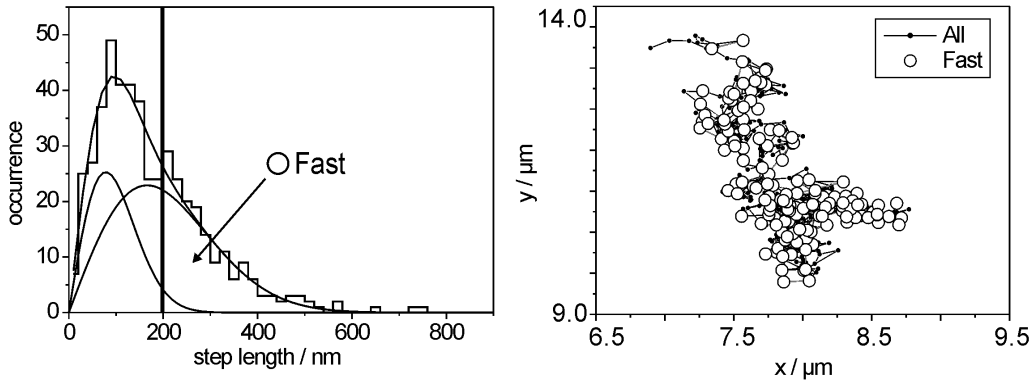

Figure 80: Distribution of fast steps in the entire trajectory. The steps contributing to the fast population in the histogram are highlighted in the trajectory to the right.

The trajectory of molecule B shows one population of step lengths. The smooth distribution curves (plotted in the lower graphs of fig. 73) are obtained using the $\langle r_i^2 \rangle$ found via fitting. The curves envelope the histogrammes obtained in a conventional way (via data binning).

Mean squared displacements / MSD versus time: The mean squared displacements MSD for different times are obtained from a population analysis. The MSDs are plotted versus time for molecule A and molecule B in figure 81. A linear regression through the data, assuming $\langle r^2(t) \rangle = 4\, D \cdot t$, gives an effective diffusion coefficients for molecule A and B respectively: $D_{A,E} = 5.6 \cdot 10^{-10}$ cm^{2}s^{-1} and $D_{B,E} = 2.1 \cdot 10^{-9}$ cm^{2}s^{-1}. Note, however, that this diffusion model is *not* justified, despite the fair agreement with the data: (a) molecule A shows sub-populations of slow and fast steps; and (b) the trajectory of molecule B does not appear to be isotropic.

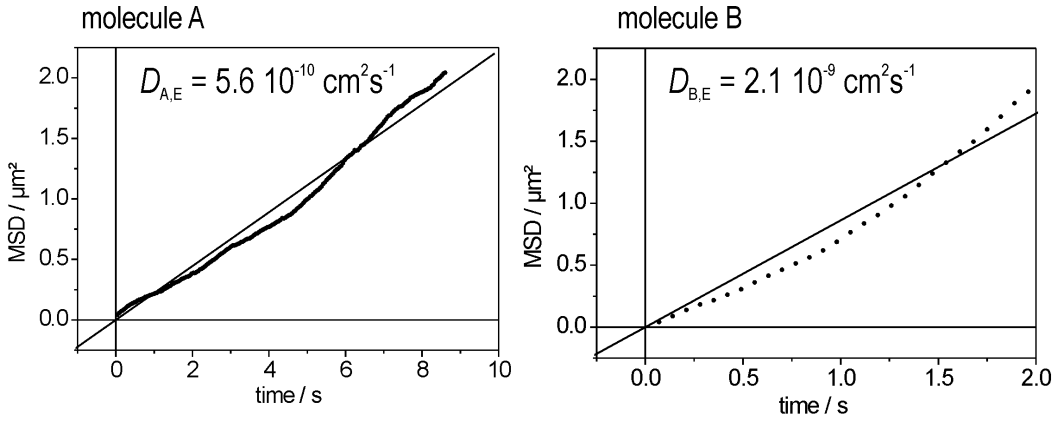

Figure 81: MSD versus time plots for molecule A and B.

Angles between steps: The angles between successive steps can be used to check whether the trajectories show directional anisotropies. (*Note:* Step angles are defined as 0° for two consecutive steps in the same direction, ±180° for a forward step followed by a backward step, and negative angles in counter-clockwise direction.) The parameters inferred so far, the trajectory themselves, the step-length distributions and the MSD versus time behaviour, pointing to a deviation from the isotropic random walk model, but are not clearly convincing. The histogram of step angles for the two trajectories, shown in figure 82, is very clearly showing that the trajectories cannot be described by isotropic motion models.

Backward steps (±180°) are clearly overrepresented in the trajectory of molecule A. In the case of molecule B, a significant population is found at 0° and ±180°, indicating that

the molecule is predominatly moving forward and backward. Significantly fewer steps have an angle of ±90° in this trajectory. In this case the trajectory bears more similarity to an unidimensional random walk along a tortuous channel than with an isotropic two-dimensional one. The trajectory reflects a real structural feature within the host material (a bundle of curved channels, for example).

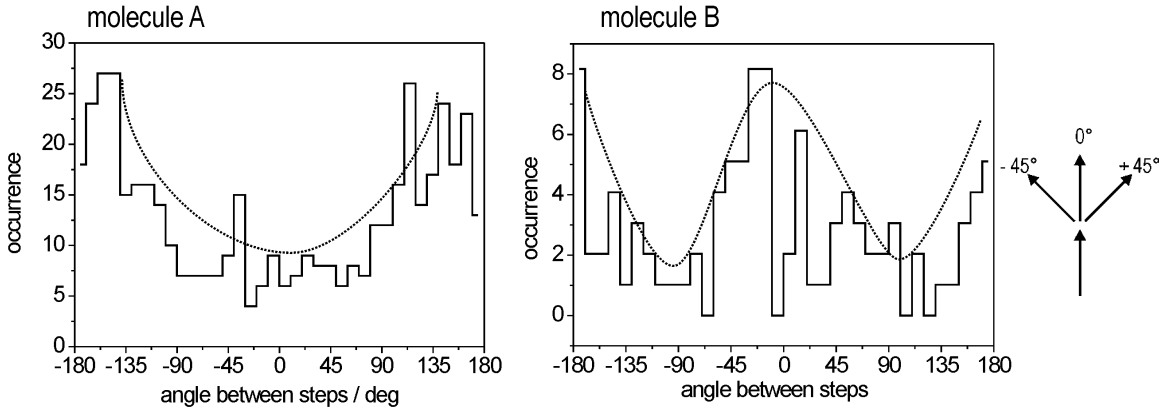

Figure 82: Histograms (bin = 10°) for the angles between successive steps in the trajectories of molecules A and B.

Outlook: The analysis of the trajectories from individual molecules allows for a very thorough characterization of the diffusional behaviour, as details of the diffusion processes become revealed. While a wealth of information can be gained from the trajectories, on the other hand the interpretation becomes more complex, as many details remain unknown. (a) The underlying structure of the host matrix, for example, is an important unknown factor: What structural feature of the host is being mapped by the tortuous trajectory? Domain boundaries? Tortuous channels? One possibility to clarify this would be to superimpose TEM images with the trajectories, recorded in the same area of the sample. (b) Is there a more direct proof showing that the molecules are diffusing in comparatively narrow cylindrical pores? This could for example be answered by looking simultaneously at the diffusional and orientational behavior. (c) What causes a molecule to predominatly move backward? TDI is an asymmetric molecule with a flexible *n*-heptyl tail, which could be giving rise to a preponderance of backward steps. Simulations and measurements on symmetric TDI derivatives could provide the necessary information for a more complete understanding of this observation.

4.7. Spectral Behavior of TDI in PMMA

Introduction: Spectral dynamics, like shifts and jumps of the emission maximum of fluorescence, is a commonly observed phenomenon in single molecule spectroscopy (SMS). [Kettner97], [Lu97], [Tamarat00], [Weber00], [Hou00], [Köhn00], [Hofkens01], [Kiraz03], [Stracke04]. This dynamic behaviour originates from fluctuations in the energy landscape of the molecule, which, in turn, depend on the structure of the molecule (*intrinsic effects*) and the influences of the molecule's immediate surroundings (*extrinsic effects*). The magnitude of the fluctuation and the time-scale on which it occurs depend on what kind of interaction the molecule experiences from its surroundings. In a simple schematical picture the fluctuations of the shapes and positions of the involved quantum-mechanical potential curves of the S_0 and S_1 states (plus vibronic levels) is what finally leads to different spectra (adapted from [Blum01]):

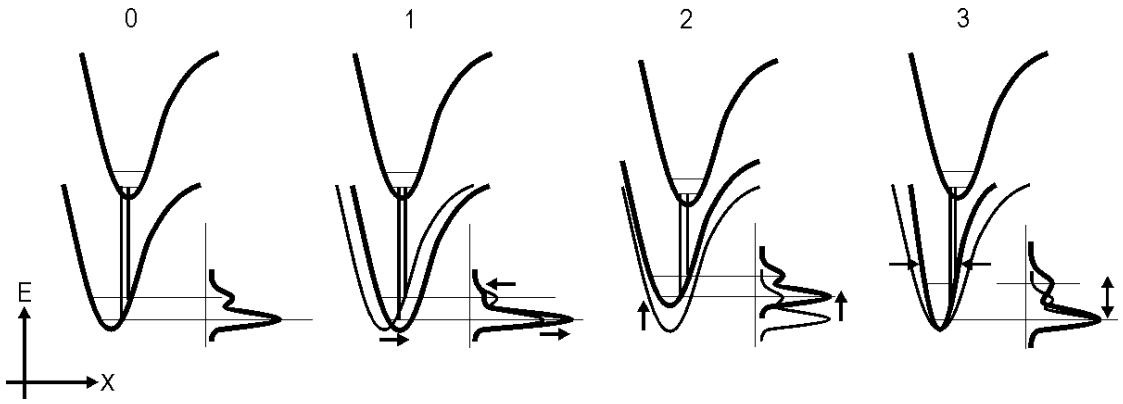

Figure 83: The schematical energy-diagram of a S_1-S_0 transition illustrates how a relative modification of the ground state potential gives rise to different emission spectra.

Starting from a given standard configuration (case 0 in fig. 83) a lateral movement of the ground state potential (case 1) changes the probabilities with which the electronic relaxations occur to the vibrational states, because the Franck-Condon factors change. In the emission spectrum this is visualized as a modified intensity ratio between the 00 band and the respective vibronic band(s). A vertical shift of the S_0 potential (case 2) leads to an overall shift of the entire spectrum (in the depicted example to lower energies). A

modification of the potential curve (case 3), which can be related to a deformation of the molecule's structure (e.g. bending or twisting), may lead to different vibronic progressions. In the depicted example a narrower shape of the potential is visible as a stretching of the spectrum. Cases 1 and 2 have been observed and described in literature [Stracke04], [Seebacher02d], [Blum01]. A direct observation of case (3) has not yet been described in literature.

Many mechanisms on the molecular level can lead to these different situations. One example is the possible distortion of the molecule's structure due to steric interactions of the molecule with the surrounding matrix. [Hou00] Another example is the chemical influence of the environment (like polar interactions, protonation, formation of contact ion pairs) leading to a stabilization or destabilization of the ground state.[Köhn00] In low-temperature SMS experiments the spectral shifts (from a few GHz down to a few 100 MHz) are usually attributed to thermal fluctuations in the immediate vicinity of the molecule or phonon assisted tunneling [Fleury93], for example in a polymer matrix [Kiraz03], [Kiraz05a], in *p*-Terphenyl crystals [Kulzer97], or in a Shpolskii-matrix [Orrit90]. At room-temperature, it was possible to identify different, interconvertible conformers of one dye as being responsible for the occurring spectral jumps.[Blum01] In one other case an observed spectral jump has been attributed to an epoxidation product of the perrylen dye used.[Christ01] Studies like these, in which the origin of the spectral fluctuation is revealed are rare, and usually not inferred solely by SMS methods. Often such observations must be supported by simulations and quantum mechanical *ab initio* calculations.[Hofkens01], [Bordat02]

Spectral dynamics occur on all time-scales and most authors differentiate between two types of dynamics: First, the most frequent random fluctuations around a mean value, which are often termed *spectral diffusion*. And second, discrete or abrupt changes of spectral properties, which are called *spectral jumps*. It is often difficult to differentiate exactly between these two types of spectral dynamics, because it depends on the time-scale of the observation, and because the exact meachnisms responsible for the fluctuations are not completely elucidated.

Spectral behavior of TDI in PMMA: Ten-thousands of spectra could be acquired for many different individual molecules in a TDI/PMMA sample, with a temporal resolution of 34 ms, allowing for a well-resolved statistical analysis. The possibility to record these amounts of spectra and an evaluation combining multiple parameters have been presented in [Seebacher02d]. The analysis of these spectra in terms of populations, on the individual and global level, and finally the characterization of the involved spectral dynamics will be laid out here.

The individual spectra of TDI molecules in PMMA at room temperature resemble the ensemble spectrum (see fig. 84) with a pronounced 00 band (emission maximum around 690 nm) and a well-resolved, vibrational band (which is red-shifted by ca. 60 nm). The main band also shows a vibronic shoulder hidden under the main band (ca. 20 nm red-shift), giving it an overall asymmetric appearance. While this shoulder is not further analysed, it is used in the analysis as a constant asymmetry of the main band.

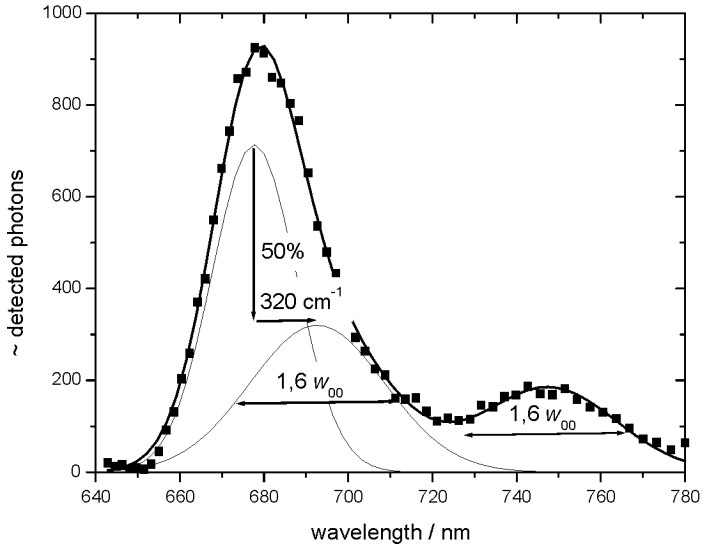

Figure 84: Spectrum of an individual TDI molecule in PMMA at room temperature (acquisition time δt =34 ms). The spectrum shows two pronounced bands (00 and vibronic) as well as a shoulder hidden in the main 00 band (adapted from [Seebacher02d]).

The individual TDI spectra are well-described by a triple Gaussian with five free parameters (equation 41, see also fig.77):

$$I(\lambda) = I_{00}\exp\left(\frac{-(\lambda-\lambda_{00})^2}{2w_0^2}\right) + \frac{I_{00}}{2}\exp\left(\frac{-(\lambda-\lambda_1)^2}{3.2w_0^2}\right) + I_{vib}\exp\left(\frac{-(\lambda-\lambda_{vib})^2}{3.2w_0^2}\right) \qquad (41)$$

In this equation the central position of the main band is λ_{00} in nm, its amplitude I_{00} (in arbitrary units), the position and the amplitude of the well-resolved vibronic band are λ_{vib} and I_{vib} and an overall width parameter is w_0. λ_1 is a fixed parameter for the shoulder corresponding to a shift of 320 cm^{-1} from the 00 band (cf. fig. 84). The parameters obtained by fitting a sequence of spectra to the triple-gaussian model above (eq.41) are evaluated to characterize spectral dynamics, and spectral populations. All spectral positions will be henceforth noted ν and given in units of wavenumbers (cm^{-1}) to allow for a linear scaling with energy.

Spectral populations: The first observation, which, as noted before, is common in SMS, is that the spectra show a noticeable dynamic behavior: The spectrum fluctuates (*spectral diffusion*) around a mean value in a noise-like way:

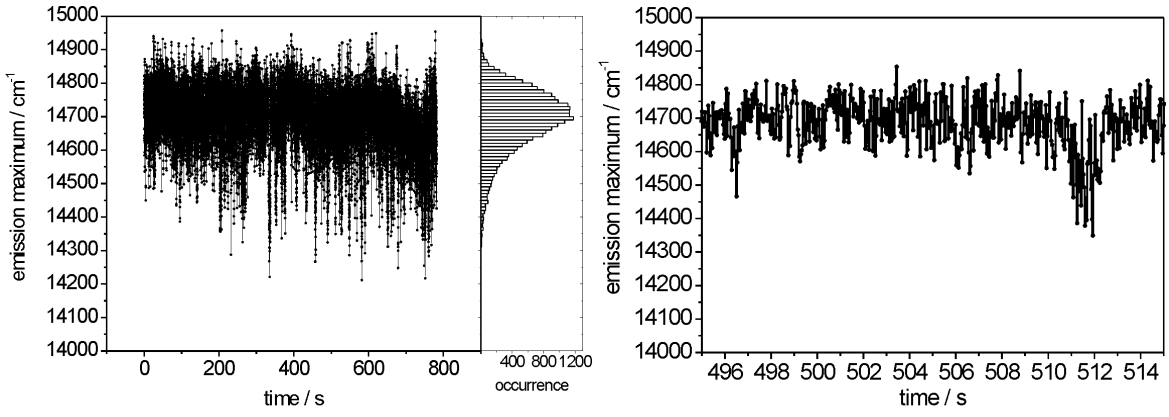

Figure 85: Emission amximum versus time for an individual TDI molecule in PMMA (~23.000 spectra; δt = 34 ms) and histogram. The right graph shows an excerpt of the complete time-trace.

First the distribution of the found spectral parameters is analysed. The histograms for the individual parameters are given in figure 86 for an exemplary sequence of 18000 spectra acquired for one TDI molecule in PMMA and with a time resolution of 34 ms. In fig. 86 the histograms for the intensity ratio (I_{vib}:I_{00}, 86a), the spectral distance (ν_{vib} - ν_{00}, 86b) and emission maximum (ν_{00}, 86c), are given. The histograms show a bell shaped distribution for the parameters. The absence of pronounced additional peaks indicates that there are no clearly distinguishable sub-populations in the distribution of the spectral parameters.

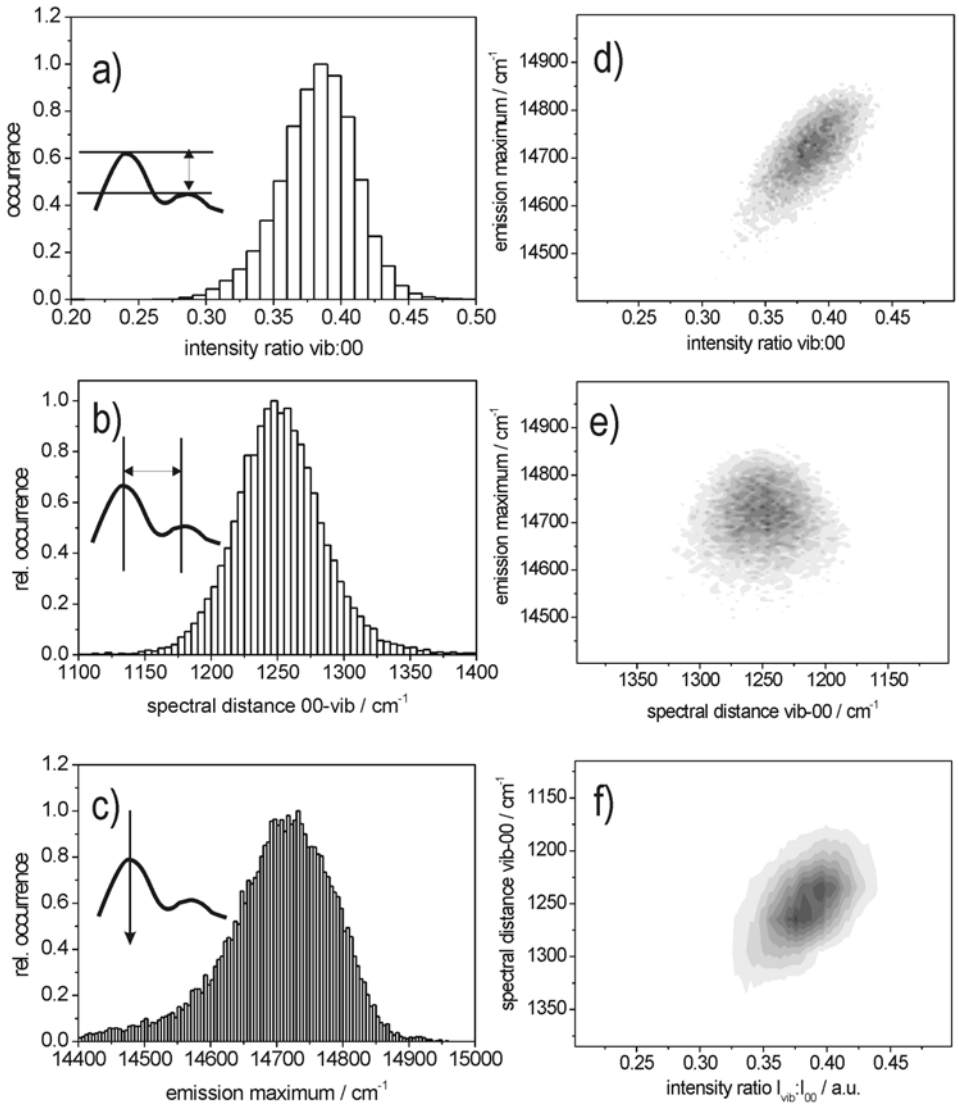

Figure 86: 1D and 2D histograms of spectral parameters.

Two-dimensional histograms can be obtained by correlating the parameters, as shown exemplarily in figure 86d for emission maximum (ν_{max}) versus intensity ratio (I_{vib}:I_{00}), in 86e for emission maximum (ν_{max}) versus spectral distance (ν_{00} - ν_{vib}) and in 86f for spectral distance (ν_{00} - ν_{vib}) versus intensity ratio (I_{vib}:I_{00}).

The distribution of spectra in a two-dimensional histogramme is shown more clearly in figure 87. Here, two extreme spectra (A and B) in the distribution are superimposed at the normalized emission maximum. The spectrum of this TDI molecule diffuses between these two extremes. In this particular case case it is also possible to observe a case of spectral stretching (case 3 in figure 83).

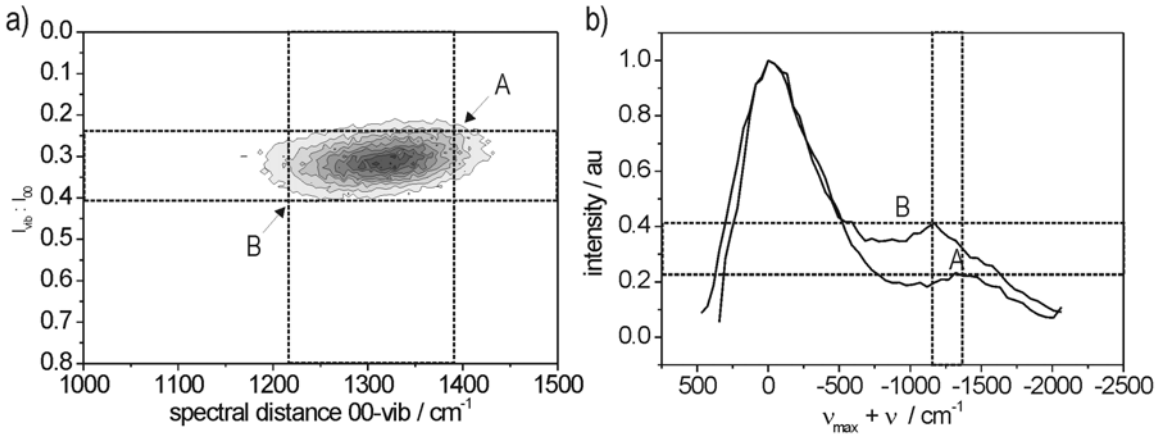

Figure 87: Two dimensional histogram of intensity ratio (I_{vib}:I_{00}) versus spectral distance (ν_{vib}-ν_{00}). In the right graph the spectra of the extreme cases (A and B) from this distribution are shown.

Spectral sub-populations: The next observation is that the distributions of spectral properties of an individual molecule may also show distingishable sub-populations, between which the molecule switches abruptly (*spectral jumps*). It is particularly interesting to emphasize that certain sub-populations only become clearly visible in the two-dimensional histograms, as they would otherwise be hidden in the conventional histograms.For example, it is possible to identify five distinguishable sub populations in the 2D-histogram shown in figure 88. Note that the simple histograms only show three clear peaks. A clear example of a hidden sub-population is sub-population 3 in fig. 88

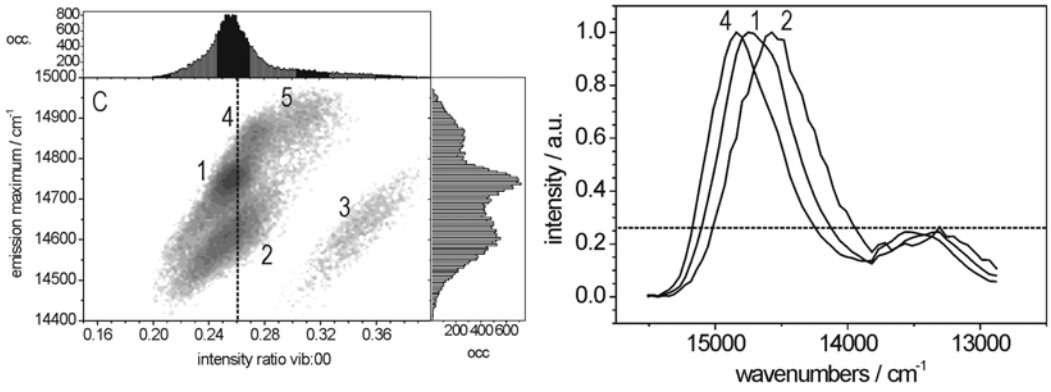

Figure 88: The two dimensional histogram or emission maximum versus intensity ratio alolows tro distinguish between sub-populations that would otherwise be hidden in the unidimensional histogram (e.g. sub-population 3). The right graph shows three spectra that can be assigned to sub-populations 4, 1 and 2.

Dynamics of spectral diffusion: The next question addresses the dynamics of spectral diffusion. How fast do the properties of the spectra diffuse within the entire distribution?

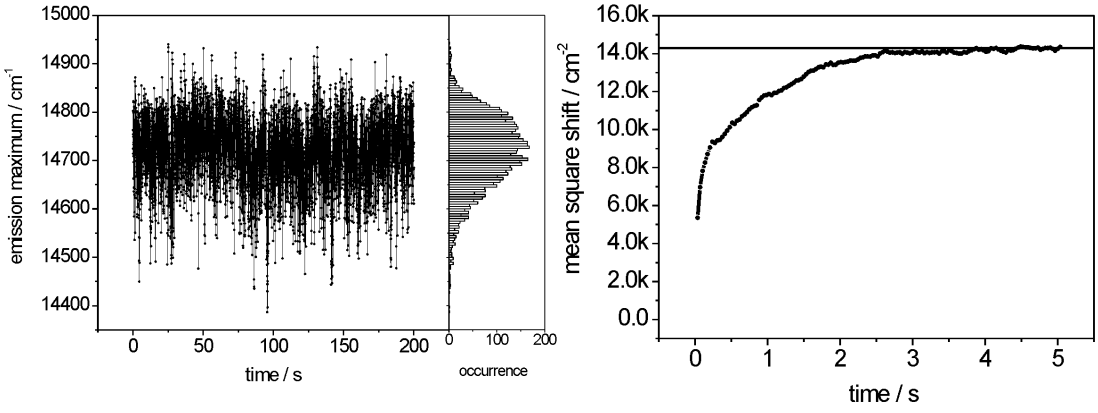

Figure 89: Characterization of spectral diffusion. *left:* The fluctuating emission maximum of an individual TDI molecule in PMMA is plotted versus time. *Right:* The mean square shift is plotted versus observation time

This question can be adressed in a similar way to that discussed for the translational motion of a particle in a confinement. If the spectrum is confined to a certain spectral region the mean squared spectral shift is expected to reach an asymptotic value in dependence of the observation time.[Kiraz05]. The analysis of the fluctuation dynamics shows the expected asymptotic behaviour. This is shown here for the diffusion of the spectral maximum with time. In figure 89 the emission maximum is plotted versus time. The squared shifts are then computed for all steps separated by 1,2,3,... time lags and the mean value is determined. The obtained mean squared shifts are then plotted versus observation time (right graph in figure 89). The value for the mean squared shift increases with time reaching an asymptotic value after ca. 3 s. Spectra acquired with an integration time >3s will not show spectral diffusion unless a slower spectral diffusion process to other spectral regions occurs (i.e. spectral jumps, cf. later). The square of the asymptotic value describes the width of the effective, spectral confinement region, which in the case of the exemplary molecule in figure 89 is in the order of 120 cm^{-1}.

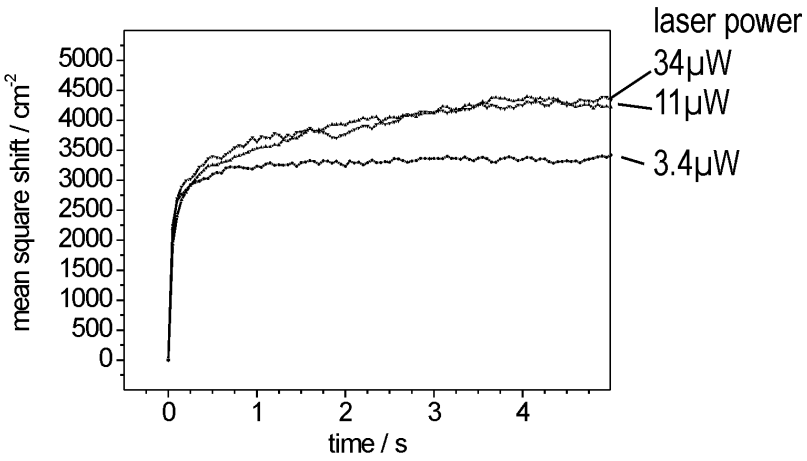

Figure 90: Measurement of the spectral diffusion in dependence of the excitation power.

The same kind of data can be acquired in dependence of the excitation power (fig. 90). The asymptotic value in this example reached rapidly (<1 s) using low excitation power (3.4 µW; asymptote at ca. 3100 cm^{-2}). Higher excitation power (11 µW, 34µW) increases the accessible spectral confinement region (4300 cm^{-2}). The spectra reach the higher asymptote after a comparatively longer time of ca. 3 s.

Dynamics of spectral jumps: The dynamic behaviour of jumps between the sub-populations can also be analysed, by assigning each spectrum to a population which are visible as 'clouds' in a two-dimensional histogramme (as shown in fig. 91).

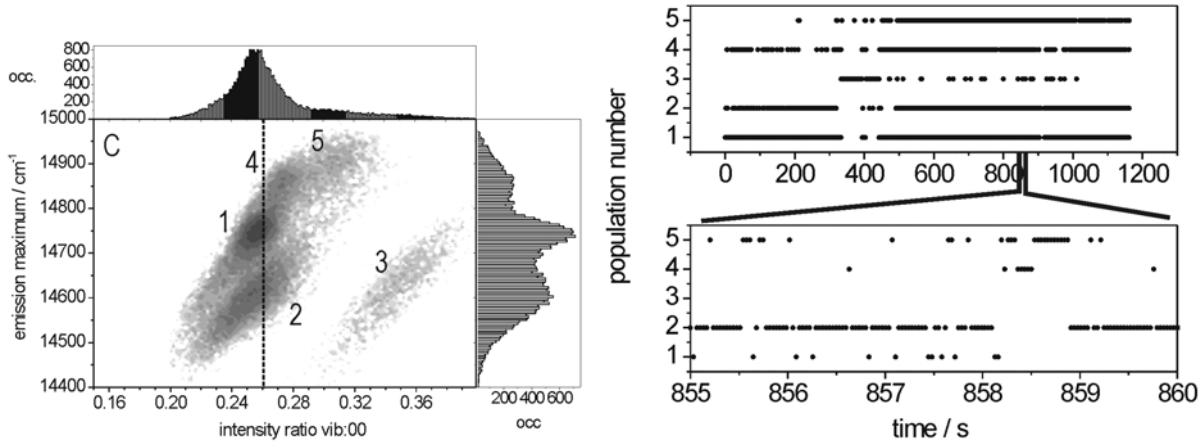

Figure 91: Individual sub-populations are assigned a number. The jumps between the assigned sub-populations are shown in the right graph

The jumps between these sub-populations are analysed and are shown to occur randomly (as opposed to the observations described in [Boiron99] for terrylene in p-terphenyl at cryogenic temperatues). Note that the following table, indicating the occurence of steps from one population to another is diagonally symmetric (i.e. steps occur in all directions in equal measure):

		step from:				
		1	2	3	4	5
to:	1	11348	1353	3	813	223
	2	1355	9586	17	195	518
	3	1	19	2917	3	8
	4	825	202	1	2031	275
	5	212	505	10	298	1443

Global Analysis: The individual two-dimensional histogrammes obtained for many different single molecules can be superimposed, to generate a global picture of spectral positions of the individual the populations and sub-populations (fig. 92).

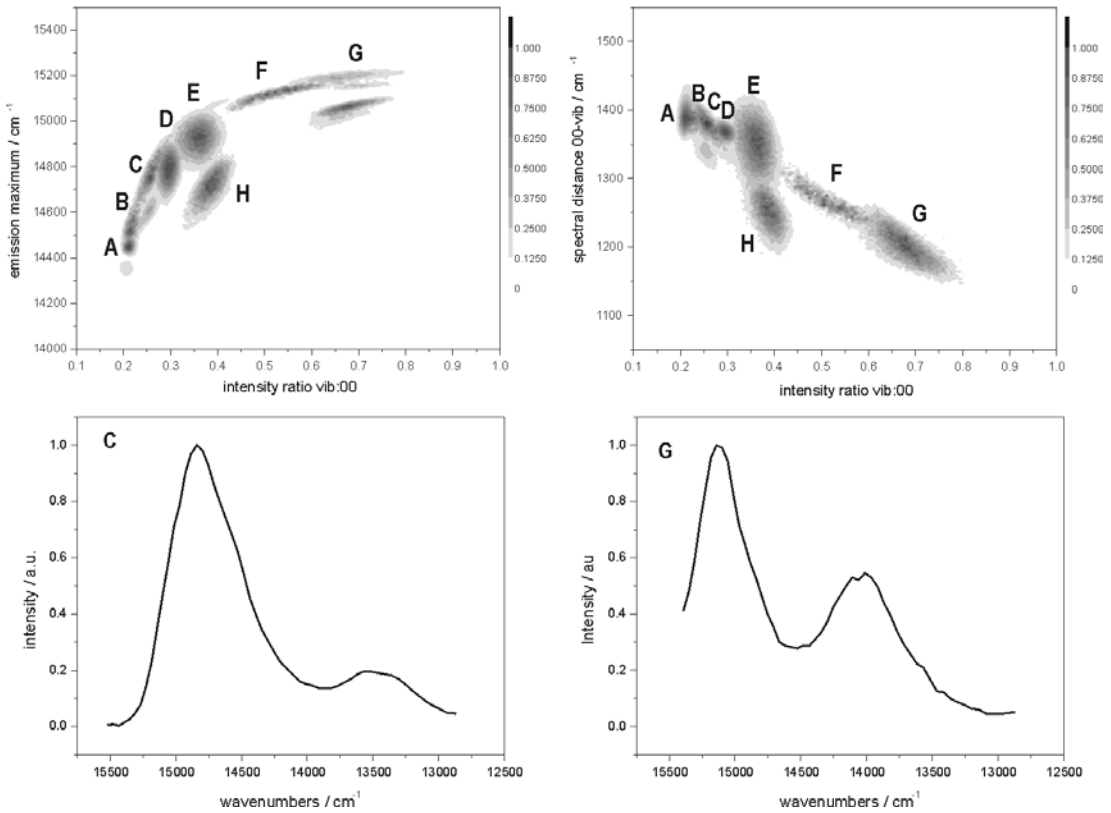

Figure 92: Global analysis. All populations (visualized as two dimensional histograms) are superimposed to generate the graphs in the upper row. a) shows the populations of emission maximum versus intensity ratios and b) the intensity ratios versus spectral distance. The spectra in the lower row (an exemplary spectrum of molecule C and G) illustrate the differences between extreme spectra.

The population histograms seem to follow a trend, in which the vibronic coupling increases with the energetic position of the main band, and at the same time the spectral distance between the main and the vibronic band decreases. The individual populations of spectra (the individual 'cluods') follow similar trends, however, on a smaller spectral region. The widths of the individual spectral distributions are significantly smaller than the entire, global distribution. That is, large jumps, for example going from the population of molecule A in fig. 92 to F have not been observed.

Summary and conclusion: The possibility to obtain ten-thousands of relatively well-resolved spectra of an individual molecule in a polymer matrix allows for a thorough analysis of the spectral diffusion. The observations described in this section are the following: (a) Spectral diffusion generates a distribution of spectral parameters (emission maximum, intensity ratios, etc.). (b) The observed dynamics of the spectral diffusion reaches a limit on a time-scale of a few seconds, and depends on the irradiation intensity. (c) Some molecules show spectral jumps to distinct sub-populations of spectral parameters. These jumps are uncorrelated. (d) On a global picture it was possible to verify that a spectral shift to higher energies correlates with an increase of the intensity ratio, and that (e) an increase of the intensity ratio correlates with a change in the vibronic progression (the distance between the bands becomes smaller). Using the schematical energy diagrams:

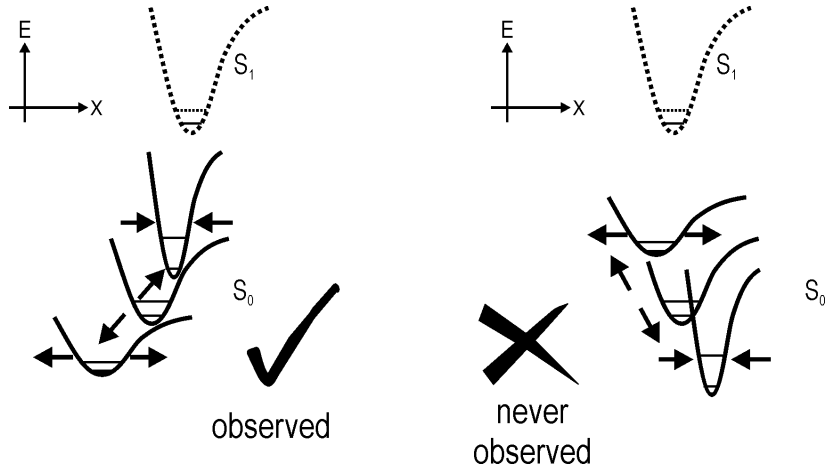

Figure 93: The schematical model on the left illustrates the observed trend, that a spectral shift towards lower energies is concomitant with a change in the vibronic coupling and with a change in the vibronic progression.

(f) The distribution of spectral populations is on a global scale is much broader than the observed variability within an individual population. To interpret these observations a series of simulations are needed, that shall explore to what extent the influence of the matrix (e.g. different positions of the molecule close or far to hydrogen-bond acceptors / donors) and to what extent deformations on the molecule give rise to the different spectra.

4.8. Covalently bound Cy5 in MCM-41

Introduction: A sample consisting of an MCM-41 host with covalently bound Cy5 molecules has been synthesized in the group of Prof. Michael Wark, Bremen / Hannover.

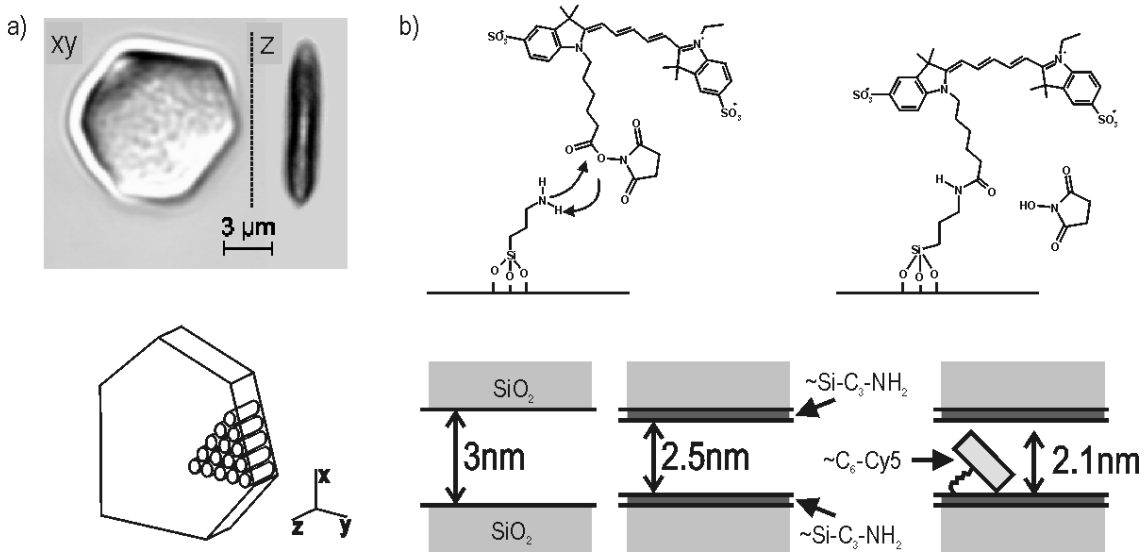

Figure 89: Cy-5 / MCM-41 sample. a) Transmission images (in plane and z-scan) of an MCM-41 particle of the investigated batch. The schematical illustration shows the pore orientation with respect to the particle shape. b) Cy-5 is bound via a linker to the walles of MCM-41. Below: Pore-diameter versus molecule-size relations in the Cy-5 / MCM-41 material.

The micrometer-sized, roughly hexagonal shaped prisms of MCM-41 were synthesized via homogeneous precipitation, as described in [Rathousky98] and [Rohlfing03] The approximate size (3 nm) and topology (hexagonal) of the pores was determined via adsorbtion isotherms and XRD measurements. The external surface of the MCM-41 material was passivated with diphenyl-dichlorosilane (DPDCS) before the linker 3-aminopropyl triethoxysilane (APTES) was bound to the internal surface of the material. Cy-5 was then bound to the primary amino-group of the linker via its succinimide-ester functionality. (see. fig.89). The samples are availiable in a concentration series of Cy-5 from 10^{-6} to 10^{-12} moles per gramme of material. In the highest concentration the

fluorescence signal is spread homogenously over the entire sample, and shows a continuous photobleaching behavior (fig. 90a). In the samples with the highest dilution the fluorescence of the molecules is visible as the diffraction limited patterns that exhibit the characteristic single-molecule on/off bleaching behavior (see fig.90b).

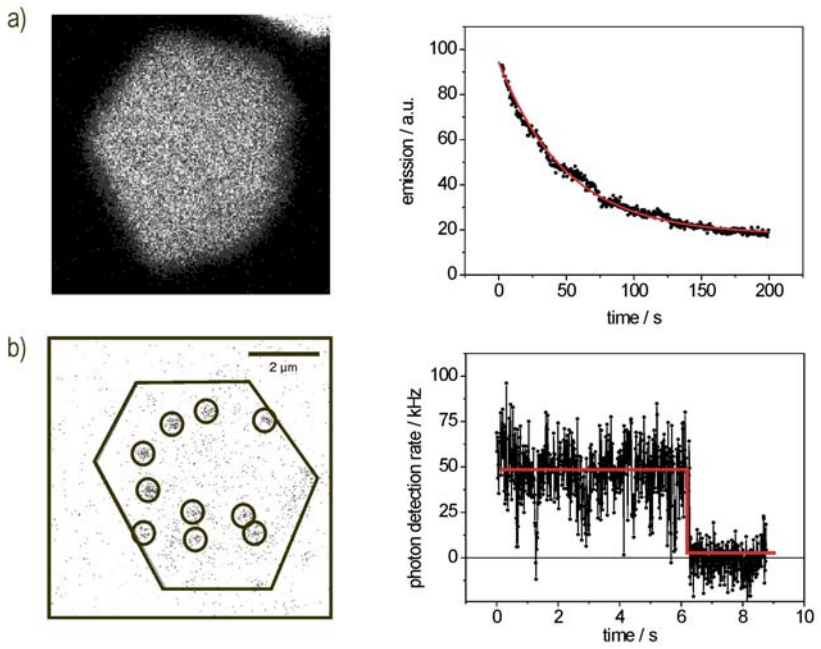

Figure 90: Samples in a)10^{-6} mol/g and b) 10^{-12} mol/g of material. The typical ensemble and typical single.molecule bleaching behavior are shown in the graphs.

A series of questions regarding the material have been addressed using SMS methods. (a) Is the loading of the material homogenous? Do the molecules show some preferential orientation with respect to the pores? (b) Can the covalent attachment of the dyes be verified? (c) Are the pores which contain the dyes accessible to other molecules coming from the outside, or are the pores sealed off? (d) Is there any visible influence of the solvent on the chromophores?

Preliminary studies on this samples have been described in [Seebacher02d], and showed (a) that there is a preferential orientation of the guest molecules along the pore axis and (b) that the molecules are immobile. More detailed studies are presented in this section.

Orientation of Cy-5 in MCM-41: The orientational distribution of the covalently bound dyes is obtained from the orientations of many (ca. 30) individual molecules (as described for the orientational distribution of oxazine dyes in $AlPO_4$-5 in section 4.3) and the evaluation of the angles against a referential angle determined by the shape of the sample. The study of the orientational distribution is in this case is expanded to the orienational distribution along the pore direction (referential angle is defined as the *z*-axis, see figure 89a), and perpendicular to the pores (referential in the *xy*-plane, see figure 89a).

(a) Orienation along the pore axis: The analysis of the orientational distribution along the *z*-axis (= 0°) shows that the transition dipole moment of the molecules is more or less well aligned with pore axis, with a distribution of ξ= 34±2° (from [Seebacher02d])

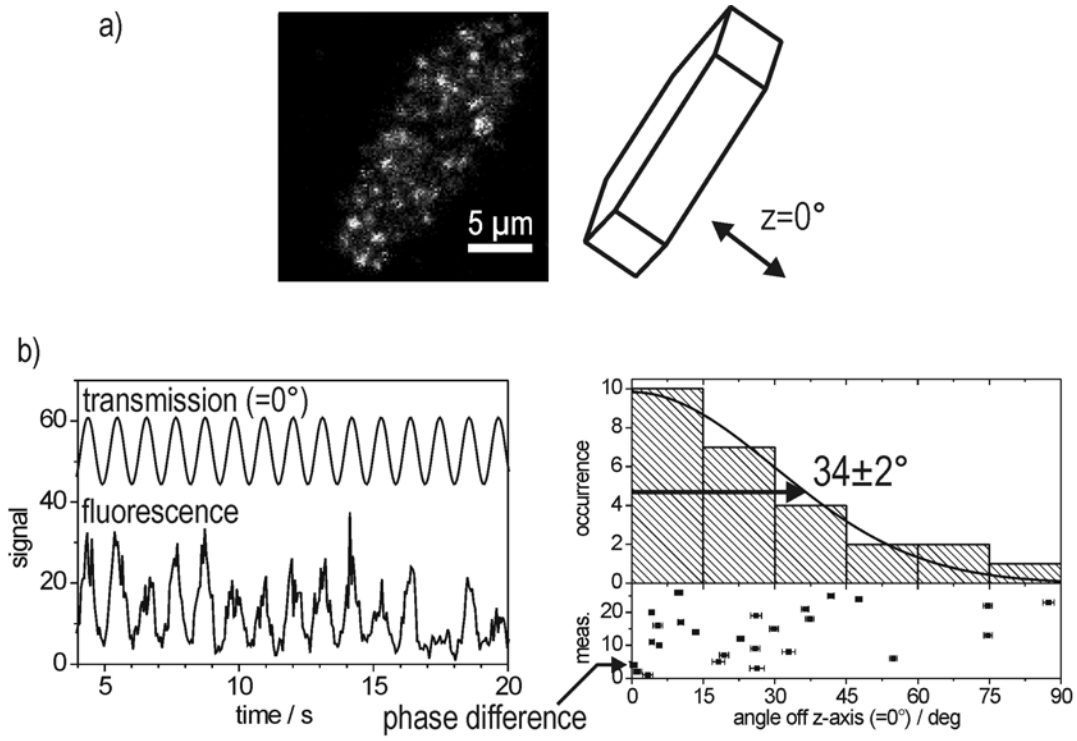

Figure 91: Orientation angles along the pore axis. a) MCM-41 particle lying on the side, showing diffraction limited patterns from individual Cy-5 molecules. b) Left is the polarization dependent curve for an individual Cy-5 in MCM-41. 28 individual molecules were analysed to generate the histogram to the right (adapted from [Seebacher04]).

(b) Orientation perpendicular to the pores (xy-plane): For the analysis of the orientations perpendicular to the pores it is necessary that the shapes of the individual analysed particles (which may deviate strongly from an idealised hexagon) come as close as possible to an ideal hexagon. It is difficult to determine a common referential orientational angle for the individual MCM.41 particles. For this reason the orientational distribution of the dyes in the *xy*-plane is less well defined than in the case of the *z*-axis. The orientational distribution in the *xy*-plane is therefore analysed with respect to molecules pointing to the edge or to the side of a nearly hexagally shaped particle (cf. fig 92). The distribution of the angles (right graph in fig. 92b) does not show a clear preferential orientation of the molecules pointing to the side or to the edges of the particle.

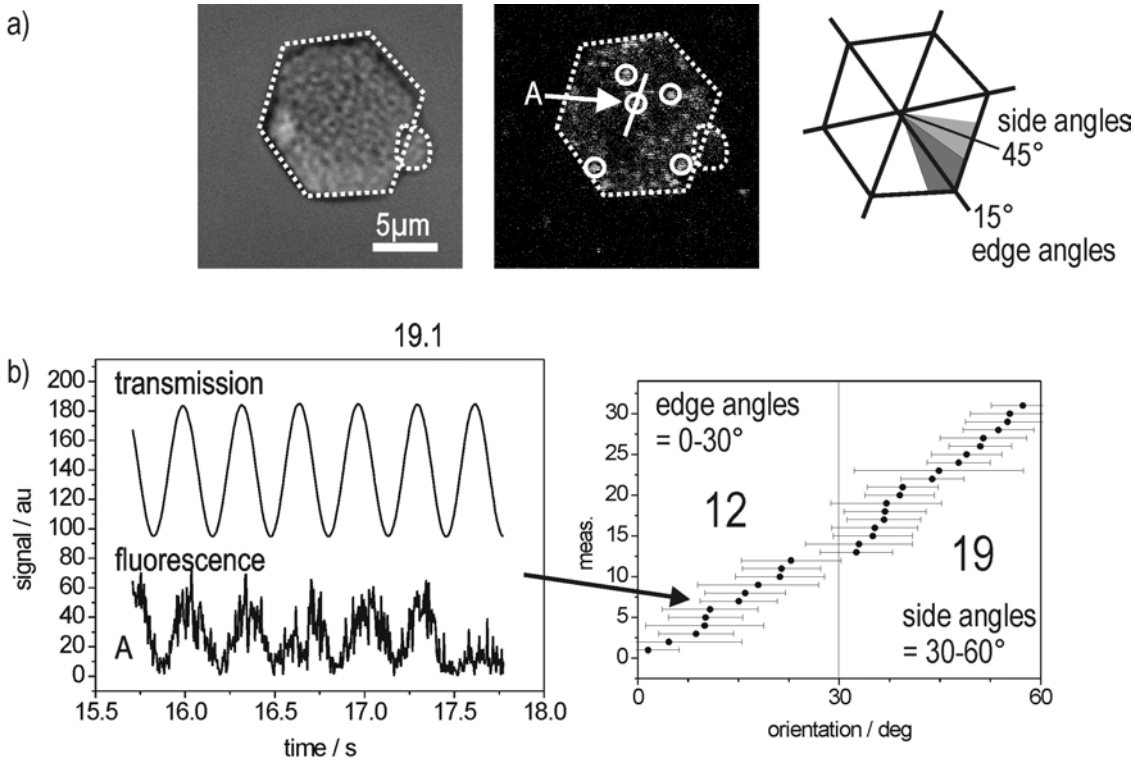

Figure 92: Orientation angle perpendicular to the pore direction (in the *xy*-plane). a) Transmission and fluorescence image of a nearly hexagon-shaped MCM-41 particle containing individual Cy-5 molecules. b) The angle of one molecule (A) is obtained from polarization dependent curves. This particular molecule can be assigned to the group of molecules oriented towards the edge of the hexagon.

Solvent dependence: Important questions concerning this sample is as to whether the individual dyes in the pores are accessible to solvents coming from the exterior, and what effect the solvent will have on the individual molecules. To study this, the samples are evacuated (10^{-7} mbar) to remove any residual adsorbed species, and then embedded in five different solvents. All solvents have been freshly degassed prior to the embedding and the solvent/sample suspensions are kept in inert gas in a sealed recipient. The five solvents used are: 1. tri-isopropylbenzene (TIB, spectroscopy grade MERCK), as a large solvent (diameter ca. 1 nm), 2. dodecane (C_{12}, spectroscopy grade), as an apolar solvent, 3. chloroform ($CHCl_3$, spectroscopy grade, MERCK), as a standard solvent, 4. ethylen-glycol (EG, spectroscopy grade) and 5. water (H_2O, deionized and distilled, HPLC grade, ACROS) as solvents with increasing polarity. The samples are left to equilibrate over night. For the microscopy studies a drop of a solvent/particle suspension is then placed in a microscopy holder with a cavity (fig93).

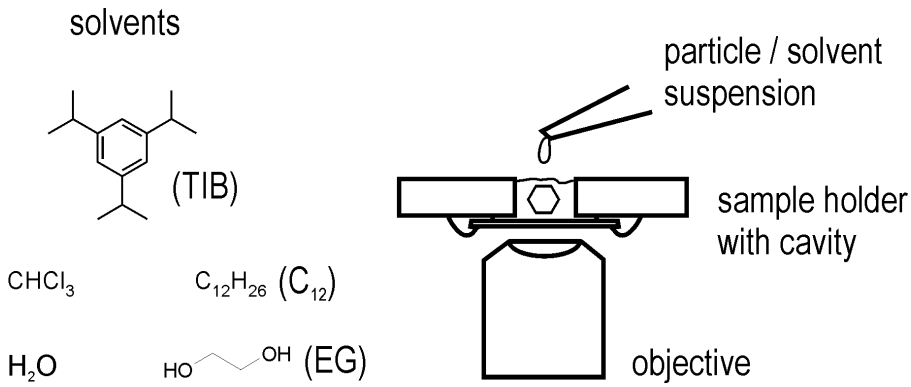

Figure 93: Used solvents and schematical drawing illustrating the sample preparation for the microscopy studies

Three different measurements are carried out to study the influence of the solvents on the individual Cy-5 molecules in the sample: (a) a photostability study, (b) a study concerning the emission spectra in dependence of the solvents and (c) a study with the aim to detect orientational dynamics of the individual dyes. The results of these three studies are described in more detail in the following

(a) Photostability: A series of 20 fluorescence images is acquired for each of the five samples embedded in the different solvents with the confocal microscope. The sequence is recorded using acquisition time of 16.2 s per frame and 60 s between frames. The excitation power is 34µW in all cases, using circularly polarized light (λ/4-retardation plate is placed in front of the objective barrel). Two typical sequences are shown in figure 94. The upper row shows the bleaching of a Cy-5/MCM-41 particle embedded in C_{12}. The lower row shows a sequence recorded for a sample embedded in water recorded under identical conditions.

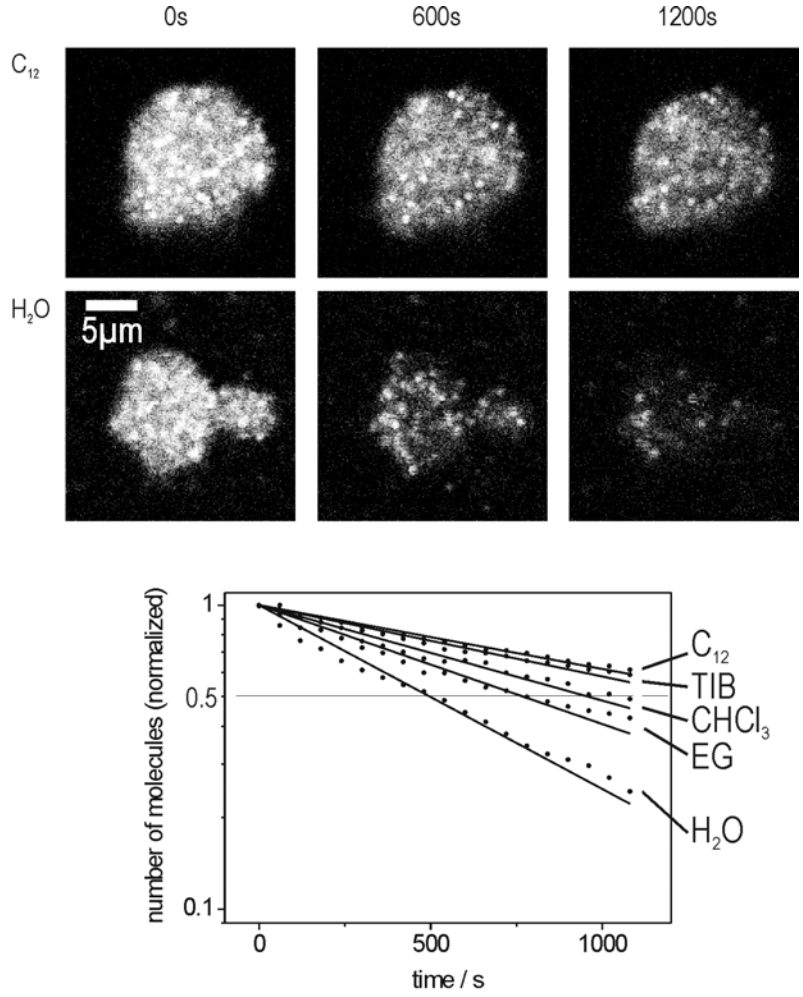

Figure 94: Photobleaching behavior of Cy-5 / MCM-41 samples embedded in different solvents. Note the semi-log scale in the graph.

The number of individual molecules is determined for all 20 frames and plotted versus time. The graphs are all normalized to unity and plotted using a semi-logarithmic scale

(see graph in fig. 94). The bleaching behaviors show a pronounced differences on going from apolar to polar solvents, where the bleaching is significantly faster. It is a common observation that dyes are less photostable in polar media (e.g. [Eggeling05]). This is a first indication that the solvents reach the individual dyes in the channels of the MCM-41 material.

(b) Spectral distributions: The distribution of spectral maxima confirms the observations made in the photobleaching study. Hundreds of spectra can be recorded for hundreds of molecules in the different samples using the confocal microscope and the prism-CCD device (acquisition time of 40 ms per spectrum). The distribution of the emission maxima are obtained from the fits to the sequences of spectra (using a double Gaussian to model the spectra, cf. fig 95, left emission spectrum).

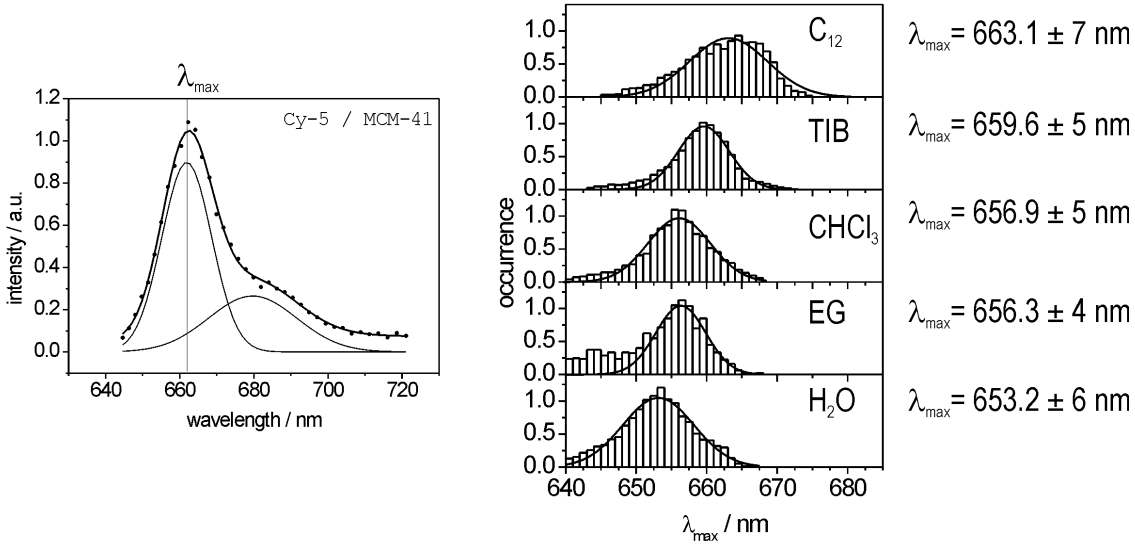

Figure 95: The spectrum of an individual Cy-5 in MCM-41 can be fitted by a double Gaussian. The emission maximum of hundreds of spectra recorded for hundreds of molecules are used to generate the histograms in the right graph.

The distributions are comparatively broad and overlap considerably (right graph in fig. 95), nevertheless it is possible to observe a pronounced blue shift (of ca. 10 nm) on going from the apolar to the more polar solvents. The blue-shift increasing with solvent polarity is a well-documented and common observation (e.g. [Mei00]).

(c) Orientational behaviour:.From the dimensions of the pore, of the dye and of the solvents it can be expected that some form of orientational mobility may be observed in the case of solvent TIB, provided (a) that the dyes are not adorbed strongly to the pore walls and (b) the linker chain is flexible enough. To observe the orientational behavior, individual fluorescence spots are selected and the emission intensity observed in dependence of the excitation polarization plane. In the sample containing TIB a few (3 out of 30) cases showed orientational jumps (see fig.96) - this was not the case in the samples embedded in the other solvents.

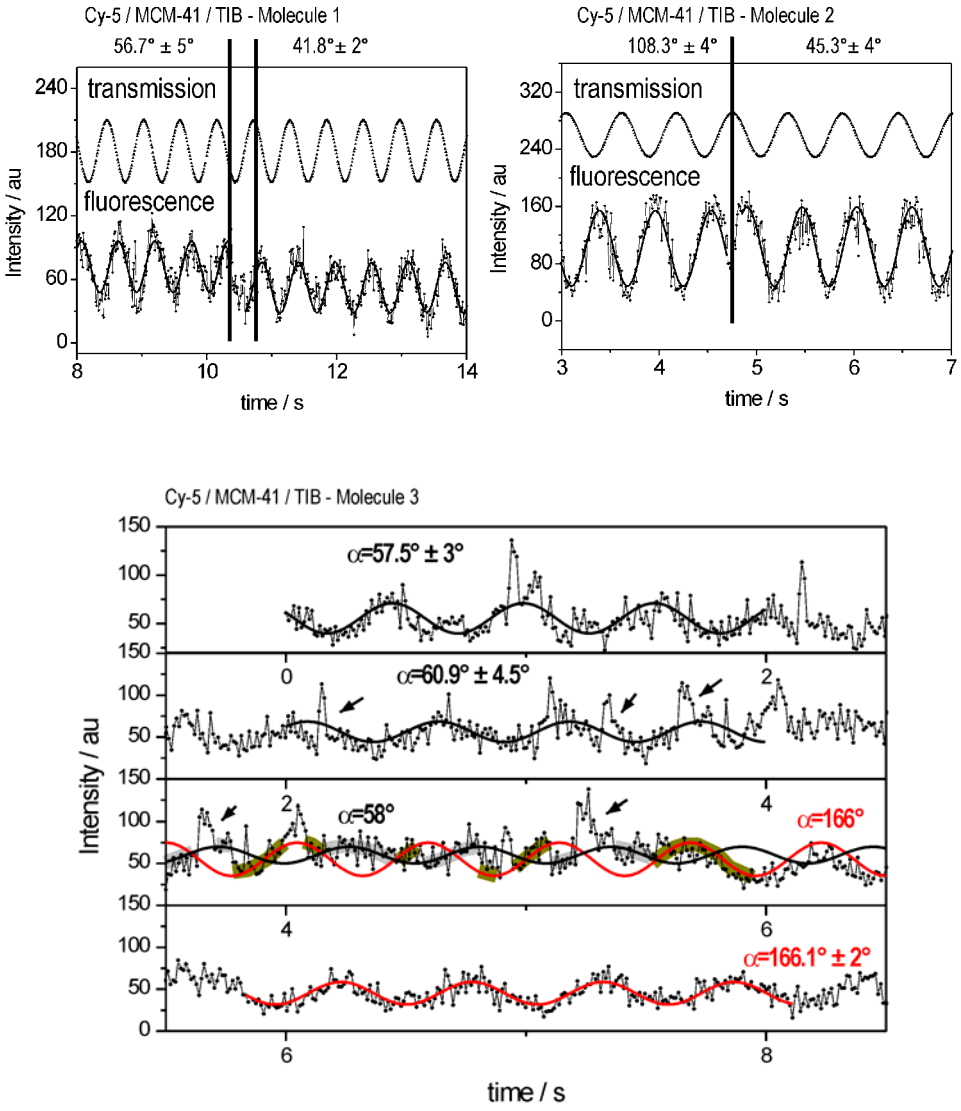

Figure 96: The three cases of (pronounced) orientational jumps in TIB / Cy-5 / MCM-41.

The two fist cases depicted in fig. 96, molecule 1 and 2, show an abrupt orientational jump of ca. 15° and ca. 60°. Molecule 3 starts at an orientation of ca. 60° for about 4 seconds shows orientational dynamic between 4 and 6 seconds and then remains at a stable orientation of ca. 166° for the remaining trace. The orientational behavior of the molecule in the time-segment between 4 and 6 seconds can be explained assuming a jumping ('flip-flop') movement between the two orientations before and after this time-segment. Also interesting is the appearance of intensity spikes (indicated by arrows in fig. 96) which could be due to very short orientational movements of the Cy.5 molecules.

Conclusion and Outlook: Cy-5 molecules are covalently attached to the inner surface of MCM-41 particles via a flexible linker, the molecules align well to the pore orientation. Solvents can be loaded into the channels. The solvents affect the photostability and the spectral distribution of the individual fluorophores depending on their polarity. In the case of large solvents it is also possible to detect effects of the confined geometry. These large solvent molecules cannot easily pass by a dye in a pore, eventually causing the dye molecule to move to a different position / orientation in the channel.

The internal functionalization of nanostructured samples is an important step in the direction of fabricating functional materials. In this study it could be shown that the functionalization procedure succeeded and that the pores and in this case the covalently attached Cy-5 dye molecules are still accessible to species coming from the exterior of the sample. In a next step further molecules will be incorporated and covalently bound to the interior of such samples. Azo-dyes, for example, which can be switched optically between the *cis*- and *trans*- isomers, could be thought of as valves that open and shut the individual pores. Biological receptors, for example, open interesting possibilities for the application of these systems in biophysical studeis.

5. Summary

Single-molecule spectroscopy (SMS) and microscopy was successfully used to characterize the behavior of fluorescent dye molecules incorporated as guests into the channels of inorganic porous materials (host-guest materials).

The results of the experimental investigations are summarized as follows:

(a) Bulk measurements (4.1.): Many host-guest materials have been synthesized by collaborating groups. Only few, however, prove to be of suitable quality for the more eleaborate SMS studies. In fact, all samples with a size larger than 3µm were found to contain heterogeneities. Studies using the more straightforward ensemble method of fluorescence micorscopy have been carried out on a large variety of samples. The most interesting results are included in this thesis: (i) the formation of domains with different concentrations of fluorescent dyes in $AlPO_4$-5, which may be caused by different crystal growth rates (ii) the detection of cracks and defects using dyes that are too large to penetrate the narrow pores of a zeolite is shown exemplarily for an apparently sealed off and defect free MFI coat around alumina beads and (iii) the estimation of the diffusion coefficient by observing the penetration depth of a dye front diffusing into a porous particle as a function of time. Bulk measurements are comparatively easy to conduct and they provide useful information, for example to define whether a sample is suitable for the SMS experiments or if there are more essential problems, for example in the synthesis, that have to be addressed first. [Hellriegel03], [Hellriegel03b], [Hellriegel04a]

(b) Photostability of dyes (4.2.): Dyes that are to be detected as individual guests in the host materials should have a high fluorescence quantum yield, and be as stable as possible against photobleaching. Fluorophores emit a statistically characteristic number $\langle n \rangle$ of photons before they undergo an irreversible reaction to a non-fluorescing species (photobleaching). This number depends on the dye and the dye's immediate surroundings. It was determined for two novel dye molecules, a water-soluble perylen diimide derivative (wTDI) in poly-vinylalcohol (PVA): $\langle n \rangle = (6.7 \pm 0.2) \cdot 10^6$, and a

streptocyanine dye (9A1) in poly-methylmethacrylate (PMMA): $\langle n \rangle = (4.4 \pm 1.7) \cdot 10^6$. These numbers are obtained from many (30-80) intensity versus time traces of individual dye molecules.

(c)Orientational distribution of Oxazine dyes in $AlPO_4$-5 (4.3.): Four differently sized oxazine dye molecules, oxazine-4, oxazine-1, oxazine-170 and oxazine-750, with molecular widths of 0.75 nm, 0.85 nm, 1.0 nm and 1.1 nm respectively, have been incorporated into the one-dimensional pores of $AlPO_4$-5 with a pore diameter of 0.73 nm during synthesis. The orientations of the used dyes with respect to the pore axis were measured with polarization dependent confocal microscopy. The distribution function of the tilt angles was obtained from these data. The thinnest two molecules, oxazine-4 and oxazine-1, show gaussian type distributions with a half width at half maximum of ξ=14° and ξ=18°. The larger sized oxazine-170 shows a broader gaussian tilt function with ξ=48°, whereas the broadest molecule, oxazine-750, does not show a preferential orientation. These results clearly show that there is a structure directing influence of the host on the guest molecules in dependence of their size, even if the molecule is larger than the pore size.[Seebacher03]

(d) Diffusion of guests in mesoporous materials (4.4, 4.5 and 4.6): The diffusion of individual fluorescent molecules can be observed by single molecule tracking techniques and characterised by the analysis of their diffusional trajectory. Heterogeneities in the diffusivity that would pass undetected by conventional ensemble methods are resolved by this method. This is demonstrated in three sections of this thesis.

4.4. The translational motion of single terrylenediimide (TDI) dye molecules incorporated into the organic part of a surfactant-silica mesostructure of a monolithic M41S-host was observed by for the first time using confocal microscopy. The effective diffusion coefficient was evaluated to be $D = 3.72 \cdot 10^{-2}$ $\mu m^2 s^{-1}$, two orders of magnitude smaller than the diffusion coefficient of TDI in the pure lyotropic hexagonal phase of the same surfactant in water and four orders of magnitude smaller than the diffusion coefficient in chloroform. Despite the limited temporal resolution of this method it was

possible to observe tortuous trajectories and a sub-population of immobile molecules coexisting in the same sample.[Hellriegel00][Seebacher02]

4.5. Single molecule tracking with a wide-field fluorescence microscope improved the temporal resolution from 4 s (confocal) to 50 ms. With this technique details in the trajectories of indivdual molecules in a porous material become apparent. The first examination was carried out on a 9A1 streptocyanine dye diffusing in the pores of two sol-gel-glasses with differing mesopore sizes of 22 nm (M22) and 3 nm (M3). The majority of molecules in M22 diffuse with an average diffusion coefficient of $D = 6.9 \cdot 10^{-9}$ cm^2s^{-1}. Most of the 9A1 molecules in M3 are confined in regions ranging in size from 50 nm –the positioning accuracy of the setup – up to 200 nm. Other molecules in M3 are found alternately trapped and freely diffusing with an average $D = 1.2\times10^{-9}cm^2s^{-1}$. Besides traps, the wide spread of the diffusion coefficients for individual molecules in both gels reveals pronounced microscopic heterogeneities.[Hellriegel04b]

4.6. Widefield imaging was also used to readdress the motion of individual TDI in structured materials similar to MCM-41 - in this case spin-coated SBA-15 films. It is possible to observe structured trajectories and other inhomogeneities, such as bimodal step-size distributions and preponderance of steps in a specific direction. The full potential of the single molecule tracking can be explored, this is shown in this sedction for two exemplary trajectories. [Hellriegel05]

(e) Spectral dynamics of TDI in PMMA (4.7): The possibility to obtain well-resolved spectra of an individual fluorophore at room-temperature with a temporal resolution of 34 ms over a period of several minutes (resulting in ten-thousands of spectra per molecule), allows a very thorough characterization of the distribution and diffusion of spectral parameters. This is shown for TDI molecules embedded in PMMA. The spectra are characterized by the energetic position of the main band (0-0, between 14200 and 15300 cm^{-1}), the position of the well-resolved vibronic band (vib, red-shifted by between 1100 and 1450 cm^{-1}) and the intensity ratio between the two bands (I_{vib}:I_{00} typically between 0.2 and 0.9). It can be shown that these parameters do not only show

instantaneous fluctuations around a mean value but also diffuse over a broader spectral region (the emission maximum, for example, diffuses typically over a region between 100 and 200 cm^{-1}). In the observed cases this diffusion process is complete on a time-scale of 2-3 s, that is, the spectrum diffuses within a limited spectal range. In some cases it is also possible to observe distinct abrupt jumps to well-separated spectral regions, superimposed on the diffusional behavior, showing the presence of distinguishable spectral sub-populations. In the observed cases these spectral jumps occur randomly. On a global level it is possible to detect a trend in the distribution of spectral properties: A spectral shift to higher energies correlates with an increase of the intensity ratio (I_{vib}/I_{00}) and at the same time with a change in the vibronic progression (the spectral distance between the 0-0 band and the vibronic band becomes smaller).

(f) Characterization of a Cy5/MCM-41 sample (4.8): The internal functionalization of nanostructured samples is an important step in the direction of fabricating functional materials. The study presented in this section shows that the functionalization procedure, attaching Cy-5 covalently to the inner surface of a micrometer-sized MCM-41 particle, succeeded and that the pores (and in this case also the covalently attached Cy-5 dye molecules in there) remain accessible to species coming from the exterior of the sample. Different solvents (with different polarities and sizes) were loaded into the channels of Cy-5 / MCM-41 particles. The solvents affect the photostability and the spectral distribution of the individual fluorophores depending on their polarity. In the case of large solvents like tri-isopropylbenzene (diameter ca. 1 nm) it is also possible to detect effects of the confined geometry. These large solvent molecules cannot easily pass by a dye in a pore, eventually causing the dye molecule to change its orientation in the channel.

6. Bibliographical Information

[Ambrose99] Ambrose, P.; Goodwin, P.; Nolan, J. *Cytometry* **1999**, *36*, 224.

[Attard95] Attard, G.S.; Glyde, J.C.; Göltner, C.G. *Nature* **1995**, *378*, 366.

[Ban04] Ban, T.; Brühwiler, D.; Calzaferri, G. *J. Phys. Chem. B* **2004**, *108*, 16348.

[Barkai04] Barkai, E.; Jung, Y.; Silbey, R. *Annu. Rev. Phys. Chem.* **2004**, *55*, 457.

[Bartussek95] Bartussek, R.; Hänggi, P. *Phys Bl.* **1995**, *51*, 506.

[Basché95] Basché, T.; Kummer, S.; Bräuchle, C. *Nature* **1995**, *373*, 132.

[Basché96] Basché, T.; Bräuchle, C. *Ber. Bunsen-Ges. P. Chem.* **1996**, *100*, 1269.

[Basché97] Basché, T., Moerner, W. E., Orrit, M., Wild, U. P., Eds. *Single-Molecule Optical Detection, Imaging and Spectroscopy*; VCH: Weinheim,**1997**.

[Baumann01] Baumann, R.; Ferrante, C.; Deeg, F.W.; Bräuchle C., *J. Chem. Phys* **2001**, *114(13)*, 5781.

[Baumann03] Baumann, R.; Ferrante, C.; Kneuper, E.; Deeg, F.W.; Bräuchle C., *J. Phys. Chem. A* **2003**, *107*, 2422.

[Benes01] Benes, N. E.; Jobic, H.; Verweij, H. *Mic. Mes. Mat.* **2001**, *43*, 147.

[Berg93] Berg, H.C. *Random Walks in Biology*, Princeton University Press **1993**.

[Besson03] Besson, S.; Gacoin, T.; Ricolleau, C.; Jacquiod, C.; Boilot, JP. *J. Chem. Mater.* **2003**, *13(2)*, 404.

[Binnig82] Binnig, G.; Rohrer, H.; Gerber, C.; Weibel, E. *Phys. Rev. Lett.* **1982**, *49*, 57.

[Binnig86] Binnig, G.; Quate, C.F.; Gerber, C. *Phys. Rev. Lett.* **1986**, *56*, 930.

[Björnstrom03] Björnström, J.; Martinelli, A.; Johnson, J. R. T.; Matic, A.; Panas, I. *Chemical Physics Letters* **2003**, *380*, 165.

[Blum01] Blum, C.; Stracke, F.; Becker, S.; Müllen, K.; Meixner A.J. *J. Phys. Chem. A* **2001**, *105*, 6983.

[Bobroff86] Bobroff, N. *Rev. Sci. Instrum.* **1986**, *57*, 1152.

[Boiron99] Boiron, A.M.; Tamarat, P.; Lounis, B.; Brown, R.; Orrit, M. *Chem Phys* **1999**, *247*, 119.

[Bondi64] Bondi, A. *J. Phys. Chem.* **1964**, *68*, 441.

[Bonilla01] Bonilla, G.; Tsapatsis, M.; Vlachos, D.G.; Xomeritakis, G. *J. Membrane Science* **2001**, *182*, 103.

[Bordat02] Bordat, P.; Brown, R. *J. Chem. Phys.* **2002**, *116(1)*, 229.

[Braun00] Braun, I.; Ihlein, G.; Laeri, F.; Nöckel, J.; Schulz-Ekloff, G.; Schüth, F.; Vietze, U.; Weiss, Ö.; Wöhrle, D. *Appl. Phys. B* **2000**, *70*, 335.

[Brinker85] Brinker, C.J.; Scherer, G.W. *J. Non-Crystal. Solids* **1985**, *70*, 301.

[Brinker90] Brinker, C.J.; Scherer, G.W. *Sol-Gel Science* **1990** Academic Press, San Diego, ISBN 0-121-34970-5.

[Calzaferri03] Calzaferri, G.; Huber, S.; Maas, H.; Minkowski, C. *Angewandte Chemie (Int. Ed.)* **2003**, *42(32)*, 3732.

[Cao98] Cao, X.; McHale, J.L. *J. Chem. Phys* **1998**, *109*, 1901.

[Caro94] Caro, J.; Marlow, F.; Wübbenhorst, M. *Adv. Mater*. **1994** , *6*, 413.

[Carslaw59] Carslaw, H.S.; Jaeger, J.C. *Conduction of heat in solids* Oxford University Press, 2 Ed., **1959**.

[Cauzzi99] Cauzzi, D.; Deltratti, M.; Predieri, G.; Tiripicchio, A.; Kaddouri, A.; Mazzocchia, C.; Tempesti, E.; Armigliato, A.; Vignali, C. *Appl. Catal. A* **1999**, 182, 125.

[Chandrasekhar43] Chandrasekhar S. *Rev. Mod. Phys.* **1943**, *15(1)*, 1.

[Christ01] Christ, T.; Kulzer, F.; Bordat, P.; Basché, T. *Angew. Chem.* **2001**, 113, 4323.

[Corma04] Corma, A.; Garcia, H. *Eur. J. Inorg. Chem.* **2004**, p. 1143.

[Cotlet04] Cotlet,M.;Masuo,S.; Luo,G.B.; Hofkens,J.; Van der Auweraer,M.; Verhoeven, J.; Müllen, K.; Xie, X.L.S.; De Schryver, F. *Proc. Nat. Acad. Sci.* **2004**, *101*, 14343.

[Davis02] Davis, M.E. *Nature* **2002**, *417*, 813.

[Dereux00] Dereux, A.; Girard, C.; Weeber, J.C. *J. Chem. Phys.* **2000**, *112*, 7775.

[Deschenes01] Deschenes, L. A.; Vanden Bout, D. A. *Science* **2001**, *292*, 255.

[Dewar77] Dewar, M. J. S.; Thiel, W. *J. Am. Chem. Soc.* **1977**, *99*, 4907.

[Domenech05] Domenech, A.; Ferrer, B.; Fornes, V.; Garcia, H.; Leyva, A. *Tetrahedron* **2005**, *61*, 791.

[Durand01] Durand, Y.; Bloeß, A.; Köhler, J.; Groenen, E.J.J.; Schmidt, J. *J. Chem. Phys.* **2001**, *114*(*15*), 6843.

[Eggeling98] Eggeling, C.; Widengren, J.; Rigler, R.; Seidel, C.A.M. *Anal. Chem.* **1998,** *70*, 2651.

[Eggeling05] Eggeling, C.; Volkmer, A.; Seidel, C.A.M. *ChemPhysChem* **2005**, *6*, 791.

[Ehrl94] Ehrl, M.; Deeg, F.W.; Bräuchle, C.; Franke, O.; Sobbi, A.; Schulz-Ekloff, G.; Wöhrle, D. *J. Phys. Chem.* **1994**, *93*, 47.

[Einstein05] Einstein, A. *Annalen der Physik* **1905**, *17*, 549.

[Einstein06] Einstein, A. *Annalen der Physik* **1906**, *19*, 371.

[Elson74] Elson, E. L.; Madge, D. *Biopolymers* **1974**, *13*, 1.

[Fleury93] Fleury,L.;Zumbusch,A.;Orrit,M.;Brown,R.;Bernard, J. *J. Lumin.* **1993**, *56*, 15.

[Fleury00] Fleury, L.; Segura, J.M.; Zumofen, G.; Hecht, B.; Wild, U.P. *Phys. Rev. Lett.* **2000**, *84*, 1148.

[Fultz02] Fultz, B.; Howe, J.M. *Transmission Electron Microscopy and Diffractometry of Materials (2nd. Ed.)* **2001** Springer, Berlin ISBN 3-540-67841-7.

[Funatsu95] Funatsu, T.; Harada, Y.; Tokunaga, M.; Saito, K.; Yanagida, T. *Nature* **1995**, *374*, 555.

[Gaebel04] Gaebel, T.; Popa, I.; Gruber, A.; Domhan, M.; Jelezko, F.; Wrachtrup, J. *New J. Phys.* **2004**, *6*, 98.

[Ganschow01] Ganschow, M.; Schulz-Ekloff, G.; Wark, M.; Wendschuh-Josties, M.; Wöhrle, D. *J. Chem. Mater.* **2001**, *11*, 1823.

[Gfeller98] Gfeller, N.; Megelski, S.; Calzaferri, G. *J. Phys. Chem. B* **1998**, *102*, 2434.

[Giessibl03] Giessibl, F.J. *Rev. Mod. Phys.* **2003**, *75*, 949.

[Göhde98] Göhde, W.; Fischer, U.C.; Fuchs, H.; Tittel, J.; Basché, T.; Bräuchle, C.; Herrmann, A.; Müllen, K. *J. Phys. Chem. A*, **1998**, *102*, 9109.

[Gölltner97] Gölltner, C.G.; Antonietti, M. *Adv. Mater* **1997**, *9*, 431.

[Grosso04] Grosso, D.; Cagnol, F.; Soler-Illia, G.J.D.A.; Crepaldi, E.L.; Amenitsch, H.; Brunet-Bruneau, A.; Bourgeois, A.; Sanchez, C. *Adv. Funct. Mater.* **2004**, *14 (4)*, 309.

[Gruber97] Gruber, A.; Dräbenstedt, A.; Tietz, C.; Fleury, L.; Wrachtrup, J.; von Borczyskowski, C. *Science* **1997**, *276*, 2012.

[Guth86] Guth, J.L.; Kessler, H.; Wey, R. *Stud. Surf. Sci.* **1986**, *28*, 121.

[Ha03] Ha, T.; Xu, J. *Phys. Rev. Lett.* **2003**, *90*, 223002.

[Hecht00] Hecht, B.; Sick, B.; Wild, U. P.; Deckert, V.; Zenobi, R.; Martin, O. J. F.; Pohl, D.W. *J. Chem. Phys.* **2000**, *112*, 7761.

[Hell03] Hell, S.W. *Nature Biotechnol.* **2003**, *21 (11)*, 1347.

[Hell04] Hell, S.W. *Physics Letters A* **2004**, *326 (1-2)*, 140.

[Hellriegel00] Hellriegel, C. *Diplomarbeit*, **2000** LMU München.

[Hellriegel03] Seebacher,C. Hellriegel,C. Deeg,F.W. Bräuchle, C. in *Host Guest-Systems based on Nanoporous Materials* (Wark, Schüth, eds.) **2003** Wiley-VCH Verlag, Weinheim ISBN 3-527-30501-7 pg. 521

[Hellriegel03b] Weiss, Ö.; Schüth, F.; Loerke, J.; Marlow, F.; Benmohammadi, L.; Laeri, F.; Seebacher, C.; Hellriegel, C.; Deeg, F.W.; Bräuchle, C. *ibid.* pg. 544

[Hellriegel04a] Ganschow, M.; Hellriegel, C.; Kneuper, E.; Wark, M.; Thiel, C.; Schulz-Ekloff, G.; Bräuchle, C.; Wöhrle, D. *Advanced Functional Materials* **2004**, *14(3)*, 269.

[Hellriegel04b] Hellriegel, C.; Kirstein, J.;Bräuchle, C.; Latour, Virginie.; Pigot, T.; Olivier, R.; Lacombe, S.; Brown, R.; Guieu, V.; Payrastre, C.; Izquierdo, A.; Mocho, P. *J. Phys. Chem. B* **2004**, *108*, 14699.

[Hellriegel05] Hellriegel, C.; Kirtsein, J.; Bräuchle, C. *New J. Phys* **2005**, *1*, 23.

[Hirschfeld76a] Hirschfeld T., *Appl. Opt.* 15, **1976**, 2965.

[Hirschfeld76b] Hirschfeld T., *Appl. Opt.* 15, **1976**, 3135.

[Hofer03] Hofer, W.A.; Foster, A.S.; Shluger, A.L. *Rev. Mod. Phys.* **2003**, *75*, 1287.

[Hofkens01] Hofkens, J.; Vosch, T.; Maus, M.; Köhn, F.; Cotlet, M.; Weil, T.; Herrmann, A.; Müllen, K.; DeSchryver, F.C.; *Chem Phys Lett.* **2001**, *333*, 255.

[Hoppe93] Hoppe, R.; Schulz-Ekloff, G.; Wöhrle, D.; Shpiro, E.S.; Tkachenko, P.P. *Zeolites* **1993**, *13*, 222.

[Hou00] Hou, Y.; Bardo, A.; Martinez, C.; Higgins, D.A. *J.Phys Chem B.***2000**, *104*, 212.

[Ihlein98] Ihlein,G.; Schüth,F.; Krauß,O.; Vietze,U.; Laeri,F. *Adv. Mater.* **1998**, *10*, 1117.

[Jimenez02] Jimenez, A.; Galvan, J.C.; Aranda, P. *Electrochim. Acta* **2002**, *47*, 2281.

[Jung01] Jung, G., *Dissertation* **2001**, *LMU-München*, ISBN 3-89791-231-7

[Jung01b] Jung, G.; Wiehler, J.; Steipe, B.; Bräuchle, C.; Zumbusch, A. *ChemPhysChem* **2001**, *2*, 392.

[Kawai04] Kawai, T.; Yoshihara, S.; Iwata, Y.; Fukaminato, T.; Irie, M. *ChemPhysChem* **2004**, *5(10)*, 1606.

[Kettner94] Kettner,R.; Tittel, J.; Basché, T.; Bräuchle, C. *J. Phys. Chem.* **1994**, *98*, 6671.

[Kinosita98] Kinosita,K.; Yasuda,R.; Noji,H.; Ishiwata,S.; Yoshida,M. *Cell* **1998**, *93*, 21.

[Kiraz03] Kiraz, A.; Ehrl, M.; Bräuchle, C.; Zumbusch, A. *J. Chem. Phys.* **2003**, *118 (24)*, 10821.

[Kiraz05a] Kiraz, A.; Hellriegel, C. Ehrl, M.; Bräuchle, C.; Zumbusch, A. *ChemPhysChem* **2005**, *6*, 919.

[Kiraz05] Kiraz, A.; Ehrl, M.; Hellerer, T.; Müstecaplolu, Ö.E.; Bräuchle, C.; Zumbusch, A. *Phys. Rev. Lett.*, **2004**, *94*, 223602.

[Kirstein02] Kirstein, J. *Diplomarbeit*, Ludwig-Maximilians-Universität München.

[Kitamura99] Kitamura, K.; Tokunaga, M.; Iwane, A. H.; Yanagida, T. *Nature* **1999**, *397*, 129.

[Köhn00] Köhn, F.; Hofkens, J.; De Schryver, F.C. *Chem. Phys. Lett.* **2000**, *321*, 372.

[Kresge92] Kresge, C.T.; Leonowicz, M.E.; Roth, W.J.; Vartuli, J.C.; Beck, J.S. *Nature* **1992**, *359*, 710.

[Kruk00] Kruk, M.; Jeroniec, M.; Ko, C.H.; Ryoo, R. *Chem Mater.* **2000**, *12*, 1961.

[Kukla96] Kukla, V.; Kornatowski, J.; Demuth, D.; Girnus, I.; Pfeifer, H.; Rees, L. V. C.; Schunk, S.; Unger, K. K.; Kärger, J. *Science* **1996**, *272*, 702.

[Kulzer97] Kulzer, F.; Kummer, S.; Matzke, R.; Braüchle, C.; Basché, T. *Nature* **1997**, *387*, 688.

[Kulzer99] Kulzer, F.; Koberling, F.; Christ, T.; Mews, A.; Basché, T. *Chem Phys* **1999**, 247, 23.

[Kulzer04] Kulzer, F.; Orrit, M. *Annu. Rev. Phys. Chem.* **2004**, *55*, 585.

[Langley99] Langley, P.J.; Hulliger, J. *Chem Soc. Rev.* **1999**, *28*, 279.

[Lefebvre04] Lefebvre, J.; Fraser, J.M.; Finnie, P.; Homma, Y. *Phys Rev. B.* **2004**, *69*, 075403.

[Levine83] Levine, I.R. *Quantum Chemistry (3rd Ed.)* **1983**, Allyn and Bacon, Newton Massachusetts ISBN 0-205-07952-0, p. 228.

[Lu97] Lu, H.P.; Xie, X.S. *Nature* **1997**, *385*, 143.

[Mahurin03] Mahurin, S. M.; Dai, S.; Barnes, M. D. *J. Phys. Chem. B* **2003**, *107*, 13336.

[Mais97] Mais,S.; Tittel, J.; Basché, T.; Bräuchle, C.; Gohde, W.; Fuchs, H.; Müller, G.; Müllen, K. *J. Phys. Chem. A* **1997**, *101*, 8435.

[Margineanu04] Margineanu, A.; Hofkens, J.; Cotlet, M.; Habuchi, S.; Stefan, A.; Qu, J.; Kohl, C.; Müllen, K.; Verkammen, J.; Engelborghs, Y.; Gensch, T.; De Schryver, F.C. *J.Phys. Chem. B* **2004**, *108*, 12242.

[McCain03] McCain, K. S.; Hanley, D. C.; Harris, J. M. *Anal. Chem.* **2003**, *75*, 4351.

[McCalley05] McCalley, D.V. *J. Chromatography A* **2005**, *1073 (1-2)*, 137.

[McGlynn69] McGlynn,S.P.; Azumi, T.; Kinoshita, M. "*Molecular spectroscopy f the triplet state*", Prentice-Hall, New Jersey, USA, **1969**, LCCCN: 69-10922.

[Megelski01] Megelski, S.; Lieb, A.; Pauchard, M.; Drechsler, A.; Glaus, S.; Debus, C.; Meixner, A.J.; Calzaferri, G. *J. Phys. Chem. B* **2001**, *105*, 25-35

[Mei00] Mei, E.; Bardo, A.M.; Collinson, M.M.; Higgins, D.A. *J. Chem. Phys.* **2000**, *104*, 9973.

[Mei04] Mei, E.; Sharonov, A.; Gao, F.; Ferris, J.H.; Hochstrasser, R.M. *J. Phys. Chem. A*, **2004**, *108*, 7339.

[Meinershagen99] Meinershagen, J.; Bein, T. *J. Am. Chem. Soc.* **1999**, *121*, 448.

[Moerner99] Moerner, W. E.; Orrit, M. *Science* **1999**, *283*, 1670.

[Moerner02] Moerner, W.E. *J. Phys. Chem. B* **2002**, *106*, 910.

[Moerner04] Moerner, W.E. *New J. Phys.* **2004**, *6*, 88.

[Moller98] Moller, K.; Bein, T. *Chem. Mater.* **1998**, *10*, 2950.

[Molski00] Molski, A. *Chem. Phys. Lett.* **2000**, *324*, 301.

[Molski01] Molski, A. *J. Chem Phys.* **2001**, *114(3)*, 1142.

[Moore76] Moore, J. *Physikalische Chemie* 2. Aufl. (4th Ed.) **1976** Walter de Gruyter Verlag, Berlin ISBN 3-11-002127-7.

[Müller04] Müller, J.G.; Lupton, J.M.; Feldmann, J.; Lemmer, U.; Scherf, U. *Appl. Phys. Lett.* **2004**, *84(7)*, 1183.

[Nie97] Nie, S.; Zare, R.N. *Annu. Rev. Biophys Biomol. Struct.* **1997**, *26*, 567.

[Orrit90] Orrit, M.; Bernard, J. *Phys. Rev. Lett* **1990**, *65*(*21*), 2716.

[Orrit02] Orrit, M. *Single Mol.* **2002**, *3*, 255.

[Ozin00] Asefa, T.; Ishii, C.; McLachlan, H.;Ozin, G.A. *J.Mater.Chem* **2000**, *10*, 1751.

[Palmer02] Palmer, C.P. *Electrophoresis* **2002**, *23*, 3993.

[Pawley95] Pawley, J.B (ed.) *Handbook of Biological Confocal Microscopy* **1995**, Plenum Press, New York.

[Peterman04] Peterman, E.J.G.; Sosa, H.; Moerner, W.E. *Annu. Rev. Phys. Chem.* **2004**, *55*, 79.

[Petkov04] Nikolay Petkov, *Dissertation* **2004** *LMU München*

[Qian91] Qian, H.; Scheetz, M.; Elson E.L. *Biophysical Journal* **1991**, *60*, 910.

[Qu04] Qu, J.; Kohl, C.; Pottek, M.; Müllen, K. *Angew. Chem. Int. Ed.* **2004**, *43*, 1528.

[Rathousky98] Rathousky, J.; Zukalova, M.; Zukal, A.; Had, J. *Collect. Czech. Chem. Commun.* **1998**, *63*, 1893.

[Ravikovitch01] Ravikovitch, P.I.; Neimark, A.V. *J Phys Chem B* **2001**, *105*, 6817.

[Regier05] Regier, M.; Schuchmann, H.P. *Transp. in Mesoporous Media* **2005**, *59*, 115.

[Renge02] Renge,I.;Hubner,C.G.;Renn,A.;Langhals,H.;Wild, U.P. *J.Lumin.* **2002**, *98*, 91.

[Ricci04] Ricci, A.; Chretien, M.N.; Scaiano, J.C. *Chem. Mater.* **2004**, *16*, 2669.

[Rigler90] Rigler, R.; Widengren, *J. BioScience* **1990**, *40*, 180.

[Rigler93] Rigler, R.; Mets, U.; Widengren, J.; Kask, P. *Eur. Biophys. J.* **1993**, *22*, 169.

[Rigler01] Rigler, R., Elson, E. S., Eds. *Fluorescence Correlation Spectroscopy; Springer Series in Chemical Physics*; Springer: Berlin, **2001**.

[Rohlfing03] Rohlfing, Y. *Dissertation* **2002** Universität Bremen.

[Saxton97] Saxton, M. J.; Jacobson, K. *Annu. Rev. Bioph. Biomol. Struct.* **1997**, *29*, 373.

[Schmidt96] Schmidt, T.; Schutz, G. J.; Baumgartner, W.; Gruber, H. J.; Schindler, H. *Proc. Nat. Acad. Sci.* **1996**, *93*, 2926.

[Schulz02] Schulz-Ekloff, G.; Wöhrle, D.; van Duffel, B.; Schonheydt, R.A. M*icroporous Mesoporous Materials* **2002**, *51*, 91.

[Schuster02] Schuster,J.; Cichos,F.; v Borczyskowski,C. *J.Phys Chem. A* **2002**,*106*, 5403.

[Schüth95] Schüth, F. *Chem. unserer Zeit* **1995**, *29*, 42.

[Schütz97] Schütz, G.J.; Schindler, H.; Schmidt, T. *Biophys J.* **1997**, *73*, 1073.

[Schwarz95] Schwarz J.A.; Contescu C.; Contescu, A. *Chem. Rev.***1995**, *95*, 477.

[Seebacher01] Seebacher, C.; Rau, J.; Deeg, F.W.; Bräuchle, C.; Altmaier, S.; Jäger, R.; Behrens, P. *Advanced Matererials*, **2001**, *13*, 1374.

[Seebacher02] Seebacher, C.; Hellriegel, C.; Deeg, F. W.; Bräuchle, C.; Müllen, K.; Altmaier, S.; Behrens, P. *J. Phys. Chem. B* **2002**, *106*, 5591.

[Seebacher02d] Christian Seebacher, *Dissertation* **2002** *LMU München*

[Seebacher03] Seebacher, C.; Hellriegel, C.; Bräuchle, C.; Ganschow, M.; Wöhrle D. *J. Phys. Chem. B* **2003**, *107*, 5445.

[Seisenberger01] Seisenberger, G.; Ried, M. U.; Endreß, T.; Büning, H.; Hallek, M.; Bräuchle, C. *Science* **2001**, *294*, 1929.

[Song96] Song, L. L.; Varma, C. A. G. O.; Verhoeven, J. W.; Tanke, H. J. *Biophys. J.* **1996**, *70*, 2959.

[Sonnleitner99] Sonnleitner, A.; Schütz, G.J.; Schmidt, T. *Biophys J* **1999**, *77*, 2638.

[Szostak89] Szostak, R. *Molecular Sieves* **1989***, VNR New York* ISBN 0-442-28023-8.

[Stracke04] Stracke, F.; Blum, C.; Becker, S.; Müllen, K.; Meixner A.J. *Chemical Physics* **2004**, *300*, 153.

[Stelzer94] Stelzer, E.H.K.; Lindek, S. *Optics Communications* **1994**, *111*, 536.

[Talhavini98] Talhavini, M.; Atvars, T. D. Z. *J. Photochem. Photobiol A* **1998**, *114*, 65.

[Tamarat00] Tamarat, P.; Maali, A.;Lounis, B.L.;Orrit, M. *J. Phys. Chem. A* **2000**, *104*, 1.

[Thommes02] Thommes, M.; Köhn, R.; Fröba, M. *Appl. Surf. Sci.* **2002**, *196*, 239.

[Tittel95] Tittel, J.; Kettner, R.; Basché, T.; Bräuchle, C.; Quante, H.; Müllen, K. *J. Lumin* **1995**, *64*, 1.

[Verberk02] Verberk, R.; van Oijen, A.M.; Orrit, M. *Phys. Rev. B* **2002**, *66*, 233202.

[Vietze98] Vietze, U.; Krauß, O.; Laeri, F.; Ihlein, G.; Schüth, F.; Limburg, B. *Phys. Rev. Lett.* **1998**, *81*, 4628.

[Wark03] Wark, M. '*Synthesis Routes...*' in *Host Guest-Systems based on Nanoporous Materials* **2003** ISBN 3-527-30501-7 *Wiley-VCH Verlag, Weinheim*, p.2.

[Weber00] Weber, M.A.; Meixner, A.J. *J. Lumin.* **2000**, *86*, 181.

[Weh02] Weh, K.; Noack, M.; Hoffmann, K.; Schröder, K.P.; Caro, J. *Microporous Mesoporous Materials* **2002**, *54*, 15.

[Weiss99] Weiss, S. *Science* **1999**, *283*, 1676.

[Weiss01] Weiss, A. M.; Saraidarov, T.; Reisfeld, R. *Optical Materials* **2001**, *16*, 15.

[Weiss02] Weiss, Ö.; Loerke, J.; Wüstenfeld, U.; Marlow, F.; Schüth, F. *J. Solid State Chem.* **2002**, *167*, 302.

[Weston98] Weston, K.D.; Carson, P.J.; Metiu, H.; Buratto, S.K.; *J. Chem. Phys.* **1998**, *109*(*17*), 7474.

[Weston01] Weston, K. D.; Goldner, L. S. *J. Phys. Chem. B* **2001**, *105*, 3453.

[Wirth98] Wirth, M.J.; Swinton, D.J. *J. Anal. Chem.* **1998**, *70*, 5264.

[Wirth03] Wirth, M. J.; Swinton, D. J.; Ludes, M. D. *J. Phys. Chem. B* **2003**, *107*, 6258.

[Xie98] Xie, X. S.; Trautman, J. K. *Annu. Rev. Phys. Chem.* **1998**, *49*, 441.

[Xomeritakis99] Xomeritakis, G.; Gouzinis, A.; Nair, S.; Okubo, T.; He, M.Y.; Overney, R.M.; Tsapatsis, M. *Chem. Eng. Sci.* **1999**, *54*, 3521.

[Yang00] Yang, PD.; Wirnsberger, G.; Huang, H.C.; Cordero, SR.; McGehee, M.D.; Scott, B.; Deng, T.; Whitesides, G.M.; Chmelka, B.F.; Buratto, S.K.; Stucky, G.D. *Science* **2000**, *287*, 465.

[Yamaizumi78] Yamaizumi M, Mekada E, Uchida T, Okada Y. *Cell* **1978**, *15(1)*, 245.

[Yatskou03] Yatskou, M.M.; Meyer, M.; Huber, S.; Pfenniger, M.; Calzaferri, G. *ChemPhysChem* **2003**, *4*, 567.

[Ying99] Ying, J.Y.; Mehnert, C.P.; Wong, M.S. *Angew. Chem.* **1999**, *38*, 58.

[Zehetmayer02] Zehetmayer, P.; Hellerer, T.; Parbel, A.; Scheer, H.; Zumbusch, A. *Biophys. J.* **2002**, *83*, 407.

[ZeoliteAtlas05] Baerlocher, C.; McCusker, L.B. *Database of Zeolite Structures* latest version **2005** - URL: http://www.iza-structure.org/databases/

[Zhang02] Zhang,J.; Carl, P.J.; Zimmermann, H.; Goldfarb, D. *J. Phys. Chem. B* **2002**, *106*, 5382.

[Zondervan03] Zondervan, R.; Kulzer, F.; Orlinskii, S.B.; Orrit, M. *J. Phys. Chem. A* **2003**, *107*, 6770.

[Zondervan04] Zondervan, R.; Kulzer, F.; Kolchenko, M.A.; Orrit, M. *J. Phys. Chem. A* **2004**, *108*, 1657.

7. Appendix

7.1. Published Works

1) C. Seebacher, C. Hellriegel, F.W. Deeg, C. Bräuchle, S. Altmaier, P. Behrens, K. Müllen "Observation of translational diffusion of single terrylenediimide molecules in a mesostructured molecular sieve" *J. Phys. Chem. B* **2002**, *106*, 5591

2) C. Seebacher, C. Hellriegel, C. Bräuchle, M. Ganschow, D. Wöhrle „Orientational Behavior of Single Molecules in Molecular Sieves: A Study of Oxazine Dyes in $AlPO_4$-5 Crystals“, *J. Phys. Chem. B* **2003**, *107*, 5445.

3) C. Seebacher, C. Hellriegel, F.W. Deeg, C. Bräuchle "Confocal Microscopy and Spectroscopy for the Characterization of Host-Guest Materials" in *Host Guest-Systems based on Nanoporous Materials* **2003** Wiley-VCH Verlag, Weinheim ISBN 3-527-30501-7 pg. 521

4) Ö. Weiß, F. Schüth, J. Loerke, F. Marlow, L. Benmohammadi, F. Laeri, C. Seebacher, C. Hellriegel, F.W. Deeg, C. Bräuchle et al. "New Microlasers Based on Sieve/Laser Dye Composite Materials" *ibid* pg. 544

5) M. Ganschow, C. Hellriegel, E. Kneuper, C. Bräuchle, D. Wöhrle „Panchromatic Chromophore Mixtures in an AlPO4-5 Molecular Sieve: Spatial Separation Effects and Energy Transfer Cascades“, *Adv. Funct Mat.* **2004**, *14*, 269.

6) C. Hellriegel, J. Kirstein, C. Bräuchle, V. Latour, T. Pigot, R. Olivier, S. Lacombe, R. Brown, V. Guieu, C. Payrastre, A. Izquierdo, P. Mocho „Diffusion of Single Streptocyanine Molecules in the Nanoporous Network of Sol-Gel Glasses“, *J. Phys. Chem. B* **2004**, *108*, 14699.

7) C. Hellriegel, C. Kirstein, C. Bräuchle „Tracking of Single Molecules as a Powerful Method to Characterise Diffusivity of Organic Species in Mesoporous Materials“, *New J. Phys* **2005**, *7*, Art. 23

8) A. Kiraz, C. Hellriegel, M. Ehrl, C. Bräuchle, A. Zumbusch "Vibronic Excitation of Single Molecules: A New Technique for Studying Low-Temperature Dynamics." *ChemPhysChem* **2005**, *6*, 919.

9) C. Hellriegel, C. Seebacher, A. Zumbusch, C. Bräuchle, K. Müllen "Single Molecule Fingerprints: Spectral Dynamics of Single Terrylendiimide Molecules in PMMA at Room-Temperature" *Chem. Phys. Lett.* **2005** submitted

in preparation:

10) C. Hellriegel, Y. Rohlfing, C. Bräuchle, M. Wark "Characterization of Cy5 covalently attached to the inner surface of MCM-41 particles" - in prep

11) J.Kirtsein, B. Platschek, C. Hellriegel, C. Bräuchle, T. Bein "Diffusion of individual TDI molecules in thin SBA-15-films" - in prep.

12) C.Jung, C.Hellriegel, C.Bräuchle "Simulataneous measurement of spectral and orientational dynamics" - in prep.

Contributions to Conferences and Meetings

9.-11. März 2005 Dechema "Surfaces and Interfaces - Engineering at the Nanoscale"
invited talk: C. Hellriegel

13. Deutsche Zeolith-Tagung, 7. - 9. März 2001, Nürnberg.
New Applications: C. Hellriegel, C.F. Seebacher, F.W. Deeg, C. Bräuchle, P. Behrens, D. Wöhrle, G. Schulz-Ekloff: "Dynamics of single chromophores in porous Host/Guest Systems"

14. Deutsche Zeolith-Tagung 6.-8.März .2002, Frankfurt.
Poster: C. Hellriegel, C.F. Seebacher, C. Bräuchle "Confocal Microscopy and Single Molecule Spectroscopy to Study Mesoporous Host-Guest Materials"

15. Deutsche Zeolith-Tagung, 5. - 7. März 2003, Kaiserslautern.
presentation: C. Hellriegel, C.F. Seebacher, C. Bräuchle "Host-Guest Materials Analysed by Confocal Microscopy and Single Molecule Spectroscopy"

16. Deutsche Zeolith-Tagung, 3. - 5. März 2004 in Dresden.
presentation: J. Kirstein, C. Hellriegel, C. Bräuchle "Single Molecule Diffusion in nanostructured molecular sieves" and poster: "Host-Guest Materials Analysed by Confocal Microscopy and Single Molecule Spectroscopy"

17. Deutsche Zeolith-Tagung, 2. - 4. März 2005 in Giessen.
presentation: J. Kirstein, C. Jung, C. Hellriegel, C. Bräuchle „Translational and Rotational Diffusion of Single Fluorescent Dye Molecules in Mesoporous Host Systems“

66. DPG-Frühjahrstagung, 11.03. – 15.03.2002 in Regensburg
presentation CPP 18.1: C. Hellriegel, C. Seebacher und C. Bräuchle „Observing the Motion of Single Molecules in Nanostructured Materials“

68. DPG-Frühjahrstagung 08.03 – 12.03.2004 in Regensburg
presentation CPP 9.4: C. Hellriegel, C. Seebacher, C. Jung, C. Bräuchle „Orientation of Single Molecules in Nanostructured Molecular Sieves“

69. DPG-Frühjahrstagung 04.03 – 09.03.2005 in Berlin
presentation: DY 43.11: J. Kirstein, C. Jung, C. Hellriegel, C. Bräuchle, N. Petkov, B. Fieres, T. Bein „Diffusion of single fluorescent dyes in nanometersized channels and cage structures“

Posters: 2nd, 3rd and 4th International VW Symposium 2001-2004 (Banz, Tutzing, Banz)

7.2. Dye data / Photostability

Dye	Matrix	λ_{ex} / nm	I_{ex} / µW	$\langle n \rangle$ / 10^6
TDI	PMMA	633	34	3010
TDI	PVB	633	34	1800
CK872	PVA	568	45	8
CK872	PMMA	568	45	400
CK875	PMMA	568	45	200
CK875	PVA	568	45	10
Oxazine-1	PMMA	633	34	9
Oxazine-4	PMMA	594	34	5
Oxazine-170	PMMA	633	34	7
Oxazine-1	AFI	633	11.3	0.25
Oxazine-170	AFI	633	3.4	0.05
Oxazine-750	AFI	633	3.4	0.06
Oxazine-4	AFI	594	20	0.03
Cy-5	MCM-41	633	11.3	0.1
Cy-5	PMMA	633	34	4
Rhodamine6G	PMMA	532	20	100
TMR	PMMA	532	20	10
Coumarin153	PMMA	442	50	0.004
Perylen	PMMA	442	50	1
Tetracen	PMMA	442	50	1
PDI	PMMA	532	20	100
TMR	PMMA	532	20	10
Nile Blue	PMMA	633	34	0.1
HIDCI	PMMA	633	34	0.1

7.3. Thank you...

Prof. Dr. Christoph Bräuchle, for your excellent assistence. It was a great honour for me working in your group.

Christian Seebacher, for being an inspiration.

Johanna Kirstein and Christophe Jung, for being part of TEAM-NANO!

All co-workers, and collaborators, for example (in no particular, and probably incomplete, order): Prof. Dr. Thomas Bein and group, Dr. Ross Brown, Prof. Dr. Michel Orrit, Prof. Dr. Peter Behrens and group, Prof. Dr. Michael Wark, Prof. Dr. Klaus Müllen, Dr. Yven Rohlfing, Dr. Andreas Zumbusch, Dr. Don C. Lamb, Dr. Alper Kiraz, Prof. Dr. D. Wöhrle and Prof. Dr. Ferdi Schüth: it was exciting, stimulating and fun working with you!

The people in the Bräuchle group, (in no particular and definetly incomplete order): Moritz Ehrl, Stephan Wörmke, Barbara Müller (TEAM NANO *honoris causa*), Thomas Endress, Ralf Bausinger, Thomas Hellerer (hej, hej), Erwin Kneuper (biscuits), Fred Deeg, Robert Baumann, Ondrej Burcacki, Stefan Rigelsberger, Peter Schlüsche, Silke Steger... You know what? You're all great!

The greatest love of all, Anna, Kata and Pavlik: My feelings for you are undescribable. I wouldn't live were it not for you bunch!

Whoever I might have forgotten, please have mercy, and **do** send me a complaint!

If you are reading this line, I also thank **you** for your patience...Enjoy Frank Zappa! Good bye, and keep your eyes peeled for new fantastic publications from TEAM NANO... See you around!

7.4. Curriculum vitae

PERSONAL INFORMATION

Name:	Christian Hellriegel
Address:	Gräfelfingerstr.56, 81375 München
Date of Birth:	17.05.1974 in São Paulo, Brazil
Citizenship:	Brazilian/German

EDUCATION

1980-1988	1° Grau (1st degree) at Colégio Humboldt / São Paulo, Brazil
1989-1991	2° Grau (2nd degree) at Colégio Visconde de Porto Seguro, São Paulo, Brazil
1992-1993	Allgemeine Deutsche Hochschulreife / Colégio Visconde de Porto Seguro, São Paulo, Brazil
1994-2000	Study of Chemistry, Ludwig Maximilians Universität München
2001-present	Doctorate in the group of Prof. Dr. C. Bräuchle, Physical Chemistry, Dept. Chemie, Ludwig Maximilians Universität München